

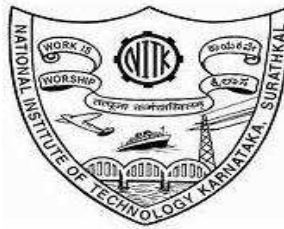
EFFECTIVE UTILIZATION OF SOLAR POWER FOR ISOLATED WATER PUMPING SYSTEM

Thesis

Submitted in partial fulfillment of the requirements for the degree of
DOCTOR OF PHILOSOPHY

by

ARJUN M



DEPARTMENT OF ELECTRICAL AND ELECTRONICS ENGINEERING,
NATIONAL INSTITUTE OF TECHNOLOGY KARNATAKA,
SURATHKAL, MANGALORE -575025

AUGUST, 2018

DECLARATION

by the Ph.D. Research Scholar

I hereby *declare* that the Research Thesis entitled Effective utilization of solar power for isolated water pumping system which is being submitted to the National Institute of Technology Karnataka, Surathkal in partial fulfillment of the requirement for the award of the Degree of Doctor of Philosophy in Electrical and Electronics Engineering is a *bonafide report of the research work carried out by me*. The material contained in this Research Thesis has not been submitted to any University or Institution for the award of any degree.

.....

Arjun M, 155016EE15F01

Department of Electrical and Electronics Engineering

Place: NITK-Surathkal

Date:

CERTIFICATE

This is to *certify* that the Research Thesis entitled Effective utilization of solar power for isolated water pumping system submitted by Arjun M (Register Number: EE15F01) as the record of the research work carried out by him, is *accepted as the Research Thesis submission* in partial fulfillment of the requirements for the award of degree of Doctor of Philosophy.

Assoc.Prof. B. Venkatesaperumal
(Research Guide)

Dr. B. Venkatesaperumal
(Chairman-DRPC, EEE dept.)

Acknowledgements

It gives me immense pleasure and great sense of satisfaction to express my heartfelt gratitude to those who made this dissertation possible.

I would like to express my sincere gratitude to Assoc Professor B Venkatesaperumal for his guidance, unending inspiration and encouragement, and for having been my Ph.D. supervisor. He and his family has been a constant source of support throughout this journey. I feel proud to have worked under his guidance.

I thank National Institute of Technology Karnataka (NITK) for giving me an opportunity for doing research and Ministry of Human Resource Department-Government of India for awarding research scholarship.

I wish to thank my research progress assessment committee (RPAC) members Dr. Y. Suresh and Dr. Arun M, for their constructive feedback and guidance. Thanks also goes to Dr. Jora M. Gonda and Dr. Vinatha U, former HODs for providing the necessary resources in the department to carry out my research. Also, I would like to thank present HOD, Dr. B Venkatesaperumal for his thought-provoking ideas and suggestions. Special thanks to Dr. A. Karthikeyan, Dr. Suresh Figarado and Dr. Krishnan, the faculties of EEE department for their valuable inputs. I also wish to thank the non teaching staff of the EEE department, specially, K.M. Naik, Arun Kumar Shetty, Basavarajaiah, Karunakar .B .S, Kasturi Rohidas and Ratnakar for providing necessary support in conducting experimentation.

Without my friends in and out of NITK Surathkal, life would have been dull. I am truly indebted to Vanjari Venkata Ramana, Roopa Viswadev, Anjan Padmasali, Dr. Ramakrishnan and Vaibhav Pai for their support, valuable inputs and constant encouragement. I wish to thank B.Tech students Subrahmanya Adiga, Anusha Adiga, Sandesh Kanchodu, Jugal

V Parmar and Alok Aryan for helping me in PCB making and necessary hardware.

I would like to express my deepest gratitude towards my parents and my sister for their love and patience which kept me going in this journey. Their faith and unconditional love towards me are the reason for whatever I have achieved in my life. Its never complete without thanking my music teacher Mrs. Pavana Balachandra Achar who has constantly supported and inspired me.

Finally, I thank God Almighty for giving me strength at all times.

Abstract

The imbalance between energy demand and the power generation has led the world to look for alternative solution called Renewable energy sources. Amongst the available energy sources, Photovoltaics (PV) has gained a lot of prominence in the present days due to its reliability and less maintenance. Therefore, the applications of PV have also become multitudinous ranging from street lights, roof top lighting till satellites. However the major drawback are its high initial costs and low energy conversion efficiency. Therefore, one of the major focus of research lie in development of efficient power electronic converters and controllers.

Due to the abundance of solar energy, and adequate requirement of water, research focus has been more on development of PV fed water pumping systems. Over the years of developments in the field of PV pump systems and power electronics technology, several topologies and control strategies have been developed. However, all these studies mentioned above assumes the PV to be receiving uniform irradiance. In an array consisting of a number of panels, it is very much sure that not all panels receive same irradiation. Often some panels are exposed to shades of buildings, clouds, etc., causing multiple peaks in the characteristics of PV array, and is termed as partial shading condition (PSC). Extracting maximum power (MPP) under such conditions becomes more challenging and complex. The non linear behavior of PV, power electronic converters and the load makes the analysis even more difficult. This study on the impact of PSC in PV systems is of high importance especially in the field of water pumping systems because PV fed water pumps are often employed in agricultural sectors where panels are exposed to soiling, shades of trees and clouds. In case of uniform shading, the MPP for varying irradiance occurs near the open circuit voltage region of the PV characteristics. In case of partial shading, the MPP occurs anywhere from short circuit current to open circuit voltage regions. The occurrence of MPP anywhere over such wide range is found to have considerable effects on water pump systems. In case of a two-stage conversion system with an intermediate DC-DC converter, the occurrence of MPP at constant current region will impose

problems such as high voltage stress on MOSFET/IGBT switches due to a higher duty cycle. It may also cause transitions from CCM (continuous conduction mode) to DCM (discontinuous conduction mode) as a result the efficiency falls drastically due to which the pump may even fail to operate though sufficient power is available at the PV terminals.

Therefore, this thesis presents the aforementioned effects of partial shading on PV fed motor pump systems. Since majority of the pump systems use induction motor, the pump system considered here for analysis is also an induction motor based. The thesis aims in studying the effects of PSC on double stage water pumping systems by developing mathematical models for PV, MPPT, DC–DC converter and induction motor system. Since the systems are non-linear, the equations governing the systems are also non-linear and implicit by nature. Therefore, advanced numerical techniques are to be employed to converge at the solution. Therefore, importance is also given to the solution techniques of the developed mathematical equations. To understand, the effect of shading on the converters stability, small signal models are also developed and several interesting observations are recorded. Finally, the effect of filters connected between the inverter and motor, to mitigate transient over voltages is studied and a cost effective solution is presented.

The entire simulation is carried out in MATLAB and verified on a laboratory setup. The results from the mathematical model and experiments are found to agree with each other. In nutshell, this thesis addresses the key points of stand alone water pumping systems and can also be used as a computer aided tool to study the PV fed pumping systems and thus helping in effective utilization of PV power.

Contents

Acknowledgement	i
Abstract	iii
List of figures	vii
List of tables	x
Nomenclature	xi
Abbreviations	xi
1 INTRODUCTION	1
1.1 Introduction	1
1.2 Photovoltaic Water Pumping Systems	2
1.3 Research Background	3
1.3.1 Literature on modeling PV and MPPT	3
1.3.2 Literature on control of motor pump systems	6
1.3.3 Literature on effects of filters on motor pump system performance	10
1.4 System Description	14
1.5 Objectives	15
1.6 Thesis organization	16
2 Modeling of PV arrays and Analytical MPPT	19
2.1 Introduction	20
2.1.1 Objectives	20
2.2 Mathematical Modeling of PV Panels	21
2.3 Proposed Analytical MPPT – I	24
2.3.1 1×2 configuration	25
2.3.2 $P \times N$ configuration	27
2.4 Results and Discussion	28
2.4.1 MPP detection for 1×2 panel configuration	28

2.5	Proposed Analytical MPPT – II	30
2.5.1	1 × 2 configuration	31
2.5.2	P × N configuration	34
2.6	Results and Discussion	36
2.7	Comparison of proposed MPPTS	40
2.7.1	Medium sized PV arrays	40
2.7.2	Larger Arrays	41
2.8	Conclusion	42
3	Modeling and Analysis of Power converter and Inverter fed Motor Pump System	45
3.1	Introduction	46
3.1.1	Objectives	46
3.2	Framework of the Objective	46
3.2.1	Effect of duty cycle on boost converter performance	49
3.2.2	Effect of C on boost converter performance	50
3.2.3	Effect of L on boost converter performance	51
3.3	Steady state Modeling of power converter and Induction motor pump	53
3.3.1	Duty cycle calculation	53
3.3.1.1	CCM	53
3.3.1.2	DCM	54
3.3.2	Induction motor and Pump	55
3.3.3	Solution of Non linear Equations	57
3.4	Dynamic modeling of Power converter and Indution Motor	58
3.4.1	Dynamic model of boost converter	58
3.4.2	Dynamic model of inverter	60
3.4.3	Dynamic model of Induction motor and pump	61
3.5	Results and Discussion	61
3.6	Conclusion	70
4	Small signal Modeling	73
4.1	Introduction	73
4.1.1	Objectives	74
4.2	Small signal model of Boost converter	74
4.2.1	CCM	76

4.2.2	DCM	77
4.2.3	Inferences	79
4.2.4	Results and discussion	80
4.3	Small signal model of Motor pump system	83
4.4	Stability of water pumping system	84
4.5	Conclusion	86
5	Effect of LC filters on water pumping systems	87
5.1	Introduction	87
5.1.1	Objectives	88
5.2	System Description	88
5.3	Selection of LC Filter Components	89
5.4	Design of Filter Inductor	90
5.4.1	Lumped Gap Inductor	90
5.4.2	Uniformly Distributed Gap Inductor	91
5.4.3	Discretly Distributed Gap Inductor	91
5.5	Results and Discussion	92
5.5.1	With lumped gap Inductor in the LC filter	93
5.5.2	With Proposed Inductor in the LC filter	95
5.6	Conclusion	100
6	CONCLUSION AND FUTURE SCOPE	101
6.1	Conclusion	101
6.2	Future scope	102
	Bibliography	107
	Publications based on the thesis	114

List of Figures

1.1	Number of peer reviewed Papers Vs Year of Publication	6
1.2	Inverter fed water pumping system with LC filter	11
1.3	Circuit diagram of a typical water pumping system	14
1.4	Control circuit for a) Boost converter b) Inverter	15
2.1	a) PV Cell Equivalent Circuit b) PV module with bypass diode . . .	21
2.2	1x2 configuration a) Schematic b) behaviour in Mode I c) Mode II . .	25
2.3	IV curves of a) individual PV panels b) combined 1x2 array	26
2.4	Experimental and simulated a) IV curves b) PV curves	29
2.5	Screenshot of MATLAB command window showing iteration details for case A	30
2.6	I-V curves under uniform shading condition indicating slopes	31
2.7	I-V curves indicating slopes when a) operating independently b) in series	32
2.8	Experimental and simulated a) IV curves b) PV curves	37
2.9	Screenshots from MATLAB command window for case B showing a) showing how inputs are fed to a generalized model b) MPP along with elapsed time c) IV and PV curves along with elapsed time	38
2.10	A 3D view showing the intersection of PV curves and, the plane con- taining MPP detected from proposed algorithm	39
2.11	Calculation of MPP for one day Irradiation data	40
2.12	Experimental Validation of simulated PV curves	40
2.13	Experimental and simulated PV curve with more number of peaks . .	42
3.1	PV curves indicating span of MPP occurrence for a) Uniform shading b) shading conditions	47
3.2	Variation of V_{dc} with duty cycle for various loads	48
3.3	Variation of efficiency of boost converter with duty cycle	49

3.4	Variation of L_{\min} with duty cycle for $P_{MPP}= 70 \text{ W}$	51
3.5	Circuit diagram of a boost converter	58
3.6	Circuit diagram of a inverter feeding motor	60
3.7	Simulated curves of PV fed induction motor water pump system showing voltage build up	62
3.8	Experimental curves of PV fed induction motor water pump system showing voltage build up	63
3.9	Simulated curves for step change in insolation and V_{dc}	64
3.10	Experimental curves for step change in insolation and V_{dc}	65
3.11	Experimental curves of PV fed induction motor water pump system showing continuously varying $V_{dc,ref}$	66
3.12	Simulated and Experimental values of MPP	67
3.13	Simulated and Experimental Duty cycle a) case one b) case two	68
3.14	Input and output power of the boost converter for $V_{dc}= 350 \text{ V}$ for case one and case two	69
3.15	Simulation and Experimental efficiency of the boost converter for $V_{dc}= 350 \text{ V}$ for case one and case two	70
3.16	Simulated and Experimental Rotor speed of Induction Motor for case one and case two	71
3.17	Experimental plots under CCM to DCM transition: a) PV panel Voltage (V_{pv}), b) PV current (I_{pv}), c) PV Power (P_{pv}), d) stator frequency (f)	71
3.18	Experimental Voltage across boost converter switch (V_{sw}) for shading patterns: a)VIII and b) IX	72
4.1	Circuit diagram of PV fed boost converter in MPPT mode feeding a load	74
4.2	Functional Block diagram of PV fed boost converter with feedback loop	75
4.3	Bode plots showing open loop stability under constant current mode in both CCM and DCM case	80
4.4	Experimental curves of PV system under constant current mode - CCM	81
4.5	Experimental curves of PV system under constant current mode - DCM	81
4.6	Simulated PV curves showing MPP value for case A and case B	82
4.7	Experimental curves of PV system under MPPT - CCM	83

4.8	Bode plots of a) DC-DC Converter b) IM pump system for various shading conditions	85
5.1	Circuit diagram of the water pumping system with LC filters	89
5.2	Cross sectional view of distributed gap inductor(not drawn to scale) .	91
5.3	Motor terminal and Inverter output voltages - without filter	93
5.4	Motor terminal,Inverter terminal voltages and stator current - with lumped gap filter	94
5.5	Temperature Profile of lumped air gap inductor	94
5.6	Thermal images of lumped air gap inductor - At the start (left image) and end(right image) of running period	95
5.7	Motor terminal, Inverter terminal voltages and stator current - with discretely distributed air gap inductor	96
5.8	Temperature Profile of discretely distributed air gap inductor	96
5.9	Thermal images of discretely distributed air gap inductor - At the start(left image) and end(right image) of running period	97
5.10	Power loss in inductors a) conventional and proposed b) percentage decrease	97
5.11	Comparison of inductor core losses	98
5.12	Copper loss in inductors a) conventional and proposed b) percentage decrease	98
5.13	Comparison of a) AC resistances b) Efficiency of the conventional and proposed inductor	99
5.14	Comparison of a) power factors b) Power available at machine terminals of the conventional and proposed inductor	100
6.1	Prototype used to validate proposed PV Panel modeling	104
6.2	Prototype of the PV fed water pumping system	105

List of Tables

2.1	PV module parameters	28
2.2	Insolation and Temperature profile for 1×2 configuration	29
2.3	Tabulation of MPP along with detection time and iterations for 1×2 configuration	30
2.4	Insolation and temperature for 1 × 2 configuration	36
2.5	Tabulation of MPP along with detection time and iterations for 1×2 configuration	37
2.6	Tabulation of MPP calculated from method I and II	41
2.7	Tabulation of MPP calculated from method I and II for larger arrays	41
3.1	IM pump parameters	47
3.2	Insolation profile for the panels considered for simulation. Temperature (T)=35° C for all cases	48
5.1	Comparison table	92

Nomenclature

AC	Alternating current
CCM	continuous conduction mode
CCVSI	Current controlled voltage source inverter
CF	Crest factor of the filter inductor
CRGO	Cold rolled grain oriented steel
DC	Direct current
DCM	discontinuous conduction mode
ESR	Effective series resistance
FEA	Finite element analysis
FLS	Fuzzy logic systems
IM	Induction machine
LHP	Left half plane
MLPT	Minimum loss point tracking
MPP	Maximum power point
MPPT	Maximum power point technique
PSC	partial shading condition
PID	Proportional integral and differentiator
PV	Photovoltaics
QDG	Quasi distributed air gap
RHP	Right half plane
SVM	Space vector modulation
UDG	Uniformly distributed air gap
$\cos(\phi)$	Power factor of the induction motor
ω_r	Rotor speed of the induction motor in rad/s
ω_s	Stator speed of the induction motor in rad/s
τ_u	Reflection co-efficient of the load
ψ_{dr}	Rotor direct axis flux of induction motor
ψ_{ds}	Stator direct axis flux of induction motor
ψ_{qr}	Rotor quadrature axis flux of induction motor
ψ_{qs}	Stator quadrature axis flux of induction motor
A	Curve fitting factor.
A_c	Core area the filter inductor

A_w	Window area of the filter inductor
A_p	Area product of the filter inductor
B_{sat}	Flux density saturation
C	DC link capacitance (output capacitance of boost converter)
C_f	Filter capacitance
C_{in}	input capacitance
C_{sw}	Charging capacitance of diode and switch
D	Duty cycle
f	stator frequency of the induction motor
f_{rated}	Rated frequency of the motor
f_s	switching frequency of the boost converter
I_{cell}	PV cell current
$I_{c_{in}}$	Current through input capacitor of the boost converter
I_d	Current through bypass diode
i_{dr}	Rotor direct axis current of induction motor
i_{ds}	Stator direct axis current of induction motor
I_{inv}	DC side inverter current
I_L	Average current of the boost converter inductor
I_m	Induction motor stator current
I_p	PV current of the p^{th} parallel path
$I_{o,pd}$	saturation current of the parallel diode
I_{ph}	photo current
I_{pd}	current through the parallel diode
I_{pv}	PV output current
i_{qr}	Rotor quadrature axis current of induction motor
i_{qs}	Stator quadrature axis current of induction motor
I_{SC}	Short circuit current of the panel
J	Moment of inertia of induction motor
k	Boltzaman constant
K	Pump constant
L	Boost converter inductance
l_c	Lenght of cable in feet
L_f	Filter inductance
l_g	air gap length of filter inductor

L_r	Rotor inductance of induction motor
L_s	Stator inductance of induction motor
L_{\min}	Minimum inductance of the boost converter to operate in CCM
L_{lr}	Rotor leakage inductance of induction motor
L_{ls}	Stator leakage inductance of induction motor
L_m	Magnetising inductance of induction motor
m_a	modulation index
N_r	Rated motor speed
P	Poles of induction machine
P_{loss}	Losses in the boost converter
P_{MPP}	Power at MPP
P_{sh}	Power available at the induction motor shaft
q	Charge of the electron
R	Equivalent load as seen by the output of boost converter
ref	Reference
r_c	Effective series resistance of boost converter output capacitor
$r_{c_{\text{in}}}$	Effective series resistance of boost converter input capacitor
r_l	Effective series resistance of boost converter inductor
r_{sw}	Effective series resistance of boost converter IGBT switch
R_r	Rotor resistance of induction motor
R_s	Series resistance of the PV panel
R_{st}	Stator resistance of induction motor
R_{sh}	Shunt resistance of the PV panel
t_e	Electromagnetic torque of the induction motor
t_l	Load torque of the induction motor
t_r	Rise time of the induction motor terminal voltage
V_{cell}	PV cell voltage
v_d	Voltage drop across the boost converter diode
V_{dc}	DC link voltage
v_{dr}	Rotor direct axis voltage of induction motor
v_{ds}	Stator direct axis voltage of induction motor
$V_{\text{m}_{\text{rms}}}$	Rated Motor voltage (line to line)
V_{OC}	Open circuit voltage of the panel
V_{pv}	PV output voltage

V_{pn}	PV Voltage of n^{th} panel in p^{th} parallel path
v_{qr}	Rotor quadrature axis voltage of induction motor
v_{qs}	Stator quadrature axis voltage of induction motor
V_T	Thermal voltage of the diode

Chapter 1

INTRODUCTION

Contents

1.1	Introduction	1
1.2	Photovoltaic Water Pumping Systems	2
1.3	Research Background	3
1.3.1	Literature on modeling PV and MPPT	3
1.3.2	Literature on control of motor pump systems	6
1.3.3	Literature on effects of filters on motor pump system performance	10
1.4	System Description	14
1.5	Objectives	15
1.6	Thesis organization	16

1.1 Introduction

This chapter presents an introduction to one of the potential applications of photovoltaics (PV) called, the PV water pumping systems. It discusses one of, the certain problems of PV, known as partial shading conditions (PSC). Furthermore, a detailed study of the available literature covering various aspects of PV fed water pumping systems is presented. The last section of the chapter covers the objectives and the chapter wise organization of the thesis.

1.2 Photovoltaic Water Pumping Systems

The shortage of natural resources like coal, diesel along with the increasing demand for electricity generation has led the world to gain interest in promising energy sources like solar (PV) and wind. Photovoltaic systems have gained the confidence of many developing countries due to its reliability and lesser maintenance. Govt. of India, in its Jawaharlal Nehru Solar Mission has planned to setup and expand PV applications up to 2000MW by the year 2022 (MNRE, 2012) and the world installed capacity is forecasted to be upto 500GW by the year 2020. The major drawbacks of the PV is its high initial costs and low efficiency. Therefore, the focus of research lie in effective utilization of PV output power (Periasamy et al., 2014).

According to the reports from World Bank, 60% of the land in India is agricultural. About $2/3^{rd}$ of it is non irrigated and hence largely depends on seasonal monsoon. Also, the agriculture is adversely affected in summer due to lack of rain. Therefore, the only means of providing year around water for cultivation is ground water. This is also the largest means of water source(Siebert et al., 2010). The power requirement for the water pumping system is met either from a grid or from standalone power generating units like diesel engine, wind or PV. The shortage of electricity, voltage fluctuations and distribution losses in case of grid fed pumps have made the stand alone pumping applications a better solution(Periasamy et al., 2014). Due to the abundance of solar energy, and huge requirement of water, water pumping becomes one of the important applications of PV.

These PV arrays have a characteristic that it exhibits a non-linear relationship between its voltage and current, and there exists only one operating point at which maximum power can be extracted from the PV array. This operating point is called maximum power point (MPP) and operating the PV at this MPP is one of the most sought-after research topics in PV systems. In an array consisting of a number of panels, it is very much sure that not all panels receive same irradiation. Often some panels are exposed to shades of buildings, clouds, etc., causing multiple peaks in the characteristics of PV array, and is termed as partial shading condition (PSC). Extracting MPP under such conditions becomes more challenging and complex. This study on the impact of PSC in PV systems is of high importance especially in the field of water pumping systems. PV fed water pumps are often employed in agricultural sectors where panels are exposed to soiling, shades of trees and clouds (with slow-

moving clouds the conditions worsen even more). Therefore, the focus of research lie in investigation of effective utilization of PV output power.

1.3 Research Background

The literature on the PV water pumping systems can be broadly described into following categories

1. Literature on modeling PV and maximum power point techniques (MPPT)
2. Literature on control of motor pump systems
3. Literature on effect of filters on the motor pump system performance.

1.3.1 Literature on modeling PV and MPPT

One of the factors affecting the performance of PV systems is partial shading. Often the panels get partially shaded due to soiling and clouds. The effect of shading can be seen from small PV plants till larger distributed power generation units(Patel and Agarwal, 2008). Thus, it becomes a matter of interest in recent studies. The multiple peaks in PV characteristics due to these partially shaded panels make MPP detection even more challenging. In view of the importance of peak detection, various methods that can track MPP are proposed in the literature. According to (Farivar et al., 2013), these methods are categorized as a) direct methods b) artificial intelligent methods and c) Indirect methods. The first two methods have however played a significant part in detecting global maxima (MPP). The subject of this thesis falls into the third category i.e., indirect methods, which involves the solution of a set of mathematical equations to calculate MPP. These methods involve calculating MPP analytically. Analytical methods use mathematical functions to solve the given problem and therefore are one of the dominant strategies. A very handful of research work based on analytical methods such as detecting MPP based on use of constant fraction of open circuit voltage and short circuit current(Masoum et al., 2002)(Tafticht et al., 2008), mean value theorem(Rodriguez and Amaratunga, 2007), fourth-degree polynomial curve fitting(Xiao et al., 2006) and lambert equations(Farivar et al., 2013) can be seen in literature. All these methods involve the solution of non-linear equations using non-iterative techniques. With the view of simplifying the equations and solve

them through non-iterative techniques, often several assumptions are made, which may lead to compromise on the accuracy of results. However, with recent advances in technology, with the availability of fast processing computers and better non-linear solving techniques like trust region based algorithms, iterative techniques could be employed to yield better results. A few hybrid iterative methods involving MPP locus accelerated method and incremental conductance method (Hartmann et al., 2013) and online parameter estimation methods(Garrigós et al., 2007)(Toledo et al., 2012)(Blanes et al., 2013) are reported in the literature.

Based on the available literature, following are some points of observation: In all the studies mentioned above, analytical methods have only been used to calculate MPP under uniform shading conditions involving just single peak. In most practical cases, not all panels in a PV string receive uniform irradiation(Patel and Agarwal, 2008). Due to this non-uniform irradiance reception, the PV characteristics exhibit multiple peaks and thus extracting MPP is more challenging. Since analytical methods are potent tools, extracting global peak in case of more challenging partial shading conditions are worth investigating. The mathematical equations derived for uniform shading conditions are often approximated with assumptions to avoid iterative techniques which would compromise on the accuracy of the results. With advancements in the field of optimization techniques and availability of high processing computers, iterative methods are handier than before, and one need not worry about computation complexities and therefore achieve more accurate results. With the points mentioned above in view, this thesis proposes two analytical solutions that can theoretically compute MPP involving N peaks.

- It provides several illustrations of detecting global peak from a smaller array till a more massive arrays (In general, array sizes of order $P \times N$). It also verifies that the predicted peak is in total agreement with experimental results.
- It also provides the necessary convergence details to ensure that the solution lies in the close vicinity of solution point.

These maximum power point tracking (MPPT) techniques invariably involve controlling the panel voltage and current using a power electronic converter based on the insolation levels and temperature. Any system which is being aimed to be controlled requires feedback. The feedback system should meet specific requirements such as stability, and properties such as settling time, overshoots, steady-state regulation

(Erickson and Maksimovic, 2007). To design a stable feedback system, we need its dynamic model. These dynamics introduced by inductors and capacitors are studied with the help of small signal models.

Stability models for power electronic converters in output voltage and input current control modes can be extensively seen in literature. However, the stability models for PV driven systems with additional input capacitor are seldom covered. The feedback controller design issues for MPPT with a buck(Solodovnik et al., 2004)(Espinoza-Trejo et al., 2015) and boost(Cai et al., 2016) converters can be seen in recent studies. The analysis considers the input capacitor into modeling. However, the effect of input capacitor on the stability is not explicitly studied. It is also unclear if the input capacitor has the same effect on stability for all the power electronic converters or rather it is converter specific. AC small signal modeling for a distributed MPPT with a boost converter as an example is derived in (Femia et al., 2008). It is observed that the dynamic interaction amongst each of the self-controlled PV modules is not responsible for any instability problem. Small signal models for double current mode controllers (Zhang and Kimball, 2018) and output voltage regulation modes(Villalva et al., 2010)(Qin et al., 2015) are also presented in the recent literature. With the aforementioned discussions, here are some points to be pondered. Stability models, especially for PV fed systems, are seldom covered. The effect of input capacitance (capacitor connected between the PV and the power electronic converter) on the system stability has not been discussed exclusively. It is observed that most of the models assume that the converter operates in CCM. However, PV systems are sometimes found to enter into DCM(Bharadwaj and John, 2014). Therefore, stability models for DCM need to be investigated.

Given the discussed subject, the contributions of this thesis are

- It provides stability models for a non-ideal boost converter in both CCM and DCM modes through detailed derivations.
- It also shows exciting results like pole-zero cancellations in both the modes leading to a significant conclusion. It also provides the experimental proof to validate the presented concept.

1.3.2 Literature on control of motor pump systems

Fig. 1.1 is the graphical representation of the number of papers published in the area of water pumping system with respect to the year of publication. It is important to note that over the span of 37 years (from 1979 - 2016), roughly 43 potential papers have been published in peer reviewed Journals (IEEE, Elsevier, Science Direct and Wiley). It also indicates the scope that lie in this field to carry out further research. The concept of the solar water pumping system(as per the available literature) was coined at Lincoln Laboratory, Lexington, Massachusetts (Matlin, 1979). The system was setup and tested at Cairo, Egypt and Orissa, India based on the geographical study carried out. The report lays guidelines for selection of pumps and motors based on the geographical conditions. The report though forms the baseline literature for water pumping system. It does not contain any information from the electrical point of view.

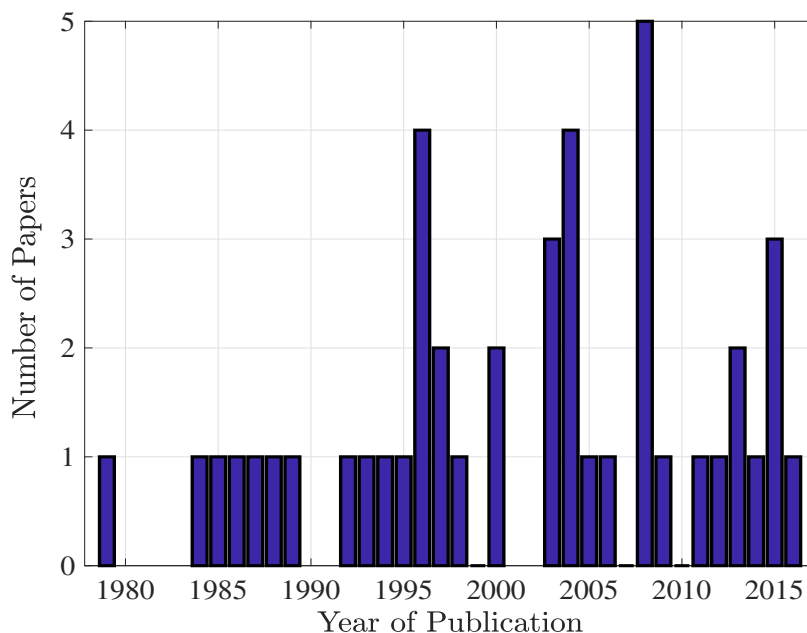


Figure 1.1: Number of peer reviewed Papers Vs Year of Publication

Selection of the type of pump is very important in design and development of the water pumping system. The drive selection depends on the pump being used.

Centrifugal pumps are the mostly used pumps for the water pumping applications. Joseph R. Pottebaum (Pottebaum, 1984) has derived various pump characteristics that assist the designer to judge the suitability of a given motor drive algorithm for his pumping application.

The earliest topology on water pumping systems focussed more on matching the load characteristics with source without using more of power electronic converters. Water pumping systems uses either DC or AC machines. The shaft of the machine is coupled to a pump. Based on the type of machine used, it is classified as DC or AC water pumping system. The transient and steady state performance of DC motors (series, shunt and separately excited motors) directly coupled to the PV source were studied through simulations package called SUPER SCEPTRE. The separately - excited (or permanent magnet) motor with a ventilator load was found to be the most suitable for the solar cell generator. The series motor is quite acceptable, but the shunt motor gives poor performance (Appelbaum, 1986).

Induction motor (IM) based PV water pumping system was proposed due to its ruggedness, small size, feasibility for more control strategies and low maintenance. The complete pumping system was implemented using a dc-dc converter, a three-phase inverter, and an induction motor-pump set. An optimized relationship between stator voltage and frequency was developed to control the speed of the motor (Bhat et al., 1987). This system which involves dc-dc converter and an inverter is called as double stage water pumping system.

DC shunt motors based water pumping system was studied through computer simulations. Transient analysis and steady state characteristics were evaluated. The emphasis was lead to steady the starting characteristics of the motor (Fam and Balachander, 1988). The performance of the PMDC based water pumping system with and without DC-DC converter for multiple pumps loads was analyzed and several conclusions were drawn. The over all research highlighted the importance of maximum power point tracking (MPPT) scheme (Appelbaum and Sarma, 1989). The literature study thereafter concentrated on converter topologies of DC-DC Converters for DC water pumping systems.

The performance of IM based water pumping system for varying insolation and temperature was carried out. The system efficiency became a major concern when the input power was variable. The frequency of the IM stator was adjusted in accordance with the varying insolation and temperature. The system was simulated for various

insolation and temperature levels using the Electromagnetic Transients Program. It was shown that the system's overall efficiency can be considerably enhanced and the operation of the motor, including transient responses such as starting is improved(Yao et al., 1994).

The optimum efficiency of the IM water pumping system was achieved by maintaining a proper balance between the flux (i_{ds}) and torque components (i_{qs}) of the motor current, which in turn equalizes the fixed and the variable losses of the cage motor. The reference currents generated and actual currents are fed to current controlled voltage source inverter (CCVSI). A high frequency chopper served as the interface between the PV source and CCVSI(Singh et al., 1996).

A comparison analysis of operating the PV array on the maximum power line and operating at maximum efficiency of the induction motor was carried out. It was observed that, in the first case, the system can be controlled to operate from an insolation level much lower than the second system. The quantity of water pumped was much larger for first case(Eskander and Zaki, 1997).

A single inverter which acts as both a variable frequency source and a peak-power tracker of the system was studied. This configuration avoids the use of a dc-dc converter which was specifically meant to track maximum power from the PV source. The direct interface of the inverter with the PV therefore reduces the number of power electronic switches. The inverter maintains the power balance between the source and load so as to avoid DC link voltage collapse(Muljadi, 1997a). Such scheme is termed as single stage water pumping system.

A mechanical power point tracker was employed in a water pumping system driven by a PMDC motor. It was observed that the through manual tracking (i.e., changing the orientation of PV array, three times a day to face the sun) the output obtained is 20% more compared to the fixed tilted PV array. The simulation and experiments were studied for different insulations and temperatures(Kolhe et al., 2004).

A study on tuning PID (Proportional, Integral and Derivative) controller for water pumping applications was carried out. Three tuning methods viz., Ziegler Nichol's based on reaction curve, Ziegler Nichol's based on critical gain and Cohen-coon parameters were analyzed. The results indicate that the methods based on the systems response in open-loop are the most suitable for such applications(Brito and Zilles, 2006). The complexities in tuning a PI controller was overcome by developing a Fuzzy logic based MPP system. The system was tested for varying solar insolation,

temperature and electric load variations(Altas and Sharaf, 2008).

An Induction motor based water pumping system with a push-pull converter and an inverter was studied through simulations and experimentations. By using a push-pull converter, it is convenient to select the transformer turns ratio “N” such that duty cycle (D) does not vary in a wide range. The research evaluated several control strategies and optimization procedures for induction motor control that can be used for implementing an effective photovoltaic pumping system(Vitorino et al., 2011).

A minimum losses point tracking (MLPT) approach, for the induction motor was applied to a stand-alone photovoltaic pumping system. The proposed approach is based on the basic principle of operating the motor with reduced flux at reduced load torque, so that its efficiency is always maximum. Power savings up to 8% of power input were obtained in the experimental tests(Corrêa et al., 2012).

Another comparative study between a double stage and single stage photovoltaic water pumping system was carried out. The systems were tested for different heads and the conclusions were drawn on the basis of quality of output power and quantity of the total water delivered. The overall system efficiency of Sine-wave Pump Controller with MPPT (SPCM)/double stage water pumping system was found to be 18% higher than VFD/single stage water pumping system for the same head level. The output power quality of SPCM was considerably higher to its counterpart, the THD was lower and it also pumped 30%-70% more water than VFD(Yadav et al., 2015).

The small signal model for a two stage water pumping system was developed and the Proportional and Integral values of the controllers were calculated. The research laid emphasis on regulating the DC link voltage. The aim of using dc-link voltage controller is to set the reference speed of the induction motor so that dc-link voltage tracks the voltage output of the MPPT(Periasamy et al., 2015).Considering the difficulty in tuning the PID controller, as well as providing the use of VFDs that do not have the PID embedded, an external control system, based on Fuzzy Logic Systems (FLS), was developed which is able to maintain a stable DC excitation voltage level of the VFD. It was observed that the controller is able to maintain the voltage level of the dc bus of the VFD constant and close to the set-point value, even with the occurrence of weather variations.(Maranho et al., 2016).

However, all these studies mentioned above assumes the PV to be receiving uniform irradiance. In case of uniform shading, the maximum power condition for varying irradiance occurs near the open circuit voltage region of the PV characteristics. In

case of partial shading, the MPP occurs anywhere on the curve (Patel and Agarwal, 2008). The occurrence of MPP anywhere over such wide range is found to have considerable effects on both single stage and double stage pump systems. In single stage pumps, if the peak power lies at the short circuit current region, the available panel voltage may not be sufficient to run the IM pump system, and the pump fails to operate, though adequate power is available at the PV terminals. In case of a two-stage conversion system with an intermediate DC-DC converter, the occurrence of MPP at short circuit current region will impose problems such as high voltage stress on MOSFET/IGBT switches due to a higher duty cycle. It may also cause transitions from CCM (continuous conduction mode) to DCM (discontinuous conduction mode) as a result the efficiency falls drastically due to which the pump may even fail to operate though sufficient power is available at the PV terminals.

Given the above discussions, the contributions of this thesis are

- It showcases the effects of partial shading on two-stage water pumping systems (system with a boost converter, inverter and induction motor pump) with several shading illustrations.
- It experimentally verifies that the converter may have to operate at higher duty cycles to meet the DC bus requirement. To avoid the high duty cycles, the converter may also operate at discontinuous modes which reduce the efficiency of operation to such a lower extent that the pump may even fail to operate though sufficient power is available at the PV terminals.

This research work thus helps in understanding the detrimental effects these partial shading might cause on the entire water pumping systems if the conditions are overlooked and thus serves as a reference tool for practitioners who wish to study PV fed pumps. Therefore, this study forms a complete framework for technical aspects of IM based water pumping systems and stand unique in terms of its technical contribution to the field of water pumping systems.

1.3.3 Literature on effects of filters on motor pump system performance

Till date, the prime focus in the literature has been on the development of MPPT strategies for extracting maximum power from the PV panels, designing different

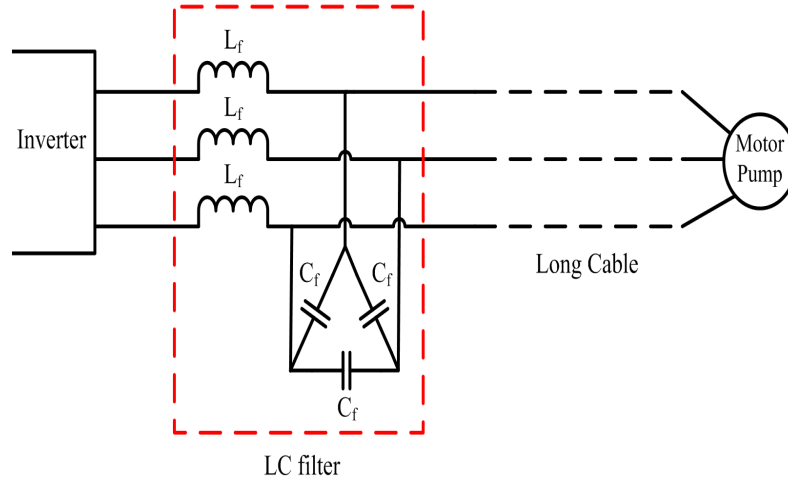


Figure 1.2: Inverter fed water pumping system with LC filter

topologies of power electronic converters, and development of new control strategies for inverters. Though all these proposed methods help in better utilization of PV power, the study of effect of LC filter is not considered in the literature. LC filter is connected across the inverter terminals to mitigate the over voltage across the machine terminals, which would otherwise cause motor insulation failure. The schematic of the Inverter fed water pumping system with LC filter is shown in Fig. 1.2. The study of LC filter and their failure in pumping systems is important because:

- PV water pumping systems have fairly high initial investments. Frequent non working conditions increase the maintenance costs which are not desirable.
- Agriculture applications demand at least a working time of 6-8hrs per day, of which 2hrs is peak demand conditions. Therefore, over heating or system damage due to long running are to be strictly avoided.

Therefore in this thesis, the effect of LC filter design for a PV fed induction motor water pumping system is discussed owing to its need and importance. It is to be noted that, the water pumping systems are mainly employed in agricultural sectors, where cost is of prime importance. Hence, the solution proposed should be cost effective. This forms the key aspect of this research work.

In case of submersible pumps, the distance between the machine and the inverter is over the order of 100s of meters. Long cables run between the terminals of the motor and the inverter. These cables cause transient over voltages across the machine

terminals. These over voltages are due to the reflections caused by the cable inductor and capacitor(Persson, 1992). The induction motor reliability greatly depends on the maximum over voltage value, rate of rise and switching frequency(Bonnett, 1996). In some cases, overvoltages which are greater than 2pu are also observed(Kerkman et al., 1997).

To mitigate the effects of overvoltages, connecting LC filters at the motor or at inverter terminal is the most feasible and cost effective solution. The additional advantage of using an LC filter is that, it helps in compensating for reactive power and helps in longevity(Steinke, 1999). In (von Jouanne and Enjeti, 1996), design issues are discussed in detail. Equations for critical rise time below which overvoltages occurs have also been derived. In (von Jouanne et al., 1995), filters are placed at the machine terminals and that effects are presented. However, this is not feasible in case of submersible pumps where motor terminals are not accessible.

Different topologies of LC filters are presented in the literature. A conventional LC filter topology with the delta connected capacitors addresses only the differential mode voltage problems. To mitigate the common mode problems, several other topologies are designed and presented. These topologies mostly involve access to the inverter neutral or inverter pole(Steinke, 1999), (Chen et al., 2007)-(Habetler et al., 2002). In induction motor fed pumps, since the load is mostly balanced, a simple LC filter which addresses only the differential mode is sufficient.

It is therefore clear that a simple traditional LC filter connected at inverter terminals is found to be successful solution to mitigate the overvoltage problems. However, the study on the life of LC filters in water pumping applications are not addressed in the literature so far. This study is very important especially in PV fed pumps where efficiency and longer life span is of prime concern owing to its high initial investment and longer working conditions.

It is noticed that, when a lumped gap inductor(conventional) is used in LC filter, the system fails when subjected to long running conditions. Through experiments, its observed that the failure is due to excess heating of the inductor within a short time span. This inturn affects the reliable operation of the system.

Lumped inductors with air gap are the conventional inductors widely used as filters. These have the advantage that fabrication and packaging are relatively simpler and they are made up of high permeability material(Hu and Sullivan, 2001). However, they are associated with high losses and hence results in over heating of the inductor.

These high losses are due to fringing fields. In systems, which are often subjected to prolonged runs, reliability is a major concern. Therefore, employing such inductors would prove to be fatal. The problem of high losses in the inductor can be overcome by controlling the field distribution, in other words by distributing the airgaps uniformly(Ngo and Kuo, 1988).

Uniformly Distributed air gaps in a high permeability core are one such choice over inductors with a single air gap. In powdered core inductors, the core does not saturate at lower flux levels due to a number of tiny air-gaps present throughout the magnetic path. Therefore, the current density is approximately linear avoiding the fringe field. The performance of these powdered cores are enhanced to a greater extent by using multi permeable cores i.e., combined core of high and low permeability. By using multi permeable core, the current density is made more uniform and therefore results in lower losses and better saturation characteristics(with respect to ferrite cores)(Kirchenberger et al., 1992)-(Kutkut and Divan, 1998a).

However, low permeability of the material, increased core losses, poor inductance regulation at lower loads, large effective series resistance (ESR) at higher operating frequencies, lower B_{sat} (flux density saturation) value compared to CRGO(cold rolled grain oriented steel) are some of the drawbacks of the powdered core inductors. For given values of inductance and energy storage, the volume/area product and the number of turns requirement for amorphous core is higher compared to ferrite or CRGO cores. In addition to these drawbacks, powdered cores do not form cost effective solutions which is the prime concern. Hence, the need is to use an inductor which has lower losses, higher permeability, occupies lesser volume and requires minimum number of turns. The core used in the inductor should also be available at a fairly affordable price.

Quasi distributed gap inductors(discretely distributed gap inductors) are found to be excellent solutions for the aforementioned problem. Quasi distributed gap inductors divide the single large air gap into several small discrete air gaps. The literature so far has focussed on modeling of quasi distributed gap inductors using FEA(finite element analysis), 1-D and 2-D methods and how best these inductors can be approximated to a uniformly distributed gap inductors(Hu and Sullivan, 2001)(Hu and Sullivan, 1997)(Nomura et al., 2013). But the literature lacks in following aspects:

- The real time applications of quasi distributed inductors as a cost effective solution.

- The reduction in size of the inductors when a more permeable material like iron or CRGO is used (this comparison is with respect to the powdered cores).

In this thesis, the water pumping system employing lumped air gap inductors is first studied through experiments. It is seen that the inductor heats up exponentially to a high temperature, within a short time span. The winding losses are studied at different operating frequencies. To reduce the losses (and to improve reliability), the inductor is redesigned with a suitable multi gap (discretely distributed and uniformly distributed gap) inductor. Through mathematical calculations it is shown that discretely distributed gap inductors are a better choice over powdered core inductors. Experimental results and thermal profile of the lumped air gap and the discretely distributed gap inductor are presented to validate the predictions done by calculations.

1.4 System Description

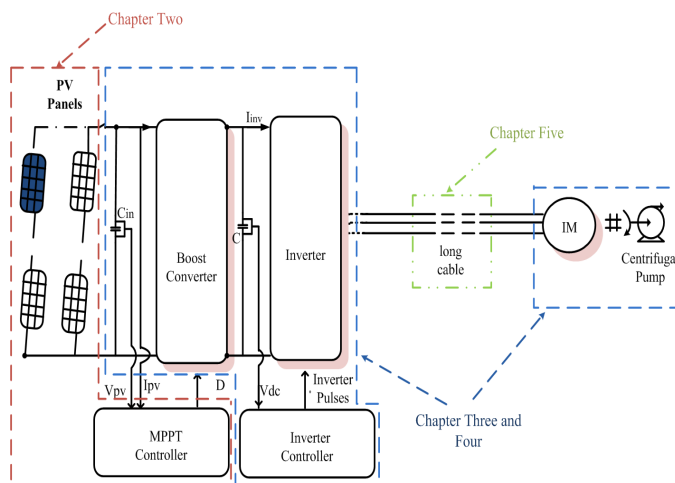


Figure 1.3: Circuit diagram of a typical water pumping system

Fig. 1.3 shows the circuit diagram of a typical water pumping system which will be used for analysis in this thesis along with the chapter wise analysis. Here, C_{in} is the input capacitor, C is the output capacitor, I_{inv} is the input current of the inverter and V_{dc} is the DC link voltage. The system consists of PV panels feeding a boost converter. The boost converter tracks the maximum power from the PV terminals by setting appropriate duty ratio (D). The boost converter output terminal is called as DC bus which further feeds a two-level, three-phase voltage source inverter. The AC terminals of the inverter are supplied to IM pump system through a long cable.

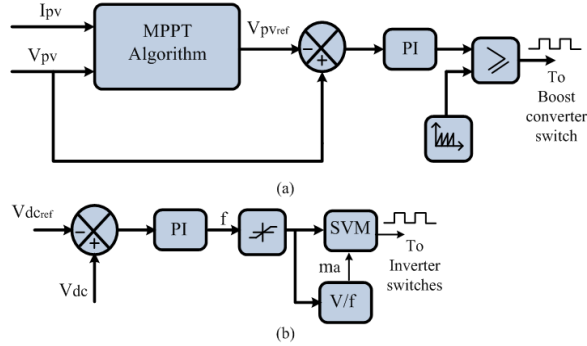


Figure 1.4: Control circuit for a) Boost converter b) Inverter

It is a well known fact that, for a given insolation and temperature, there exists an operating point that extracts maximum power from PV panels. A boost converter acts an interface between the PV panels and the load to operate the panel at MPP. The control scheme for boost converter to operate at MPP is given by Fig. 1.4a. The control involves sensing panel voltage (V_{pv}) and panel current (I_{pv}) which forms as input to the MPPT algorithm. The algorithm generates a reference PV voltage called V_{pv_ref} that should be maintained across PV terminals for succesful MPP operation. In order to accomplish this, the generated V_{pv_ref} is compared with actual (V_{pv}) and the error is fed to a PI controller to generate duty cycle to control the boost converter switch.

The MPP extracted from PV is transfered via boost converter to the DC bus. The principle here is to transfer the entire power from DC bus to the IM pump system. Any mismatch in power levels will either lead to swell or sag in the DC bus voltage. Therefore, the control is here to maintain the DC bus voltage at a set point level called V_{dc_ref} . The control strategy is shown in Fig. 1.4b. The value of actual V_{dc} is compared with the V_{dc_ref} and the error is fed to another PI controller. The controller outputs the stator frequency at which the IM pump system should be operated so acheive power balance at DC bus. The stator frequency command from the PI controller is fed to v/f and space vector modulation schemes to generate pulses to the inverter.

1.5 Objectives

Based on the review of the literatures related to Photovoltaic based water pumping system, following have been identified as the main objectives of the research work

1. To develop a mathematical model that can also serve as a computer aided

design tool for users to understand the effects of partial shading conditions on the operating conditions and efficiency of power converters and water pumps. The mathematical model takes into account the non idealities of the practical system to yield results that are more practical.

2. To study the effects of partial shading conditions on the stability of the converters and pump system by developing small signal models. To exclusively give emphasis on the understanding the effect of input capacitance on the DC–DC converter stability
3. To investigate the failure of LC filters connected between the inverter and the motor pump and thereby providing a cost effective solution to aid uninterrupted and prolonged running conditions

Therefore, this study forms a complete framework on technical aspects of IM based water pumping systems and stand unique interms of its technical contribution to the field of water pumping systems.

1.6 Thesis organization

There are six chapters and two appendices in this thesis document.

Chapter 1: Presents a brief introduction to the state-of-the-art PV water pumping systems through a detailed literature survey. Based on the review of the work carried out, the objectives of the thesis are presented. This chapter also presents the system description of the water pump which will be universally used in the thesis.

Chapter 2: Proposes the model of a PV panel which can further be used to model arrays of any size. The proposed model will further be used to present proposed analytical MPPT techniques. The proposed methods are tested for smaller arrays, more massive arrays and one day irradiation data. Finally a comparative study of both the proposed techniques are presented.

Chapter 3: Discusses the effect of partial shading on the PV pumps through detailed steady state and dynamic models. Extensive simulation and experimental results are presented to provide sufficient proof to the studied theory.

Chapter 4: In this chapter, small signal models for boost converter is presented for both CCM and DCM and interesting inferences are drawn. In the later section of the chapter, small signal model for IM pump system is also presented. Thus, providing stability model for over all water pumping systems.

Chapter 5 : An investigation on the effect of LC filter on water pumping system is presented through experimental investigations. The losses in the conventional inductor is studied and a cost effective solution is presented.

Chapter 6: Summarizes the thesis major contributions and includes some discussions on possible future research.

Chapter 2

Modeling of PV arrays and Analytical MPPT

Contents

2.1	Introduction	20
2.1.1	Objectives	20
2.2	Mathematical Modeling of PV Panels	21
2.3	Proposed Analytical MPPT – I	24
2.3.1	1×2 configuration	25
2.3.2	P×N configuration	27
2.4	Results and Discussion	28
2.4.1	MPP detection for 1 × 2 panel configuration	28
2.5	Proposed Analytical MPPT – II	30
2.5.1	1 × 2 configuration	31
2.5.2	P × N configuration	34
2.6	Results and Discussion	36
2.7	Comparison of proposed MPPTS	40
2.7.1	Medium sized PV arrays	40
2.7.2	Larger Arrays	41
2.8	Conclusion	42

2.1 Introduction

Partial shading is one of the most inevitable conditions in any PV installations. The PV characteristics of such partially shaded PV systems exhibit multiple peaks, thereby making it more complex to understand and extract maximum power. Therefore, it becomes necessary to understand this complex behavior of PV to predict this maximum power point (MPP). Analytical methods are known to be powerful tools that establish relationships between variables in complex systems using mathematical functions. Once the relationship between the variables are expressed mathematically, it becomes easier to study any complex systems. With fast processing computers and computational softwares available in present days, solution of non linear equations is not a concern. This thesis presents two analytical approaches to solve maximum power point problem under partial shading conditions. The proposed method is generic and can be applied to configurations of any size. Equations describing PV panels and MPP conditions are derived by applying fundamental circuit laws and the proposed MPPT techniques can theoretically detect the MPP amongst 'N' peaks. The MPP models presented can be used as a easy to use computer aided tool to study PV systems under partial shading conditions. The results from the proposed models are validated through experimentations and its functionality has been shown through several illustrations. The simulations are performed using MATLAB, however the model can be simulated on any such computational tools.

2.1.1 Objectives

The objectives of this chapter are

- It provides several illustrations of detecting global peak from a smaller 1x2 array till a more massive arrays (In general, array sizes of order $P \times N$). It also verifies that the predicted peak is in total agreement with experimental results.
- It also provides the necessary convergence details to ensure that the solution lies in the close vicinity of solution point.

2.2 Mathematical Modeling of PV Panels

This section contains modeling of PV system which will further be used to model the proposed MPP technique.

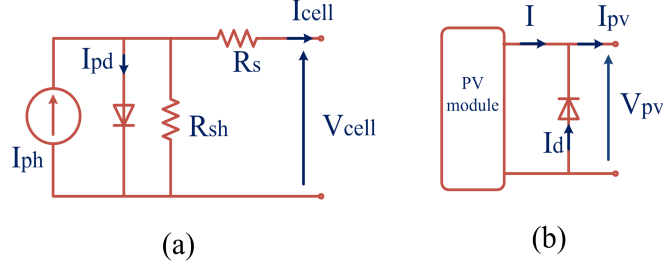


Figure 2.1: a) PV Cell Equivalent Circuit b) PV module with bypass diode

The electrical equivalent of a PV cell with single diode is given in Fig. 2.1a. I_{ph} is the photo current, I_{pd} is the current through the parallel diode, R_{sh} and R_s are the shunt and series resistances, I_{cell} is the PV cell current and V_{cell} is the PV cell voltage.

Referring to Fig 2.1, the equation for I_{cell} can be written as

$$I_{cell} = I_{ph} - I_{o,pd} \left(e^{\frac{q(V_{cell} + I_{cell}R_s)}{AKT}} - 1 \right) - \frac{V_{cell} + I_{cell}R_s}{R_{sh}} \quad (2.1)$$

where $I_{o,pd}$ is the saturation current of the parallel diode, q is the charge of the electron and K is the Boltzaman constant and A is the curve fitting factor.

Since the slope of the IV curve at short circuit current is parallel to voltage axis, it implies $R_{sh} \approx \infty$. However (2.1) is valid for a PV cell. Since a PV panel is a made of a PV cells in series, a term N_s (number of series connected cells) is appended to the PV cell equation. Therefore, (2.1) becomes,

$$I = I_{ph} - I_{o,pd} \left(e^{\frac{q(V + IR_s)}{N_s AkT}} - 1 \right) \quad (2.2)$$

where, I and V are the PV panel current and voltage. It is very well derived in (Ding et al., 2012), that (2.2) can be simplified as,

$$I = I_{sc} \left(1 - k \frac{V + R_s I}{V_{oc}} - 1 \right) \quad (2.3)$$

where $k = \frac{I_{o,pd}}{I_{sc}}$, I_{sc} is the short circuit current and V_{oc} is the open circuit voltage of one

panel. The equations for calculating I_{sc} and V_{oc} are given in (Herrmann and Wiesner, 1996). The current voltage relationship of a PV module is defined by (2.3).

To avoid hot spots due to partial shading, a bypass diode is connected in antiparallel to the modeled PV module as shown in Fig 2.1b.

Applying KCL,

$$I_{pv} = I + I_d \quad (2.4)$$

where, I_{pv} is the PV current and I_d is the current through bypass diode.

Substituting (2.3) in (2.4) we get

$$I_{pv} = I_{sc} \left(1 - k \frac{V_{pv} + R_s I}{V_{oc}} - 1 \right) + I_o \left(e^{\frac{-V_{pv}}{V_T}} - 1 \right) \quad (2.5)$$

where I_o and V_T are the saturation current and thermal voltage of the bypass diode. We now eliminate I by backsubstituting (2.4) in (2.5).

$$I_{pv} = I_{sc} \left(1 - k \frac{V_{pv} + R_s \left(I_{pv} - I_o \left(e^{\frac{-V_{pv}}{V_T}} - 1 \right) \right)}{V_{oc}} - 1 \right) + I_o \left(e^{\frac{-V_{pv}}{V_T}} - 1 \right) \quad (2.6)$$

Defining $\frac{V_{pv} + R_s \left(I_{pv} - I_o \left(e^{\frac{-V_{pv}}{V_T}} - 1 \right) \right)}{V_{oc}} = x$, (2.6) becomes,

$$I_{pv} = I_{sc} (1 - k^{x-1}) + I_o \left(e^{\frac{-V_{pv}}{V_T}} - 1 \right) \quad (2.7)$$

The complete PV module with a bypass diode can now be described by (2.7) which is implicit and therefore, to plot its IV and PV characteristics, (2.7) is solved using numerical techniques in MATLAB for a vector of V_{pv} varying from 0 to V_{oc} .

As discussed, (2.7) is a non linear implicit function of I_{pv} which is really difficult to be burnt on a DSP or microcontroller. Therefore, the equation can also be modified to make it an explicit function of I_{pv} which can thereafter can be burnt on a processor.

Rearranging (2.7) and defining $I_o \left(e^{\frac{-V_{pv}}{V_T}} - 1 \right) = C$, we get

$$I_{pv} = I_{sc} - I_{sc} k^{x-1} + C \quad (2.8)$$

On simplifying (2.8) we get,

$$k^x = -\frac{k}{I_{SC}}I_{pv} + \frac{(C + I_{SC})k}{I_{SC}} \quad (2.9)$$

In the manuscript, x is defined as $\frac{V_{pv} + R_s \left(I_{pv} - I_o \left(e^{\frac{-V_{pv}}{V_T}} - 1 \right) \right)}{V_{oc}}$ therefore, k^x can be written as

$$k^x = k^{\frac{V_{pv}}{V_{OC}}} \times k^{\frac{R_s I_{pv}}{V_{OC}}} \times k^{-\frac{R_s C}{V_{OC}}} \quad (2.10)$$

Defining $k^{\frac{V_{pv}}{V_{OC}}} \times k^{-\frac{R_s C}{V_{OC}}} = M$,

$$k^x = M k^{\frac{R_s I_{pv}}{V_{OC}}} \quad (2.11)$$

substituting (2.11) in (2.9), we get,

$$k^{\frac{R_s I_{pv}}{V_{OC}}} = -\frac{k}{M I_{SC}}I_{pv} + \frac{(C + I_{SC})k}{I_{SC}M} \quad (2.12)$$

Re-writing (2.12),

$$k^{\frac{R_s I_{pv}}{V_{OC}}} = -\frac{k V_{OC}}{R_s M I_{SC}} \left(\frac{R_s}{V_{OC}} I_{pv} \right) + \frac{(C + I_{SC})k}{I_{SC}M} \quad (2.13)$$

Equation (2.13) can be written in the form as shown

$$e^y = ay + b \quad (2.14)$$

where, $y = \frac{R_s I_{pv}}{V_{OC}}$, $a = -\frac{k V_{OC}}{R_s M I_{SC}}$ and $b = \frac{(C + I_{SC})k}{I_{SC}M}$.

Equation (2.14) is one of the standard forms which can be converted into an explicit equation using Lambert functions.

Using standard Lamberts law, y can be written as,

$$y = \frac{W \left(-\frac{\ln k}{a} k^{-\frac{b}{a}} \right)}{\ln k} - \frac{b}{a} \quad (2.15)$$

where, W is the lambert operator.

Therefore, the equation for I_{pv} can be written as

$$I_{pv} = \frac{V_{OC}}{R_s} \left(\frac{W \left(-\frac{\ln k}{a} k^{-\frac{b}{a}} \right)}{\ln k} - \frac{b}{a} \right) \quad (2.16)$$

Equation (2.16) is explicit function of I_{pv} and can therefore be substituted in place of (2.7) to further arrive at MPP conditions and can be burnt in a processor for experimentation. In further discussions, (2.7) is taken as reference to derive the equations governing MPP and therefore the resulting equations are all implicit functions. However, the equations can be made explicit functions by using Lamberts operater as discussed above.

2.3 Proposed Analytical MPPT – I

In this section, the first analytical MPPT is presented followed by generalization for a $P \times N$ array. We know that, $P_{pv} = V_{pv}I_{pv}$. Differentiating, P_{pv} with respect to V_{pv} we get,

$$\frac{dP_{pv}}{dV_{pv}} = V_{pv} \frac{dI_{pv}}{dV_{pv}} + I_{pv} \quad (2.17)$$

At MPP, $\frac{dP_{pv}}{dV_{pv}}=0$, $\implies \frac{dI_{pv}}{dV_{pv}}=-\frac{I_{pv}}{V_{pv}}$. Differentiating (2.7) w.r.t V_{pv} ,

$$\frac{dI_{pv}}{dV_{pv}} = I_{sc} \left\{ \frac{-k^{x-1} \ln k}{V_{oc}} \left[1 + R_s \left(\frac{dI_{pv}}{dV_{pv}} + \frac{I_o}{V_T} e^{-\frac{V_{pv}}{V_T}} \right) \right] \right\} - \frac{I_o}{V_T} e^{-\frac{V_{pv}}{V_T}} \quad (2.18)$$

Substituting $\frac{dI_{pv}}{dV_{pv}}=-\frac{I_{pv}}{V_{pv}}$ in (2.18) and simplifying we get,

$$I_{pv} = \frac{V_{pv}I_{sc}}{V_{oc}} k^{x-1} \ln k \left[1 + R_s \left(\frac{I_o}{V_T} e^{-\frac{V_{pv}}{V_T}} - \frac{I_{pv}}{V_{pv}} \right) \right] + \frac{V_{pv}I_o}{V_T} e^{-\frac{V_{pv}}{V_T}} \quad (2.19)$$

Equation (2.19) is solved with (2.7) using numerical techniques in MATLAB to calculate the V_{pv} and I_{pv} . The concept is now extended to a small array consisting of 2 panels in series (1x2 configuration).

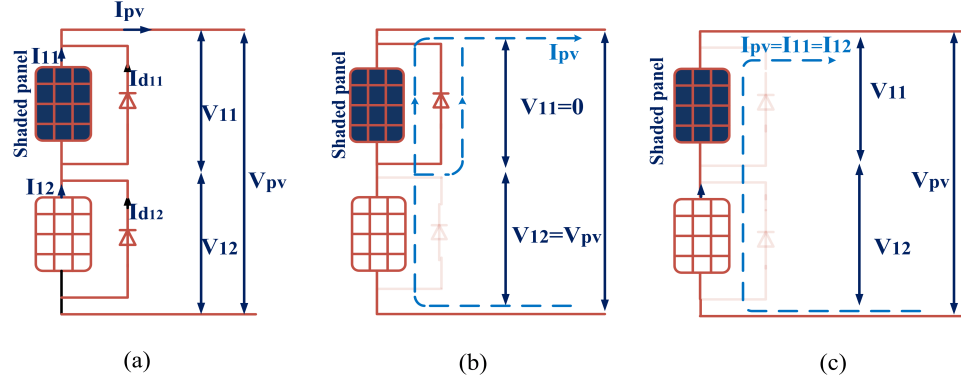


Figure 2.2: 1x2 configuration a) Schematic b) behaviour in Mode I c) Mode II

2.3.1 1×2 configuration

Fig. 2.2a shows a 1x2 configuration with two panels in series. We shall first formulate the equations that define 1x2 configuration and later derive equations for MPP conditions. Applying KVL at PV array terminal and KCL at first panel,

$$V_{pv} = V_{11} + V_{12} \quad (2.20)$$

$$I_{pv} = I_{11} + I_{d11} \quad (2.21)$$

where, V_{11} and V_{12} are voltage across module 1 and 2 respectively, V_{pv} and I_{pv} are the total PV array voltage and current respectively, I_{11} is the current through first panel and I_{d11} is the bypass diode current of the first module.

Applying the procedure as discussed for the case of single panel, (2.21) can be written as,

$$I_{pv} = I_{sc11} \left(1 - k_{11} \frac{V_{11} + R_s I_{11} - 1}{V_{oc11}} \right) + I_o \left(e^{\frac{-V_{11}}{V_{T11}}} - 1 \right) \quad (2.22)$$

simplifying (2.22),

$$I_{pv} = I_{sc11} \left(1 - k_{11}^{x_{11}} \right) + I_o \left(e^{\frac{-V_{11}}{V_{T11}}} - 1 \right) \quad (2.23)$$

where

$$x_{11} = \frac{V_{11} + R_s \left(I_{pv} - I_o \left(e^{\frac{-V_{11}}{V_{T11}}} - 1 \right) \right)}{V_{oc11}}$$

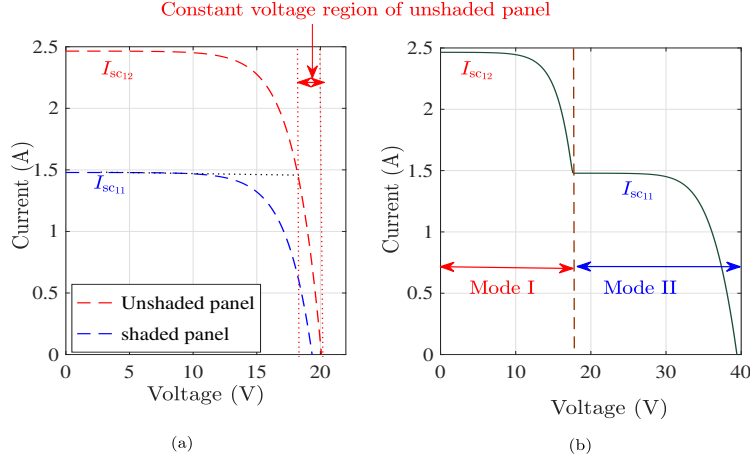


Figure 2.3: IV curves of a) individual PV panels b) combined 1x2 array
 Similar procedure is applied for the second panel and we get (2.24).

$$I_{pv} = I_{sc12} (1 - k_{12}^{x_{12}-1}) + I_o \left(e^{\frac{-V_{12}}{V_{T12}}} - 1 \right) \quad (2.24)$$

To plot IV and PV characteristics of 1×2 array, (2.20), (2.23) and (2.24) are solved for a vector V_{pv} varying from 0 to $2V_{oc}$.

Once the equations describing the array are derived, we further move to deduce equations for MPP calculation. One of the panels in 1x2 configuration is assumed to be shaded as shown in Fig. 2.2b and the corresponding IV characteristics are presented in Fig. 2.3b. It is seen from Fig. 2.3b that there exist two modes of operation, named as mode I and mode II.

The circuit behavior at two modes of operation is presented in Fig 2.2. In mode I, the current flows through an unshaded panel and bypass diode and the shaded panel. Since the current flows through the bypass diode of the shaded panel, ideally the voltage across the shaded panel is zero. In other words, $V_{pv}=V_{12}$ and the circuit behaves as if there is only unshaded panel working in a string. Once the current in the circuit reaches the short circuit value of the shaded panel, the circuit operation switches to mode II. In this mode, the current flows through the shaded and unshaded panels and $V_{pv}=V_{11}+V_{12}$. However, the voltage across the unshaded panel will remain constant throughout mode II and therefore, $V_{pv} = fn(V_{11})$. If the same panels are removed from the series connection and operated individually, their corresponding IV curves would like in Fig. 2.3a. Comparing the IV characteristics of Fig. 2.3a and Fig. 2.3b, it is clear that the IV characteristics of a 1x2 configuration are a superposition

of IV curves of their panels shifted along voltage axis.

In conclusion,

- In mode I, $V_{pv} = V_{12} \implies \frac{dV_{12}}{dV_{pv}} = 1$
- In mode II, $V_{pv} = V_{11} + V_{12}$, since V_{12} is constant, $\implies \frac{dV_{11}}{dV_{pv}} = 1$

Keeping these points in view, MPP equations are formulated. With panels receiving two different irradianations, there exists two points at which $\frac{dP}{dV}=0$ We can now state the condition where $\frac{dP}{dV} = 0 \implies \frac{dI_{pv}}{dV_{11}} = \frac{-I_{pv}}{V_{11}}$ and $\frac{dI_{pv}}{dV_{12}} = \frac{-I_{pv}}{V_{12}}$

Differentiating (2.23) and (2.24) with respect to their corresponding voltages and substituting $\frac{dI_{pv}}{dV_{11}} = \frac{-I_{pv}}{V_{11}}$ and $\frac{dI_{pv}}{dV_{12}} = \frac{-I_{pv}}{V_{12}}$,

$$I_{pv} = \frac{V_{11}I_{sc11}}{V_{oc11}}k_{11}^{x_{11}-1} \ln k_{11} \left[1 + R_s \left(\frac{I_o}{V_{T11}} e^{\frac{-V_{11}}{V_{T11}}} - \frac{I_{pv}}{V_{11}} \right) \right] + \frac{V_{11}I_o}{V_T} e^{\frac{-V_{11}}{V_{T11}}} \quad (2.25)$$

$$I_{pv} = \frac{V_{12}I_{sc12}}{V_{oc12}}k_{12}^{x_{12}-1} \ln k_{12} \left[1 + R_s \left(\frac{I_o}{V_{T12}} e^{\frac{-V_{12}}{V_{T12}}} - \frac{I_{pv}}{V_{12}} \right) \right] + \frac{V_{12}I_o}{V_{T12}} e^{\frac{-V_{12}}{V_{T12}}} \quad (2.26)$$

To calculate the first maxima, equation (2.26) is solved with (2.20), (2.23) and (2.24) and to calculate the second maxima (2.25) is solved with (2.20), (2.23) and (2.24). The maximum of the two maxima is the global maxima. This concept can similarly be extended to PV arrays of any size. Nowadays, simulation packages like MATLAB, MATHEMATICA are now available with fast converging powerful solvers which makes the solution of nonlinear equations an easier task. One such solver is “fsolve” of MATLAB which is embedded with trust region algorithms. In this thesis, fsolve is used to solve the system of equations that are derived above. The processor used for the simulation study is 8GB RAM, INTEL(R) CORE(TM) i7-4770 CPU @ 3.40 GHz. The simulation package used is MATLAB 2015a

2.3.2 P×N configuration

If V_{pn} is the voltage across n^{th} panel of p^{th} parallel path and I_p is the current through the p^{th} parallel path (I_p is the sum of p^{th} path current and the bi-pass diode).

$$V_{pv} = V_{11} + V_{12} + V_{13} + \dots + V_{1n} = V_{p1} + V_{p2} + V_{p3} + \dots + V_{pn} \quad (2.27)$$

$$I_{pv} = I_1 + I_2 + \dots + I_p \quad (2.28)$$

$$I_p = I_{sc_{pn}} (1 - k_{pn}^{x_{pn}-1}) + I_o \left(e^{\frac{-V_{pn}}{V_{T_{pn}}}} - 1 \right) \quad (2.29)$$

$$\text{where, } x_{pn} = \frac{V_{pn} + R_s \left(I_p - I_o \left(e^{\frac{-V_{pn}}{V_{T_{pn}}}} - 1 \right) \right)}{V_{oc_{pn}}}$$

Equations (2.27)–(2.29) are solved for voltage vector V_{pv} from 0 to NV_{oc} to draw IV and PV characteristics.

Differentiating (2.29) with respect to their corresponding voltage and substituting $\frac{dI_p}{dV_{pn}} = \frac{-I_p}{V_{pn}}$,

$$I_p = \frac{V_{pn} I_{sc}}{V_{oc_{pn}}} k_{pn}^{x_{pn}-1} \ln k_{pn} \left[1 + R_s \left(\frac{I_o}{V_{T_{pn}}} e^{\frac{-V_{pn}}{V_{T_{pn}}}} - \frac{I_p}{V_{pn}} \right) \right] + \frac{V_{pn} I_o}{V_{T_{pn}}} e^{\frac{-V_{pn}}{V_{T_{pn}}}} \quad (2.30)$$

For $p = 1 \dots P$ and $n = 1 \dots N$, each time (2.30) is solved with (2.27)–(2.29) to yield a vector of I_{pv} , V_{pv} and P_{pv} . The vector P_{pv} contains all the maxima points and the maximum of P_{pv} yields the MPP.

2.4 Results and Discussion

Table 2.1: PV module parameters

PV parameters	Variable	Values
Power at MPP	$P_{MPP, \text{ref}}$	74.8 W
Voltage at MPP	$V_{MPP, \text{ref}}$	17 V
Current at MPP	$I_{MPP, \text{ref}}$	4.4 A
Open circuit voltage	$V_{OC, \text{ref}}$	21.8 V
Short circuit current	$I_{SC, \text{ref}}$	4.9 A
Temperature co-efficient of V_{OC}	β	-0.33 %/°C
Temperature co-efficient of I_{SC}	α	0.04 %/°C

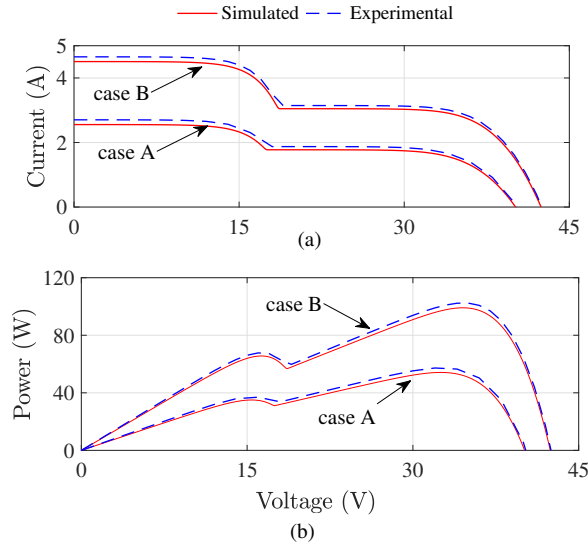
In this section, the results from the proposed model are presented and verified experimentally. The model is tested for various configurations and the necessary iteration details are provided.

2.4.1 MPP detection for 1×2 panel configuration

The proposed model at first is validated for a smaller 1x2 configuration and the panels used for modeling and experimentation is given in Table 2.1. Two cases are presented,

Table 2.2: Insolation and Temperature profile for 1×2 configuration

Case	Insolation		Temperature	
	$S_{11}(W/m^2)$	$S_{12}(W/m^2)$	$T_{11} (^{\circ}C)$	$T_{12} (^{\circ}C)$
A	360	520	35	30
B	620	920	30	25

**Figure 2.4:** Experimental and simulated a) IV curves b) PV curves

and their insolation and temperature profile is given in Table 2.2. To plot IV and PV characteristics (2.20), (2.23) and (2.24) are solved for voltage vector V_{pv} from 0 to $2V_{oc}$ in steps of 0.1 V. The simulated and experimental results for both the cases are presented in Fig. 2.4. The experimental and simulated curves are seen to have minimal errors. For both the cases, MPP detection is carried out. The simulated and experimental MPP are presented in Table 2.3. In both the cases, the experimental and simulated values are found to be an acceptable correlation. The error between simulated and experimental values are found to be 8.4% in case A and 3.324% in case B. In both the cases, the simulation time to calculate the MPP is found to be nearly 0.27–0.28 s. A screenshot of MATLAB command window displaying the necessary iteration details of case A is shown in Fig. 2.5. It can be seen that case A requires 09 iterations to converge with the first-order optimality of 6.33×10^{-17} . The command window also displays that the necessary tolerance condition has been met and hence the equation is solved. The detected MPP (displayed as Pmax in the command window) is found to be 54.15 W with an elapsed time of 0.2790 s.

Table 2.3: Tabulation of MPP along with detection time and iterations for 1×2 configuration

Case	Power at MPP (W)			Simulated	
	Simulated	Experimental	% Error	Detection time (s)	Iterations
A	54.15	59.12	8.4	0.2790	09
B	99.08	102.48	3.324	0.2814	08

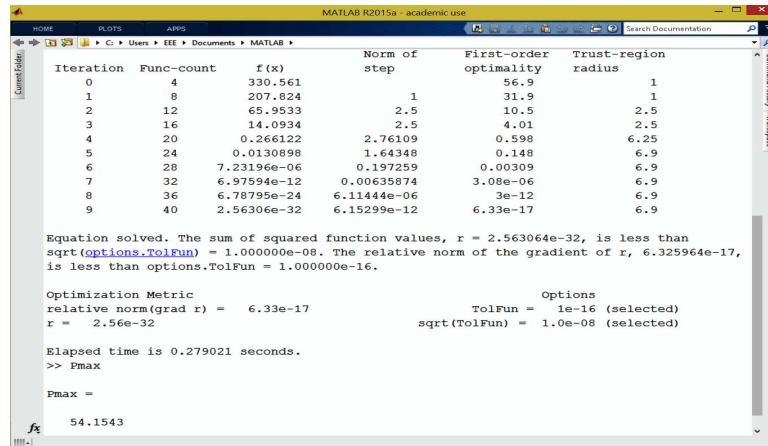


Figure 2.5: Screenshot of MATLAB command window showing iteration details for case A

2.5 Proposed Analytical MPPT – II

Once the equations which relate insolation/temperature levels to PV voltage and currents are derived in section 2.2, equations that detect the maximum power point are mathematically formulated in yet another approach. The equations governing maximum power point formulated here is based on “mean value theorem” (Bartle and Sherbert, 2000), which states, for any real-valued function $f(x)$, there exists a point x^* , such that $f(x^*) = m$, where m is the slope of line joining two arbitrary points in $f(x)$.

Based on this inference, authors in (Rodriguez and Amaratunga, 2007) have analytically proved a proposition for a uniform irradiance condition that, the point V_{pv}^* satisfying (2.31) and its corresponding I_{pv}^* are enclosed within a ball of radius which also contains MPP $[V_{MPP}, I_{MPP}]$. Such a neighborhood is defined by (2.32).

$$\left. \frac{dI_{pv}}{dV_{pv}} \right|_{v_{pv}^*} = -\frac{I_{sc}}{V_{oc}} \quad (2.31)$$

where,

$$I_{pv} = -\frac{I_{SC}}{V_{OC}}V_{pv} + I_{SC}$$

I_{pv} is a straight line joining $(0, I_{SC})$ and $(V_{OC}, 0)$.

$$|(V_{pv}^* + I_{pv}^* R_s) - (V_{MPP} + I_{MPP} R_s)| \leq \zeta \quad (2.32)$$

where ζ is a very small number.

In other words, If a tangent is drawn to an IV curve whose slope is same as the straight line joining the open circuit and short circuit points $(0, I_{SC})$ and $(V_{OC}, 0)$. The point of intersection of the tangent and the IV curve lies in the vicinity of MPP (V_{pv}^*, I_{pv}^*) . as shown in Fig 2.6.

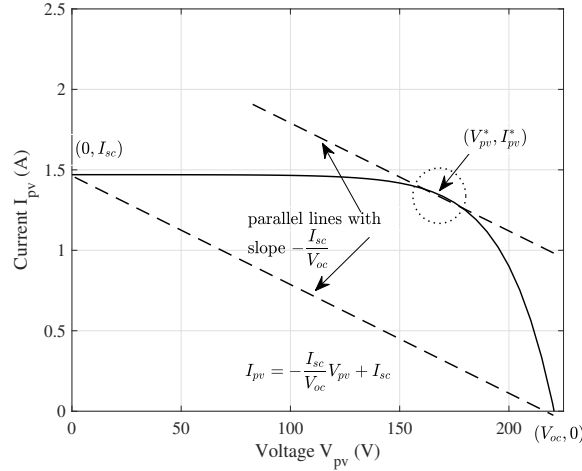


Figure 2.6: I-V curves under uniform shading condition indicating slopes

2.5.1 1×2 configuration

The concept is now extended to PV arrays under partial shading conditions. Unlike uniform shading conditions, partial shading conditions have multiple peaks in its PV curve. These multiple maxima make the formulation slightly complex. The proposed MPP is based on the fact that, the number of local MPP points in the IV and PV characteristics is equal to the number of panels receiving different irradiancies. If two or more panels in the same string receive similar irradiation, it is grouped as a zone.

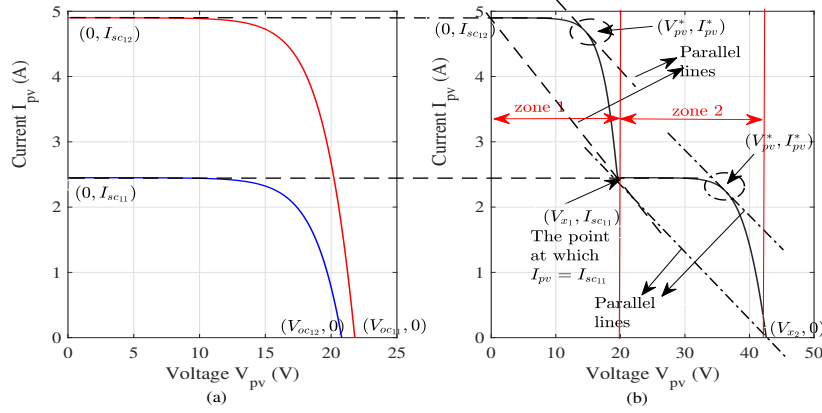


Figure 2.7: I-V curves indicating slopes when a) operating independently b) in series

Therefore, the entire string can be grouped into different zones based on the irradiance levels. Once the zones are formed, the proposition in (Rodriguez and Amaratunga, 2007) is applied to each zone. The IV curve of two series panels receiving non-uniform irradiance, divided into 2 zones is shown in Fig 2.7b.

In case of uniform shading, application of mean value theorem is straightforward as the slope of straight line joining $(0, I_{SC})$ and $(V_{OC}, 0)$ is only dependent on I_{SC} and V_{OC} values. However, in case of partial shading conditions as shown in Fig 2.7b, calculation of slopes in each zone is not just dependent on I_{SC} and V_{OC} but also on other intermediate variables. To understand this, we will look into how a 1x2 array behaves when we sweep the voltage from short circuit to open circuit levels. The current flow through 1x2 configuration during two zones is shown in Fig 2.2. During the first zone, the current flows through the panel receiving the higher irradiation and further divides between the bypass diode of other panel. The voltage across the panel receiving lower irradiation is zero ($V_{11} = 0$ and $V_{pv} = V_{12}$). Therefore, the entire PV voltage is across the other panel. As the voltage is swept, the current keeps decreasing and at certain voltage where the PV current equals to the short circuit value of the panel receiving lower irradiation, the current now starts flowing through both the panels. However the voltage across the panel receiving higher irradiation is now constant which means, though $V_{pv} = V_{11} + V_{12}$, $V_{pv} = fn(V_{11})$. This also means that only one panel is active in each zone.

In summary,

- In zone I, $V_{pv} = V_{12} \implies \frac{dV_{12}}{dV_{pv}} = 1 \implies \frac{dI_{pv}}{dV_{12}} = \frac{dI_{pv}}{dV_{pv}}$

- In zone II, $V_{pv} = V_{11} + V_{12}$, since V_{12} is constant, $\implies \frac{dV_{11}}{dV_{pv}} = 1 \implies \frac{dI_{pv}}{dV_{11}} = \frac{dI_{pv}}{dV_{pv}}$

If we look into IV characteristics of Fig 2.7b, we see observe the same phenomena. The curves in Fig 2.7a are the individual IV curves of two panels operating independently. If the panels are now connected in series, the IV curves look as in Fig 2.7b. From the figure, it is clear that the IV curve of series connected panels is the superposition of IV curves of individual panels shifted along voltage axis. The two IV curves superpose at the point where the PV array current becomes equal to short circuit current level of the lower irradiated panel. The voltage at which this happens is termed as V_{x_1} and the coordinates are (V_{x_1}, I_{sc11}) .

With this background, mean value theorem is applied to each zone, starting with zone one. The equation of the line joining $(0, I_{SC12})$ and (V_{x_1}, I_{SC11}) is given by

$$I_{pv} = \frac{I_{SC11} - I_{SC12}}{V_{x_1}} V_{pv} + I_{SC12} \quad (2.33)$$

The slope of (2.33) is $\frac{I_{SC11} - I_{SC12}}{V_{x_1}}$. We now draw a line tangent to the IV curve such that the slope of the tangent is equal to $\frac{I_{SC11} - I_{SC12}}{V_{x_1}}$. The point of intersection of IV curve and the tangent gives the co-ordinates of the local maxima. To calculate the point of intersection, we differentiate (2.24) with respect to V_{pv} . However, in zone 1, $V_{pv} = V_{12}$. Therefore, $\frac{dV_{12}}{dV_{pv}} = 1$. The final resulting equation is (2.34).

$$\frac{dI_{pv}}{dV_{pv}} = -\frac{I_{SC12} k_{12}^{x_{12}} \ln k_{12}}{V_{OC12}} \left(1 + R_s \left(\frac{dI_{pv}}{dV_{12}} + \frac{I_o}{V_T} e^{-\frac{V_{12}}{V_T}} \right) \right) - \frac{I_o}{V_T} e^{-\frac{V_{12}}{V_T}} \quad (2.34)$$

Equating the slope of tangent with (2.34), we get

$$\frac{I_{sc12} - I_{sc11}}{V_{x_1}} = \frac{I_{SC12} k_{12}^{x_{12}} \ln k_{12}}{V_{OC12}} \times \left(1 + R_s \left(\frac{dI_{pv}}{dV_{12}} + \frac{I_o}{V_T} e^{-\frac{V_{12}}{V_T}} \right) \right) + \frac{I_o}{V_T} e^{-\frac{V_{12}}{V_T}} \quad (2.35)$$

Equation (2.35) is solved with (2.20), (2.23), (2.24) using numerical techniques to give the co-ordinates of local MPP.

Since V_{x_1} is the array voltage at which $I_{pv} = I_{SC11}$, we substitute $I_1 = I_{SC11}$ in (2.20), (2.23), (2.24) and solve for V_{pv} .

Similar technique is applied in zone 2. The equation of the line joining (V_{x_1}, I_{SC11})

and $(V_{x_2}, 0)$ is given by (2.36).

$$I_{pv} = -\frac{I_{SC11}}{V_{x_2} - V_{x_1}} V_{pv} + \frac{I_{SC11} V_{x_1}}{V_{x_2} - V_{x_1}} + I_{SC11} \quad (2.36)$$

The slope of the (2.36) is equated with the slope of the IV curve to calculate the co-ordinates of the second local MPP. Differentiating (2.23) with respect to V_{pv} and equating with $-\frac{I_{SC11}}{V_{x_2} - V_{x_1}}$ we get (2.37).

$$-\frac{I_{SC11}}{V_{x_2} - V_{x_1}} = \frac{I_{SC11} k_{11}^{x_{11}} \ln k_{11}}{V_{OC11}} \times \left(1 + R_s \left(\frac{dI_{pv}}{dV_{11}} + \frac{I_o}{V_T} e^{-\frac{V_{11}}{V_T}} \right) \right) + \frac{I_o}{V_T} e^{-\frac{V_{11}}{V_T}} \quad (2.37)$$

Equation (2.37) is solved with (2.20), (2.23), (2.24) using numerical techniques to gives the coordinates of local second MPP. Once the coordinates of the local MPP are calculated, the local peak power can be computed. From the local peaks, the maximum of the local peaks gives the global peak.

Since V_{x_2} is the array voltage at which I_{pv} becomes zero, we substitute $I_{pv}=0$ in (2.20), (2.23), (2.24) and solve for V_{pv}

2.5.2 $P \times N$ configuration

A similar procedure can be applied to a $P \times N$ array. The array consisting of N panels in each of the P parallel path is described by (2.27) - (2.29). An array consisting of N series panels, the maximum possible peaks are also N and this happens only if each of the panel receives different irradianations. To explain the MPP process with ease, we shall assume that in an array, the panels receive irradiation in the decreasing order of their positions. Example: In P^{th} parallel path, let, $S_{p1} > S_{p2} > \dots > S_{pn}$. When PV panels are connected in parallel, the PV characteristic of the entire PV array is nothing but superposition of PV characteristic of each of the strings. Therefore, in each zone only one panel is active in each string. This continues till the current in each string reaches the short circuit current level of the panel receiving next highest irradiation. The total PV current at this point (zone I) is now $I_{SC12} + I_{SC22} + I_{SC32} \dots + I_{SC_{p2}}$. This marks the start of zone II where the first panels in each string reaches its open circuit voltage and the second panels gets active. This continues till end of zone II where the current reaches $I_{SC13} + I_{SC23} + I_{SC33} \dots + I_{SC_{p3}}$. The same process continues till the total PV current becomes zero. Therefore, with N

such zones, we get N peaks. The objective here is to calculate the intersection point of the tangent (whose slope is same as the line joining the open circuit and short circuit points) with the PV curve in each zones. If $m_1 \dots \dots m_n$ are the slopes of the tangent in each zone, then

- $\frac{di_{pv}}{dv_{pv}} = m_1$ in zone one
- $\frac{di_{pv}}{dv_{pv}} = m_2$ in zone two
- \dots
- $\frac{di_{pv}}{dv_{pv}} = m_n$ in zone N

the slope of the straight lines in each of the zones are given by

$$m_1 = \frac{\sum_{p=1}^{p=P} I_{SC_{p2}} - \sum_{p=1}^{p=P} I_{SC_{p1}}}{V_{x_1}} \quad (2.38)$$

$$m_2 = \frac{\sum_{p=1}^{p=P} I_{SC_{p3}} - \sum_{p=1}^{p=P} I_{SC_{p2}}}{V_{x_2} - V_{x_1}} \quad (2.39)$$

...

...

$$m_n = \frac{-\sum_{p=1}^{p=P} I_{SC_{pn}}}{V_{x_n} - V_{x_{n-1}}} \quad (2.40)$$

where, $V_{x_1} \dots V_{x_n}$ are the value of PV voltages at $\sum_{p=1}^{p=P} I_{SC_{p2}} \dots 0$. Once the values of slopes are found out, we further derive the generalized expression for $\frac{dI_{pv}}{dV_{pv}}$. From (2.28), we know that, $I_{pv} = I_1 + I_2 + \dots \dots + I_p$. Differentiating (2.28) with respect to V_{pv} we get,

$$\frac{dI_{pv}}{dV_{pv}} = \frac{dI_1}{dV_{pv}} + \frac{dI_2}{dV_{pv}} + \dots \dots + \frac{dI_p}{dV_{pv}} = \sum_{p=1}^{p=P} \frac{dI_p}{dV_{pv}} \quad (2.41)$$

In zone I, $V_{pv} = V_{p1} \implies \frac{dV_{p1}}{dV_{pv}} = 1 \implies \frac{dI_{pv}}{dV_{p1}} = \frac{dI_{pv}}{dV_{pv}}$

In zone II, $V_{pv} = V_{p1} + V_{p2}$, since V_{p1} is constant, $\implies \frac{dV_{p2}}{dV_{pv}} = 1 \implies \frac{dI_{pv}}{dV_{p2}} = \frac{dI_{pv}}{dV_{pv}}$

In zone N, $V_{pv} = V_{p1} + V_{p2} \dots V_{pn} \implies \frac{dV_{pn}}{dV_{pv}} = 1 \implies \frac{dI_{pv}}{dV_{pn}} = \frac{dI_{pv}}{dV_{pv}}$ Differentiating (2.29) wrt V_{pv} at each of the zones with appropriate zone conditions we get (2.42).

$$\frac{dI_{pv}}{dV_{pv}} = - \sum_{p=1}^{p=P} \left(\frac{I_{SC_{pn}} k_{pn}^{x_{pn}-1} \ln k_{pn}}{V_{OC_{pn}}} \left(1 + R_s \left(\frac{dI_p}{dV_{pn}} + \frac{I_o}{V_T} e^{-\frac{V_{pn}}{V_T}} \right) \right) + \frac{I_o}{V_T} e^{-\frac{V_{pn}}{V_T}} \right) \quad (2.42)$$

Table 2.4: Insolation and temperature for 1×2 configuration

Case	Insolation		Temperature	
	$S_{11}(W/m^2)$	$S_{12}(W/m^2)$	$T_{11} (^{\circ}C)$	$T_{12} (^{\circ}C)$
A	360	520	35	30
B	540	625	33	28
C	620	920	30	25

At each zone, (2.42) is solved with (2.27) - (2.29) to obtain all MPPs. The maximum value amongst all the MPP is the global MPP.

2.6 Results and Discussion

The proposed model at first is validated for a smaller 1x2 configuration. Three cases are presented, and their insolation and temperature profile is given in Table 2.4. To plot IV and PV characteristics (2.20), (2.23) and (2.24) are solved for voltage vector V_{pv} from 0 to NV_{oc} in steps of $0.1V_{pv}$. The screenshots from Matlab command window asking for various inputs from user such as datasheet parameters, array configuration, insolation, temperature is shown in Fig 2.9(a). There is also provision for the user to choose to just calculate global MPP or plot its VI characteristics. The screenshot also shows that the user has entered the details of case B of Table 2.4. The screenshot image in Fig 2.9(b) shows the result for the parameters entered in Fig 2.9(a). The system of equations takes six iterations to converge at the solution point with function value $f(x)$ as small as 1.28741×10^{29} within a span of 0.3495 s. The detected global peak is 78.3157 W. The screenshot of MATLAB command window for IV and PV characteristics is shown in 2.9(c). It is seen that the numerical equation solver has stalled the program because the required criteria is met and that the system of equations have converged to solution point. It also shows the time taken to plot the characteristics. It has taken 7.23 s to plot the characteristics with a step of 0.1 V containing 436 data points. It means that the system of non linear equations are solved 436 times in a span of just 7.23 s. The screenshot also shows the image of IV and PV

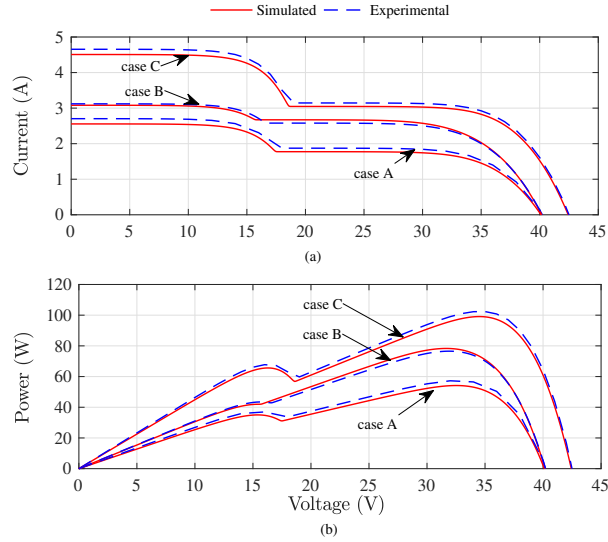


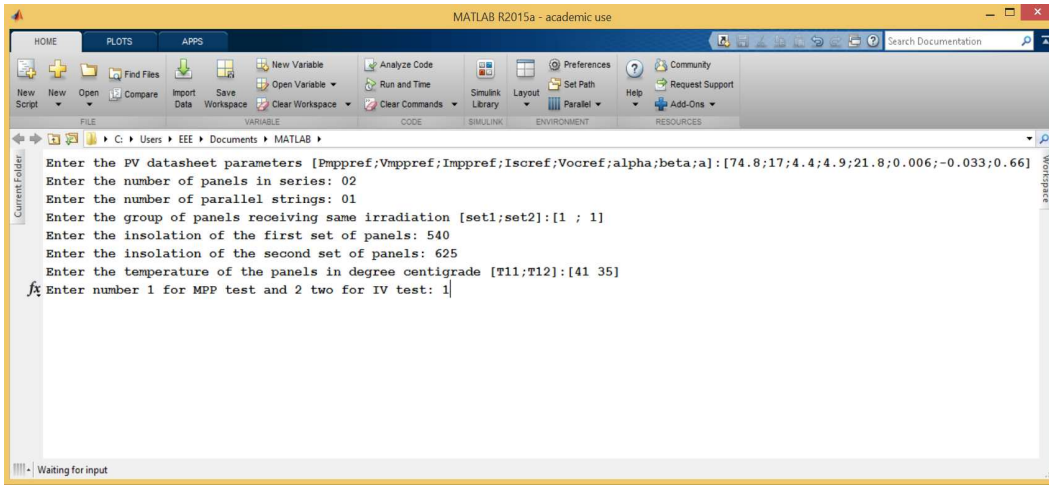
Figure 2.8: Experimental and simulated a) IV curves b) PV curves

Table 2.5: Tabulation of MPP along with detection time and iterations for 1×2 configuration

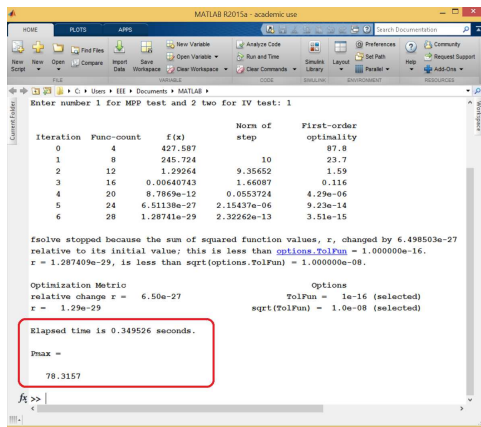
Case	Power at MPP (W)			MPP detection time (s)	Iterations
	Simulated	Experimental	% Error		
A	55	59.12	6.96	0.28	08
B	78.31	76	3.04	0.3495	06
C	97	102.48	5.34	0.27	08

characteristics plotted by MATLAB where peak power is seen to be approximately 80 W, which is same as the one calculated by the proposed algorithm in Fig. 2.9(b). The simulated and experimental results for other two cases along with case B are presented in Fig. 2.8. Experimental IV and PV characteristics are plotted using “HT IV400” IV tracer in voltage sweep mode. The experimental and simulated curves are seen to have minimal errors. For both the cases, MPP detection is carried out. The simulated and experimental MPP are presented in Table 2.5. In all the cases, the experimental and simulated values are found to be in acceptable correlation. The error between simulated and experimental values are found to be 6.96% in case A and 3.044% in case B and 5.34 % in case C. In all the cases, the simulation time to calculate the MPP is found to be nearly 0.27–0.34 s.

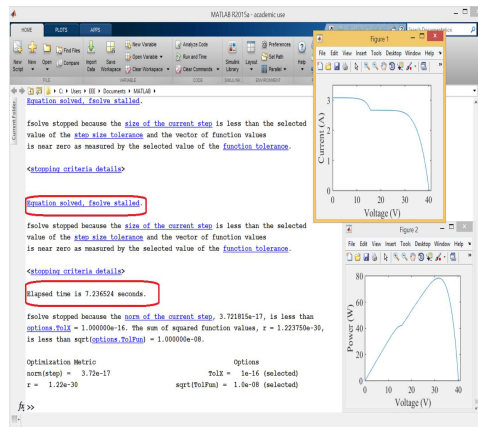
To show the simulation capability of the proposed model, the shading on three



(a)



(b)



(c)

Figure 2.9: Screenshots from MATLAB command window for case B showing a) showing how inputs are fed to a generalized model b) MPP along with elapsed time c) IV and PV curves along with elapsed time

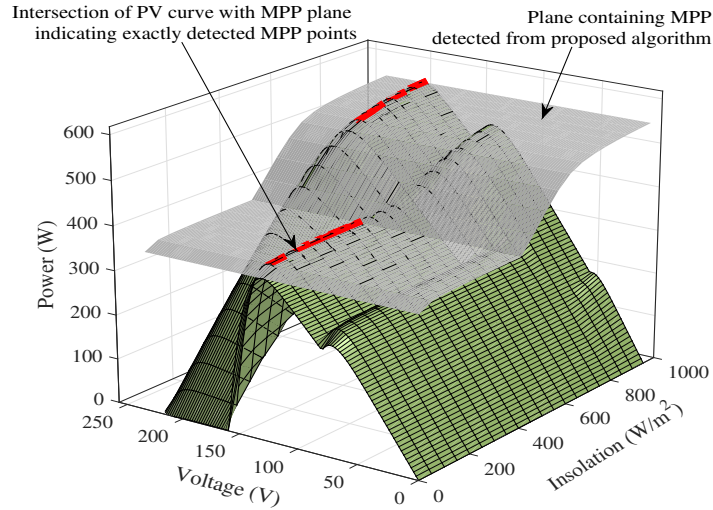


Figure 2.10: A 3D view showing the intersection of PV curves and, the plane containing MPP detected from proposed algorithm

panels out of 11 panels are varied continuously. For each shading pattern, MPP test and IV, PV characteristic test are performed resulting in a PV mesh and a plane containing MPP . The intersection of MPP plane obtained from proposed algorithm and the PV mesh shows that the MPP detected by the proposed algorithm is true to most of the patterns considered. The intersection of PV mesh and MPP plane is shown in Fig. 2.10.

The proposed technique is now tested with a full day irradiation data. The irradiation data along with the simulated MPP is presented in Fig 2.11. The irradiation data is obtained from National Solar Irradiation Laboratory (NREL)(NREL, 2017) measured on March 18, 2017, at a 39.74° N latitude and 105.18° W longitude. The irradiance was measured from 00.00 hrs to 24.00 hrs at a rate of 1 min. This insolation data was fed to the proposed model with 1x11 configuration to extract the MPP. It is seen that the proposed model could successfully calculate MPP at all the irradiance levels. The entire simulation took 7 min 44s which involved 1440 (1m x 60 x 24) irradiation data points.

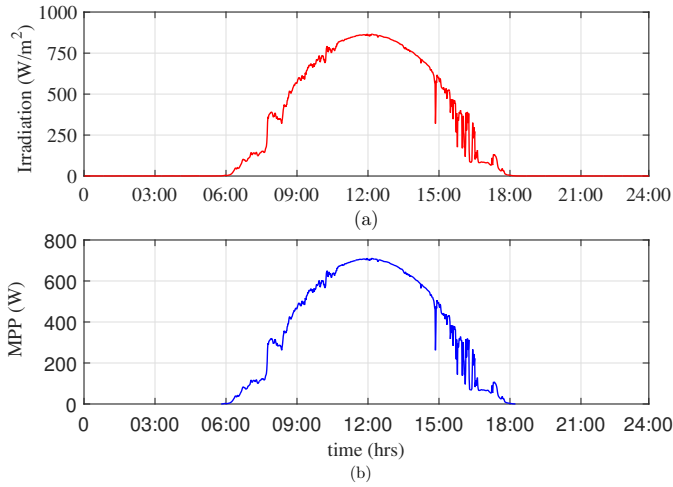


Figure 2.11: Calculation of MPP for one day Irradiation data

2.7 Comparison of proposed MPPTS

In this section, the results from both the proposed methods are compared for a medium sized and larger arrays, and the MPP values are tabulated.

2.7.1 Medium sized PV arrays

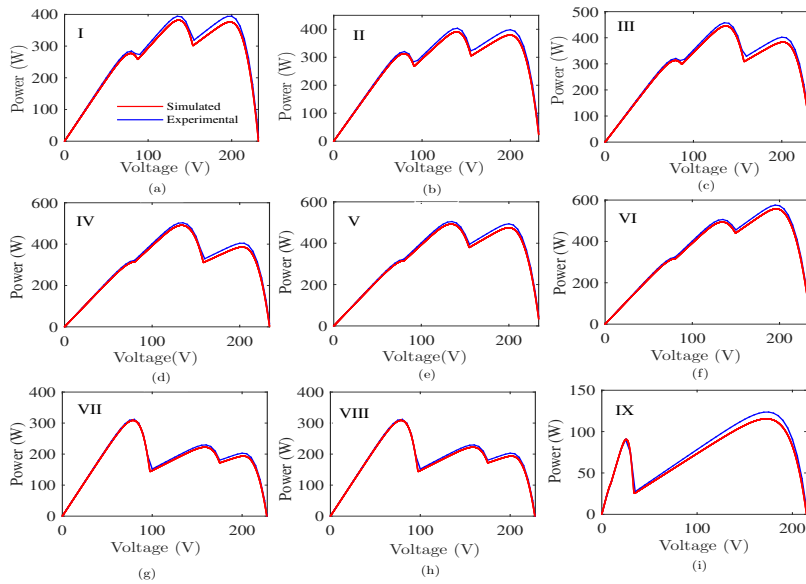


Figure 2.12: Experimental Validation of simulated PV curves

Table 2.6: Tabulation of MPP calculated from method I and II

Shading Pattern	Power at MPP (W)				
	Method I	Method II	Experimental	% Error ₁	% Error ₂
I	381.80	380	394.24	3.155	3.61
II	390.62	389.9	403.65	3.21	3.41
III	445.12	445.1	457.44	2.69	2.7
IV	491.05	490.8	503.39	2.45	2.5
V	492.32	491.5	504.7	2.45	2.62
VI	557.30	557.2	575.54	3.16	3.18
VII	308.5	308	318.37	3.1	3.257
VIII	228.6	227.89	236.27	3.28	3.54
IX	114.8	114.5	118.8	3.38	3.61

Fig. 2.12 shows the simulated PV characteristics of nine shading patterns for a 1×11 configuration. The simulated PV curves are also verified experimentally. All of these nine shading patterns are fed to the proposed algorithms and the MPP detected are presented in Table 2.6. It can be seen that the proposed algorithms track MPP with error not exceeding 4% in any case. Here Error₁ is the error between MPP detected from Method I and Experimental and Error₂ is the error between MPP detected from Method II and Experimental.

2.7.2 Larger Arrays

In this section, the MPP detection for larger arrays is presented. A set of four

Table 2.7: Tabulation of MPP calculated from method I and II for larger arrays

Panel size	Power at MPP (W)				
	Method I	Method II	Experimental	% Error ₁	% Error ₂
2x9	488	489	502.6	3.01	2.70
2x11	574	580	588.92	2.47	1.51
2x15	793	790	812.42	2.47	2.60
9x9	2620	2600	2699.9	3.05	3.67

different panel sizes is chosen here and their corresponding PV characteristics are presented in Fig 2.13. The experimental plots are also presented to validate the simulated characteristics. The simulated and experimental characteristics are found to be in agreement with each other for all the patterns considered. This shows that the proposed PV model is capable of simulating PV curves with a large number of

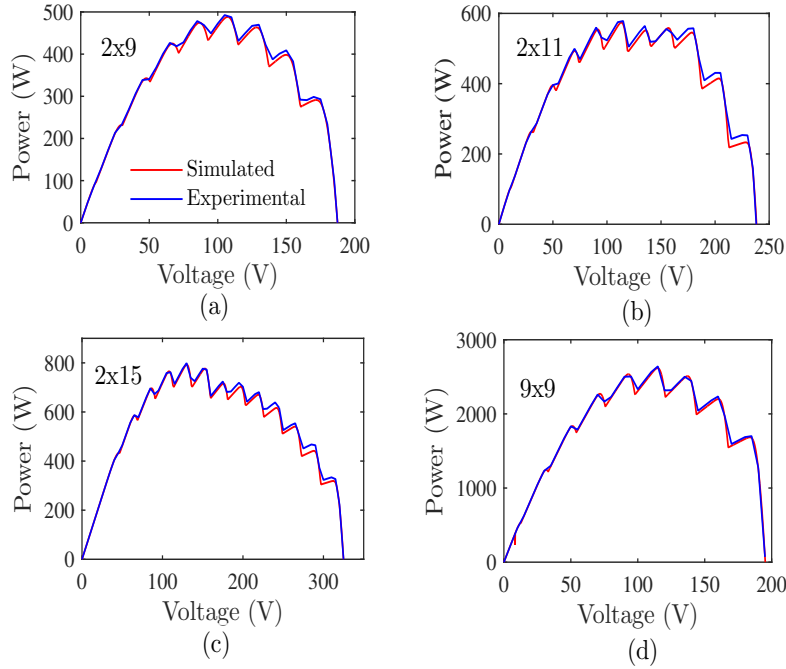


Figure 2.13: Experimental and simulated PV curve with more number of peaks

peaks. Therefore, it can be used to simulate larger PV arrays with N number of peaks. The simulated and experimental values of MPP calculated from both the proposed methods are given in Table 2.7. It can be seen that both proposed methods could detect an MPP in all the cases with an error, not more than 4%. A case of 2x15 panels is chosen with 14 peaks is shown in Fig 2.13c. The proposed models could detect the MPP amongst the 14 peaks with an error lesser than 3%. To validate the proposed model for a case with large strings, a 9x9 array is considered in Fig 2.13d. The proposed models could detect the global peak with an error less than 4%.

2.8 Conclusion

In this chapter, two iterative analytical model for calculating MPP under partial shading conditions are presented. The developed models are capable of detecting MPP with any number of peaks. Several illustrations are presented and results are verified with experimental studies. Convergence and simulation details are provided to ensure the effectiveness of the proposed model. Results from the simulation are found to be in agreement with the experimental results. Finally, a comparative study

of both the proposed methods are presented. It is seen both the proposed algorithms can track MPP with error not exceeding 4% in any case and therefore, any of these proposed algorithms can be incorporated in water pumping systems to detect MPP. In the next chapter, analytical method proposed in section 2.3 is used to track MPP in Induction motor water pumping system.

Chapter 3

Modeling and Analysis of Power converter and Inverter fed Motor Pump System

Contents

3.1	Introduction	46
3.1.1	Objectives	46
3.2	Framework of the Objective	46
3.2.1	Effect of duty cycle on boost converter performance	49
3.2.2	Effect of C on boost converter performance	50
3.2.3	Effect of L on boost converter performance	51
3.3	Steady state Modeling of power converter and Induction motor pump	53
3.3.1	Duty cycle calculation	53
3.3.2	Induction motor and Pump	55
3.3.3	Solution of Non linear Equations	57
3.4	Dynamic modeling of Power converter and Induction Motor	58
3.4.1	Dynamic model of boost converter	58
3.4.2	Dynamic model of inverter	60
3.4.3	Dynamic model of Induction motor and pump	61

3.5 Results and Discussion	61
3.6 Conclusion	70

3.1 Introduction

In the previous chapter, modeling of PV panels along with two analytical MPPTs are presented. It is seen that both the MPPT techniques could track the global MPP with error less than 4% for all the presented cases. In this chapter, modeling of boost converter, inverter and induction motor pump system is presented. Equations governing the power converters and induction motor pump system are derived and solved with the MPPT algorithms developed in Chapter 2 to evaluate the performance of water pumping systems under partial shading conditions. This research work thus helps in understanding the detrimental effects these partial shading might cause on the entire water pumping systems if the conditions are overlooked and thus serves as a reference tool for practitioners who wish to study PV fed pumps.

3.1.1 Objectives

Given the above discussions, the objectives of this chapter are

- It showcases the effects of partial shading on two-stage water pumping systems (system with a boost converter, inverter and induction motor pump) with several shading illustrations.
- It experimentally verifies that the converter may have to operate at higher duty cycles to meet the DC bus requirement. To avoid the high duty cycles, the converter may also operate at discontinuous modes which reduce the efficiency of operation to such a lower extent that the pump may even fail to operate though sufficient power is available at the PV terminals.

3.2 Framework of the Objective

We start the framework with the sizing of PV panels, intermediate power converters as per the requirement of the water pump. The rating of the IM water pump considered here is 1 HP (745 W). The parameters of the chosen motor are given in Table 3.1.

Table 3.1: IM pump parameters

IM parameters	Variable	Values
Connection		Delta
Rated Motor voltage (L-L)	$V_{m_{rms}}$	230 V
Rated frequency	f_{rated}	50 Hz
Rated speed	N_r	2700 rpm
Stator & Rotor resistances	R_s & R_r	9.5 Ω & 13.68 Ω
Stator & Rotor leakage reactances	L_{ls} & L_{lr}	0.0295 H each
Magnetising inductance	L_m	0.878 H
Poles	P	02
Pump constant	k	33.181 μ W/(rad/s) ³

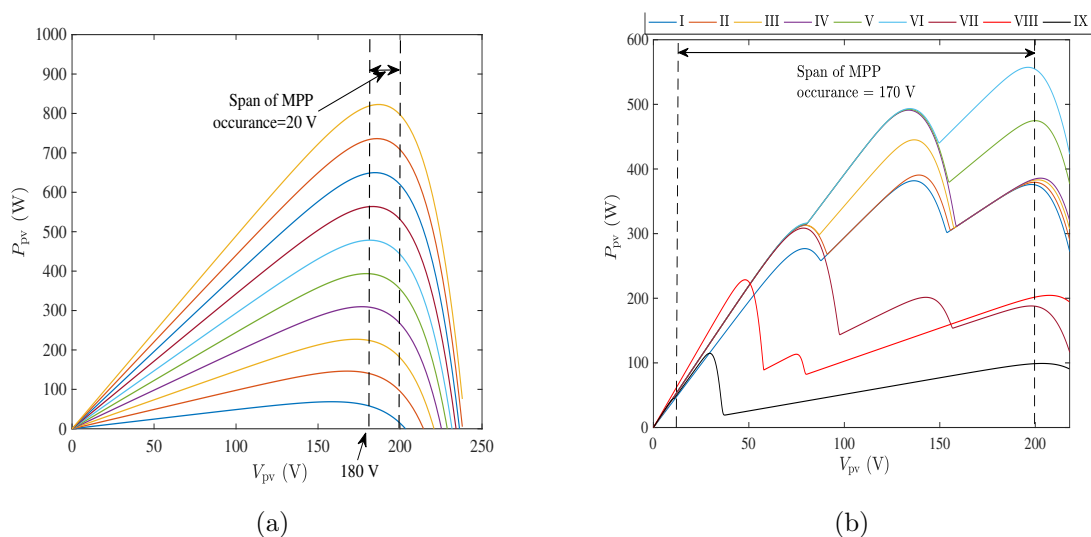


Figure 3.1: PV curves indicating span of MPP occurrence for a) Uniform shading b) shading conditions

Considering a motor of rating 1 HP with an efficiency of 90 %, the motor draws an input power of 828 W from the supply at rated load. If PV panel of rating 74.8 W (rated as power delivered by panels at MPP at 1000 W/m²) is considered, we require 11 panels so that the power available is 74.8 W \times 11 = 822.8 W which is sufficient to feed the motor at rated conditions. The PV panel datasheet parameters are given in Table 2.1. This power from the panels is in DC and therefore, to feed the IM pump we use an intermediate inverter. The inverter needs a minimum DC voltage at its DC side to feed the IM pump system. The DC bus requirement for an inverter with space vector modulation (SVM) is given by (3.1)(Mohan and Undeland, 2007).

Table 3.2: Insolation profile for the panels considered for simulation. Temperature (T)=35° C for all cases

panels → shading ↓ pattern	1	2	3	4	5	6	7	8	9	10	11
I	400	400	400	600	600	600	800	800	800	800	800
II	400	400	400	600	600	600	900	900	900	900	900
III	400	400	400	700	700	700	900	900	900	900	900
IV	400	400	400	800	800	800	900	900	900	900	900
V	500	500	500	800	800	800	900	900	900	900	900
VI	600	600	600	800	800	800	900	900	900	900	900
VII	900	900	900	900	900	200	200	300	300	300	300
VIII	1000	1000	1000	250	250	250	250	300	250	250	250
IX	150	150	150	150	150	150	150	150	150	900	800

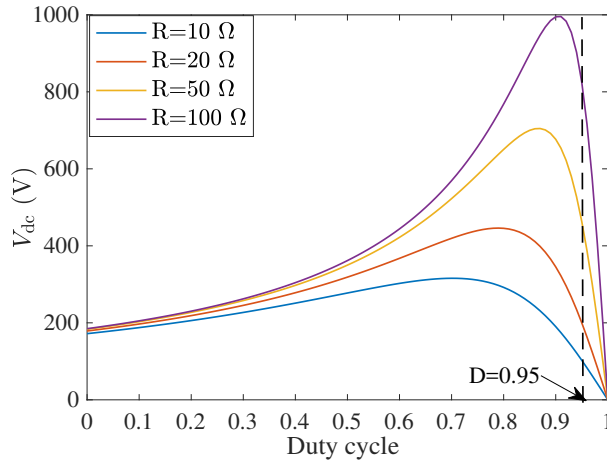


Figure 3.2: Variation of V_{dc} with duty cycle for various loads

$$V_{dc} = \frac{2 \times \sqrt{2} \times V_{m_{rms}}}{1.15 \times \sqrt{3} \times m_a} \quad (3.1)$$

where, m_a is the modulation index that varies between 0-1. For a motor with $V_{m_{rms}} = 230$ V, the required minimum $V_{dc} = 340$ V. This means a minimum of 350 V should be maintained at the DC bus of the inverter to feed the IM pump system (The DC bus requirement increases to 587 V for a star connected motor with $V_{m_{rms}} = 415$ V). However, the maximum voltage at MPP available from the panels is $17 \text{ V} \times 11 = 188$ V ($V_{MPP,ref} \times \text{number of panels in series}$). Since there is a mismatch between the available DC voltage from panels and the V_{dc} , we use another intermediate DC–DC boost converter.

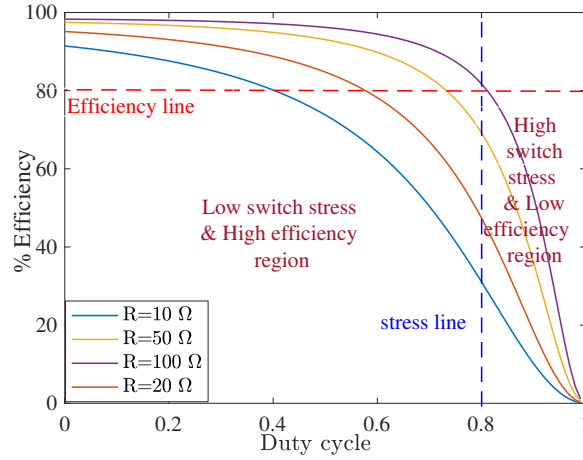


Figure 3.3: Variation of efficiency of boost converter with duty cycle

3.2.1 Effect of duty cycle on boost converter performance

For a boost converter, the approximate duty cycle required to maintain V_{dc} of 350 V is given by (3.2)(Mohan and Undeland, 2007). In case of uniform shading conditions, when the insolation (S) is varied from $100 W/m^2 - 1000 W/m^2$, the PV curves are as shown in Fig 3.1(a). It can be observed that over an entire range of insolation, the MPP occurrence lie somewhere between narrow band of just 180 V – 200 V, i.e., when the insolation is varied over a wide range, the location of MPP is within 20 V range (200 V-180 V=20 V) and the region between which the MPP occurs is termed here as span of MPP. Therefore, in case of uniform shading, the span of MPP is just 20 V. If a voltage of 350 V should be maintained across the DC bus, according to (3.2), we need a duty cycle (D) of 0.468.

$$V_{dc} = \frac{V_{MPP}}{1 - D} \quad (3.2)$$

In case of PSC, the PV characteristics are as shown in Fig 3.1(b). In Fig 3.1(b), the legends written in roman letters I, II, III ... indicate the various shading patterns. The insolation and temperature of all shading patterns is presented in Table 3.2. We have considered cases where peak can occur to the left, middle and towards the right side on a voltage axis. It is seen that, unlike uniform shading conditions, the value of V_{MPP} can lie anywhere between 17.44 V to 188 V ($0.8 V_{OC}-0.8 \times N \times V_{OC}$), where N is the number of panels in series. If MPP occurs somewhere at 17.44 V, the required

D will be as high as 0.95. If a plot of V_{dc} Vs D is plotted for various loads as shown in Fig 3.2 (the equations required to plot Fig 3.2 are presented in the next section), it can be seen that duty cycles above 0.95 are not a preferred region of operation as there is uncertainty in maintaining higher V_{dc} values and this uncertainty of boosting up to higher V_{dc} is a function of load. If a plot of efficiency of boost converter vs duty cycle is plotted as shown in Fig 3.3, it can be seen that, the region to the right of $D=0.8$ and below the efficiency line of 80 % (80 % is assumed to be the worst possible efficiency) is considered a region of high switch stress and low efficiency. With conclusions drawn from Fig. 3.2 and 3.3, it can be seen that for any load, duty cycle above 0.8 is considered as an unfeasible operation region and it is always safe to operate the converter at duty cycles lesser than 0.8. With the value of peaks occurring around regions of 0.8 V_{OC} , it is not feasible to operate converters in MPP mode as not only uncertain to maintain V_{dc} but increases stress across the IGBT/MOSFET and the efficiency drops considerably.

We now move to study the effect of boost inductor (L) and capacitor (C) on partial shading conditions.

3.2.2 Effect of C on boost converter performance

For a boost converter, the design equation of capacitor is given by (Mohan and Undeland, 2007)

$$C = \frac{D}{R \frac{\Delta V_{dc}}{V_{dc}} f_s} \quad (3.3)$$

where,

$$R = \frac{V_{dc}}{I_{inv}} = \frac{V_{dc}}{I_{MPP}(1-D)} = \frac{V_{dc} V_{MPP}}{P_{MPP}(1-D)} \quad (3.4)$$

where, I_{inv} is the DC side inverter current and f_s is the switching frequency of the boost converter. Substituting (3.2) in (3.4), and resubstituting the resulting equation in (3.3) we get

$$C = \frac{D P_{MPP}}{V_{dc}^2 \frac{\Delta V_{dc}}{V_{dc}} f_s} \quad (3.5)$$

For a constant V_{dc} , $f_s = 25$ kHz and $\frac{\Delta V_{dc}}{V_{dc}} = 0.01$, the value of C depends only on D and P_{MPP} . Since the maximum value of $P_{MPP}=822$ W, the capacitor value linearly depends only on D. In case of uniform shading conditions, the value of D is approximately 0.468. Therefore, the required capacitance is approximately 13 μ F.

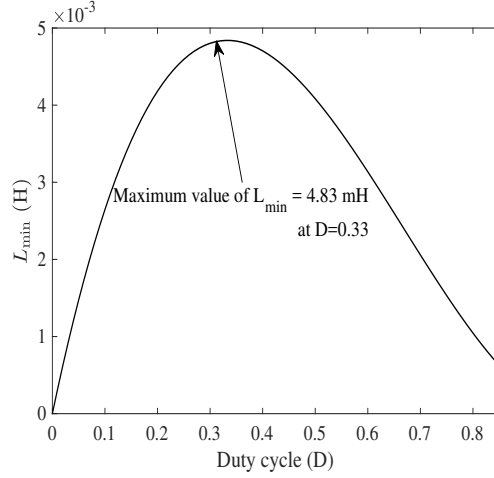


Figure 3.4: Variation of L_{\min} with duty cycle for $P_{\text{MPP}}= 70 \text{ W}$

However, in case of PSC, since the value of V_{MPP} can lie anywhere between 17.44 V to 188 V ($0.8 V_{\text{OC}}-0.8 \times N \times V_{\text{OC}}$), the duty ratio cycle swings between 0.95-0.468. Therefore, the value of capacitor should be designed for the worst possible C. With $D=0.95$, the value of C is found to be $25 \mu \text{ F}$. It can be seen that if the value of C is not carefully designed for PSC, it might result in a lot of ripples in the DC bus voltage.

3.2.3 Effect of L on boost converter performance

The value of inductance (L) plays an important role in deciding the performance of converter. The value of L is chosen such that $L > L_{\min}$, to operate the converter in CCM, otherwise the system operates in DCM. L_{\min} is the minimum inductance required to maintain the inductor current continuous. For a boost converter (Mohan and Undeland, 2007),

$$L_{\min} = \frac{(1-D)^2 DR}{2f_s} = \frac{V_{\text{dc}}V_{\text{pv}}D(1-D)}{2P_{\text{pv}}f_s} = \frac{V_{\text{dc}}^2D(1-D)^2}{2f_sP_{\text{MPP}}} \quad (3.6)$$

For a constant V_{dc} and switching frequency (f_s), $L_{\min}=fn(P_{\text{MPP}}, D)$. From (3.6), it is evident that the worst possible L_{\min} is designed for minimum possible P_{MPP} and maximum $D(1-D)^2$. For a IM pump system, the power drawn by the motor (P_m) is a cubic function of stator frequency (f) (Muljadi, 1997b). For a motor pump system to operate (to successfully pump the water for the given head) the minimum stator

frequency f_{\min} should be 20 Hz. If $P_{m_{\min}}$ and $P_{m_{\text{rated}}}$ are the minimum and rated power the motor draws to operate pump at f_{\min} and f_{rated} respectively, then the value of $P_{m_{\min}}$ is given by

$$P_{m_{\min}} = \left(\frac{f_{\min}}{f_{\text{rated}}} \right)^3 P_{m_{\text{rated}}} = 53W \quad (3.7)$$

From (3.7), it is seen that the motor should draw a minimum of 53 W from the inverter for the pump to operate successfully. If the inverter is assumed to be 100 % efficient, the boost converter should supply a minimum of 53 W at the DC bus. Assuming the worst possible boost converter efficiency to be 80%, the value of P_{MPP} should be at least 70 W. This means the worst possible P_{MPP} should be at least 70 W. With this P_{MPP} , we plot the variation of L_{\min} vs D. The variation of L_{\min} with D for $P_{\text{MPP}} = 70$ W is shown in Fig 3.4. From Fig 3.4 one can see that the maximum value of $L_{\min} = 4.83$ mH occurs at $D = 0.33$. If any value of $L < L_{\min}$, the converter operates in DCM. In case of uniform shading conditions, the value of L_{\min} is 4.37 mH. Any value of $L < L_{\min}$, the converter operates in DCM. However, in case of PSC, since the MPP can lie anywhere in the voltage range, it is ideal to fix $L_{\min} = 4.83$ mH. It is seen from the above analysis that, if PSC is not taken into account, and the converter is designed for uniform shading conditions, the converter might enter into DCM.

To demonstrate the detrimental effect the DCM might have on the system performance, an example is demonstrated in Fig 3.1. Since the converter always operates at MPP, the values of V_{pv} , P_{pv} for the design are all chosen at MPP. Suppose the value of L is designed keeping into consideration the shading patterns I-VI (Fig 3.1b), the maximum value of L_{\min} would be 0.903 mH (designed for $0.8V_{\text{oc}}$, which is the maximum possible voltage and the minimum peak power value of 376 W). This ensures the converter operates in CCM.

However, if the panels are subjected to shading pattern VIII, the MPP algorithm detects the global peak at V_{pv} of 47.9 V and the peak power is 228 W. Since the peak power location is shifted to the left, this requires a duty cycle as large as 0.88 which may cause a large stress on the switch which is not advisable. The duty cycle requirement may worsen if the DC link requirement increases. For star connected IM, the minimum DC link requirement should be at least 560 V, the duty cycle required to maintain this voltage is 0.92. From pattern VIII it is clear that, when the converter is operated at, $V_{\text{pv}} = 0.8V_{\text{oc}}$, the power is almost similar to MPP region. The duty cycle required at this point is 0.4285 and the power detected is approximately 210 W,

which is a little lesser than MPP. However, the minimum inductor required would be 1.67 mH. Since the designed value of L_{\min} is 0.9 mH, the converter now enters into DCM. When the panels are subjected to shading pattern IX, the similar phenomena as of VIII is observed. However, the value of L_{\min} required is now 3.48 mH. The shading pattern VIII and IX clearly demonstrate the effect of location of peak on converter performance.

3.3 Steady state Modeling of power converter and Induction motor pump

In section 3.2, the possible effects of the partial shading on the performance of DC–DC converter is presented. In this section, the equations that describe the DC–DC converter, inverter and induction motor pump system will be derived. This equations are further solved using numerical techniques to understand the phenomena discussed in section 3.2.

3.3.1 Duty cycle calculation

Once the maximum power point is known, we now estimate the duty ratio requirement to the fix the panel voltage and current at MPP. In section 3.2, we have already discussed the fair chances of converter entering into discontinues mode. Therefore, we formulate equations for both CCM and DCM. It is a known fact that source power (power from the PV panels) must be sum of output power (power fed to inverter) and losses. The losses are the functions of parasites which are given by equations (3.8) and (3.9) respectively. P_{pv} is the power available at the panels and P_{inv} is the power at the output of the converter (power input to the inverter) and P_{loss} is the power loss in the converter due to parasites.

$$P_{\text{pv}} = P_{\text{inv}} + P_{\text{loss}} \quad (3.8)$$

$$P_{\text{loss}} = fn(r_l, r_c, c_{\text{sw}}, v_d, r_{\text{sw}}, D) \quad (3.9)$$

3.3.1.1 CCM

The P_{loss} in case of CCM is given by (3.10).

$$p_{\text{loss}} = I_L^2 r_l + DI_L^2 r_{\text{sw}} + 0.5C_{\text{sw}} V_{\text{dc}}^2 f_s + I_c^2 r_c + (1 - D)v_d I_L \quad (3.10)$$

Here, I_L is the average inductor current. Substituting (3.10) in (3.8) and equating $I_L = I_{pv}$ (this is true because, $I_{pv} = I_{cin} + I_L$ and $I_{cin} = 0$, where I_{cin} is the average current through the input capacitor)

we get,

$$V_{pv}I_{pv} = V_{dc}I_{inv} + I_{pv}^2 r_1 + DI_{pv}^2 r_{sw} + 0.5C_{sw}V_{dc}^2 f_s + I_c^2 r_c + (1-D)v_d I_{pv} \quad (3.11)$$

where, I_{inv} is the inverter input current. Simplifying (3.11) will yield the steady state voltage (3.12). The steady state duty cycle required to transfer the maximum power to DC bus is obtained by solving (3.12) for $D = D_{MPP}$, $V_{pv} = V_{MPP}$ and $I_{pv} = I_{MPP}$ with $V_{dc} = V_{dc,ref}$. The parasites considered for modeling are esr of inductor (r_1), esr of capacitor (r_c), switch resistance (r_{sw}), voltage drop across the diode (v_d), charging capacitance of switch and diode (c_{sw}). Here $D' = (1 - D)$.

$$V_{dc} = \frac{[V_{pv} - v_d(1 - D)](1 - D)R}{Dr_{sw} + r_1 + r_c DD' + D'^2 R \left(\frac{1}{2}c_{sw}f_s R + 1\right)} \quad (3.12)$$

where,

$$R = \frac{V_{dc}}{I_{pv}(1 - D)}$$

R is the equivalent load resistance as seen by the boost converter output terminals,

3.3.1.2 DCM

The steady state duty cycle required to transfer the maximum power to DC bus is obtained by solving (3.13) and (3.14) for $D = D_{MPP}$, $V_{pv} = V_{MPP}$ and $I_{pv} = I_{MPP}$ with $V_{dc} = V_{dc,ref}$.

$$V_{dc} = \frac{[(D + D_1)V_{pv}D_1 - v_d D_1^2]R}{x} \quad (3.13)$$

$$x = (D + D_1)^2 r_1 + D(D + D_1)r_{sw} + \frac{0.5c_{sw}f_s R^2 D_1^2}{D + D_1} + \left(\frac{D_1(1 - D_1) + D^2}{D + D_1}\right) D_1 r_c + \frac{RD_1^2}{D + D_1}$$

and

$$R = \frac{V_{dc}(D + D_1)}{I_{pv}D_1}$$

$$D_1 = \frac{V_{dc} 2(Lf_s + (r_1 + r_{sw})D)}{V_{pv}RD} \quad (3.14)$$

Whenever there is a change in insolation/temperatures, the new MPP is mathematically calculated using analytical MPPT derived in chapter 2. The V_{MPP} and I_{MPP} from MPP calculation is further used to determine the duty ratios, (3.12) in case of CCM and (3.13) and (3.14) in case of DCM. In both the cases, $V_{dc} = V_{dc,ref}$, this is done in order to operate the converter at constant DC link voltage.

3.3.2 Induction motor and Pump

The equations derived in subsection 3.3.1, ((3.12) for CCM and (3.13) and (3.14) for DCM), gives the duty cycle (D_{MPP}) that not only transfers maximum power from PV to DC bus, but also maintains a constant DC-link voltage. However, for this to happen, the value of R (load as seen by the converter output terminals) should be able to sink the MPP power. Since $R = \frac{V_{dc}}{I_{inv}}$, for a constant V_{dc} , it is I_{inv} that varies to meet the maximum power transfer condition and constant v_{dc} requirement. The inverter should draw this I_{inv} to drive the motor pump system. For an IM pump system, the power consumed by the motor pump (P_m) is given by $P_m = k\omega_r^3$. where ω_r is the rotor speed. Therefore, the power consumed by the motor pump is controlled by varying rotor speed. Since rotor speed is a function of stator speed(ω_s), we control the stator speed (stator frequency) to control the power consumed by the motor.

To summarize, the entire power available at the DC bus is pumped into motor pump system by calculating the suitable stator frequency. The boost converter equations will set the required duty cycle to transfer the power from PV terminals to DC bus. The current that the inverter should draw to maintain the DC link constant in case of CCM and DCM are given by (3.15) and (3.16) respectively.

CCM

$$R = \frac{V_{dc}}{I_{inv}} = \frac{V_{dc}}{I_{pv}(1 - D)} \quad (3.15)$$

DCM

$$R = \frac{V_{dc}}{I_{inv}} = \frac{V_{dc}(D + D_1)}{I_{pv}D_1} \quad (3.16)$$

The objective here is to derive equations that relate V_{dc} , I_{inv} with the stator frequency(f).

Assuming the inverter to be lossless, the power fed to the inverter($V_{dc}I_{inv}$) is equal to the power fed to the motor pump system.

$$V_{dc}I_{inv} = 3V_{ph}I_{ph}\cos(\phi) \quad (3.17)$$

$$\implies I_m = \frac{V_{dc}I_{inv}}{3V_{ph}\cos(\phi)} \quad (3.18)$$

where, V_{ph} and I_m are the phase voltage and current of induction motor. ϕ is the phase angle between V_{ph} and I_m .

To avoid the flux saturation and utilize the maximum torque handling capability, we fix e/f ratio to be constant. If e_{rated} and f_{rated} are the emf and frequency at rated conditions respectively and e and f are the emf at any other conditions.

$$\frac{e}{f} = \frac{e_{rated}}{f_{rated}} = k_1 \quad (3.19)$$

Expressing V_{ph} in terms of k_1 and f ,

$$V_{ph} = k_1f + I_m z_1 \quad (3.20)$$

where, z_1 is the stator impedance of the induction motor. Substituting (3.20) in (3.18), we get

$$I_m - \frac{V_{dc}I_{inv}}{3(kf + I_m z_1)\cos\phi} = 0 \quad (3.21)$$

where,

$$\phi = \tan^{-1} \left(\frac{(x_1 + x_m)(r_2^2/s^2 + x_1^2 + 2x_1x_m)}{r_2x_m^2/s + r_1(r_2^2/s^2 + (x_2 + x_m)^2)} \right)$$

Equation (3.21) has three unknowns, I_m , f and s . Therefore, two more equations should be derived to make the system of equations solvable.

We know that, for a pump load,

$$P_{\text{sh}} = k\omega_r^3 \quad (3.22)$$

where, $k = \frac{P_{\text{sh, rated}}}{\omega_{r, \text{rated}}^3}$ is called the pump constant.

$$P_{\text{sh}} = P_g(1 - s) = (V_{\text{dc}}I_{\text{inv}} - 3I_{\text{m}}^2r_1)(1 - s) \quad (3.23)$$

$$I_{\text{m}} = \frac{V_{\text{ph}}}{z} = \frac{(k_1f + I_{\text{m}}z_1)}{z} \quad (3.24)$$

Substituting (3.23) and (3.24) in (3.22), we get

$$V_{\text{dc}}I_{\text{inv}} - 3\frac{((k_1f + I_{\text{m}}z_1)^2r_1)}{z^2} - k(2\pi f)^3(1 - s)^2 = 0 \quad (3.25)$$

Here, P_{sh} is the power available at the shaft, k is the pump constant, ω_r is the rotor speed, P_g is the power available at the air-gap, s is the slip and z is the total impedance of the IM. Equations (3.21), (3.24) and (3.25) are now solved for given V_{dc} and I_{inv} to obtain f and ω_r .

The initial condition for the stator frequency calculation is given by (3.26) (derived from pump characteristics)(Pottebaum, 1984).

$$f^*\alpha P_{\text{MPP}}^3 = \sqrt[3]{\frac{P_{\text{MPP}}}{P_{\text{MPP, ref}}}} f_{\text{ref}} \quad (3.26)$$

where f is the stator frequency in Hz and P_{MPP} is the power at DC bus at any insolation, $P_{\text{mpp, ref}}$ is the power at the dc bus at standard test conditions, and f_{ref} is the base frequency of the motor.

3.3.3 Solution of Non linear Equations

Since the system involves PV panels, power electronic converters and machines which are by nature non-linear. The equations that are formulated are also non-linear. Therefore, arriving at solutions is tedious and challenging.

Newton's method is the most widely used method to solve the system of non-linear equations. However, following are its limitations.

1. The Hessian matrix $H(x_k)$ in $H(x_k)d_k = -F(x_k)$ if singular, the newton step

(d_k) is not defined.

2. It is also possible that the newton method may not converge to the solution if the chosen initial condition is far away from the solution
3. The Hessian matrix should be positive definite

Since the resulting equations from water pumping system are complex, understanding the definiteness of the Hessian matrix is difficult. Predicting the nearby initial conditions is also tedious especially when the system is subjected to partial shading conditions, where the operating voltage and current are a function of global peak location (Refer Fig 3.1(b) where the voltage corresponding to global peak may occur anywhere in between 0 to $0.7XNXV_{OC}$) and the frequency of the motor pump system that maintains the V_{dc} constant may lie anywhere between 20 Hz to 50 Hz. It is therefore clear that, the Newton based method is not suitable for solving such system of non linear equations. Therefore, trust region based methods which overcomes the limitations of Newton based method is employed.

3.4 Dynamic modeling of Power converter and Induction Motor

In the previous section, the steady state model of the boost converter, induction motor and the pump system is presented. In this section, the dynamic equations of the same shall be presented. The differential equations of this section are solved using simulink blocks of MATLAB to yield dynamic plots.

3.4.1 Dynamic model of boost converter

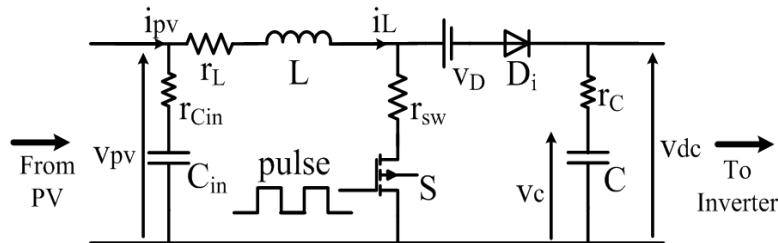


Figure 3.5: Circuit diagram of a boost converter

The circuit diagram of a non ideal boost converter is shown in Fig 3.5. Applying KCL at the node containing capacitors and KVL for the loop containing inductors, during switch ON and OFF state we get,

ON State

$$\frac{dv_{c_{in}}}{dt} = \frac{1}{C_{in}} (i_{pv} - i_L) \quad (3.27)$$

$$\frac{di_L}{dt} = \frac{1}{L} (v_{pv} - i_L (r_L + r_{sw})) \quad (3.28)$$

$$\frac{dv_c}{dt} = -\frac{1}{C} i_{inv} \quad (3.29)$$

OFF state

$$\frac{dv_{c_{in}}}{dt} = \frac{1}{C_{in}} (i_{pv} - i_L) \quad (3.30)$$

$$\frac{di_L}{dt} = \frac{1}{L} (v_{pv} - i_L (r_L) - v_d - v_{dc}) \quad (3.31)$$

$$\frac{dv_c}{dt} = \frac{1}{C} (i_L - i_{inv}) \quad (3.32)$$

If s is the switching state of the converter with value 1 when switch being ON and 0 when switch OFF, the above equations can be written as

$$\frac{dv_{c_{in}}}{dt} = \frac{1}{C_{in}} (i_{pv} - i_L) \quad (3.33)$$

$$\frac{di_L}{dt} = \frac{1}{L} (v_{pv} - i_L (r_L + sr_{sw}) - (1 - s) (v_d - v_{dc})) \quad (3.34)$$

$$\frac{dv_c}{dt} = \frac{1}{C} ((1 - s) i_L - i_{inv}) \quad (3.35)$$

and the equations for v_{pv} , v_{dc} and i_{inv} are given by

$$v_{pv} = (i_{pv} - i_L) r_{c_{in}} + v_{c_{in}} \quad (3.36)$$

$$v_{dc} = (i_L - i_{inv}) r_c + v_c \quad (3.37)$$

$$i_{inv} = s_a i_a + s_b i_b + s_c i_c \quad (3.38)$$

where, s_a , s_b and s_c are the switching functions of the inverter for a, b and c phase respectively and i_a , i_b and i_c are the line currents of the induction motor.

3.4.2 Dynamic model of inverter

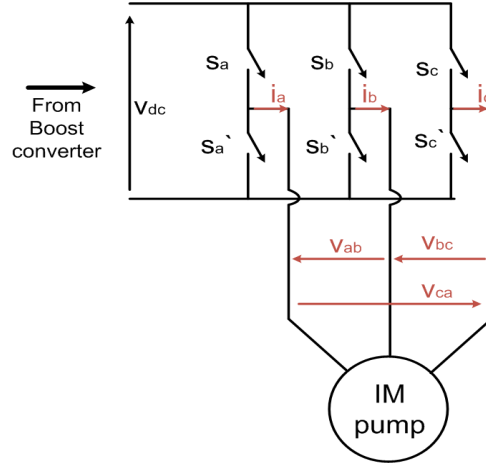


Figure 3.6: Circuit diagram of a inverter feeding motor

The circuit diagram of a inverter feeding an induction motor pump is given by 3.6. If $s_a^|$, $s_b^|$ and $s_c^|$ are the complimentary switching states of s_a , s_b and s_c , then the inverter L-L voltages are given by

$$V_{ab} = (s_a s_b^| - s_a^| s_b) = (s_a (1 - s_b) - (1 - s_a) s_b) \quad (3.39)$$

$$V_{bc} = (s_b s_c^| - s_b^| s_c) = (s_b (1 - s_c) - (1 - s_b) s_c) \quad (3.40)$$

$$V_{ca} = (s_c s_a^| - s_c^| s_a) = (s_c (1 - s_a) - (1 - s_c) s_a) \quad (3.41)$$

$$(3.42)$$

Using three to two axis transformation we get,

$$v_{ds} = v_{ab} \quad (3.43)$$

$$v_{qs} = \frac{1}{\sqrt{3}} (v_{bc} - v_{ca}) \quad (3.44)$$

where, v_{ab} , v_{bc} and v_{ca} are the L-L output voltage of the inverter and v_{ds} and v_{qs} are the direct and quadrature axis voltages of the inverter.

3.4.3 Dynamic model of Induction motor and pump

The dynamic model of the induction motor is presented in d-q frame given by (3.45)–(3.48)(Bose, 2010). Here, ψ_{dr} and ψ_{ds} are the direct axis rotor and stator flux, and ψ_{qr} and ψ_{qs} are the quadrature axis rotor and stator flux. i_{dr} and i_{ds} are the direct axis rotor and stator currents, and i_{qr} and i_{qs} are the quadrature axis rotor and stator currents.

$$\begin{bmatrix} \dot{\psi}_{ds} \\ \dot{\psi}_{qs} \\ \dot{\psi}_{dr} \\ \dot{\psi}_{qr} \end{bmatrix} = - \begin{bmatrix} r_s & \omega L_s & 0 & \omega L_m \\ \omega L_s & r_s & \omega L_m & 0 \\ 0 & -\omega_s L_m & r_r & -\omega_s L_r \\ \omega_s L_m & 0 & \omega_s L_r & r_r \end{bmatrix} \begin{bmatrix} i_{ds} \\ i_{qs} \\ i_{dr} \\ i_{qr} \end{bmatrix} + \begin{bmatrix} v_{ds} \\ v_{qs} \\ v_{dr} \\ v_{qr} \end{bmatrix} \quad (3.45)$$

$$\begin{bmatrix} \psi_{ds} \\ \psi_{qs} \\ \psi_{dr} \\ \psi_{qr} \end{bmatrix} = \begin{bmatrix} L_s & 0 & L_m & 0 \\ 0 & L_s & 0 & L_m \\ L_m & 0 & L_r & 0 \\ 0 & L_m & 0 & L_r \end{bmatrix} \begin{bmatrix} i_{ds} \\ i_{qs} \\ i_{dr} \\ i_{qr} \end{bmatrix} \quad (3.46)$$

$$t_e = \frac{3P}{2} \frac{1}{2} (\psi_{ds} i_{qs} - \psi_{qs} i_{ds}) \quad (3.47)$$

$$\frac{d\omega_r}{dt} = \frac{P}{2J} (t_e - k\omega_r^2) \quad (3.48)$$

v_{dr} and v_{ds} are the direct axis rotor and stator voltages, and v_{qr} and v_{qs} are the quadrature axis rotor and stator voltages. t_e is the electromagnetic torque developed by the motor

3.5 Results and Discussion

In the previous sections, the effect of partial shading on the boost converter performance is discussed followed by steady state modeling of the system, In this section, the results that serve as proof for validating the studied theory is presented. In the first half of the section, the dynamic response of the water pump for partial shading

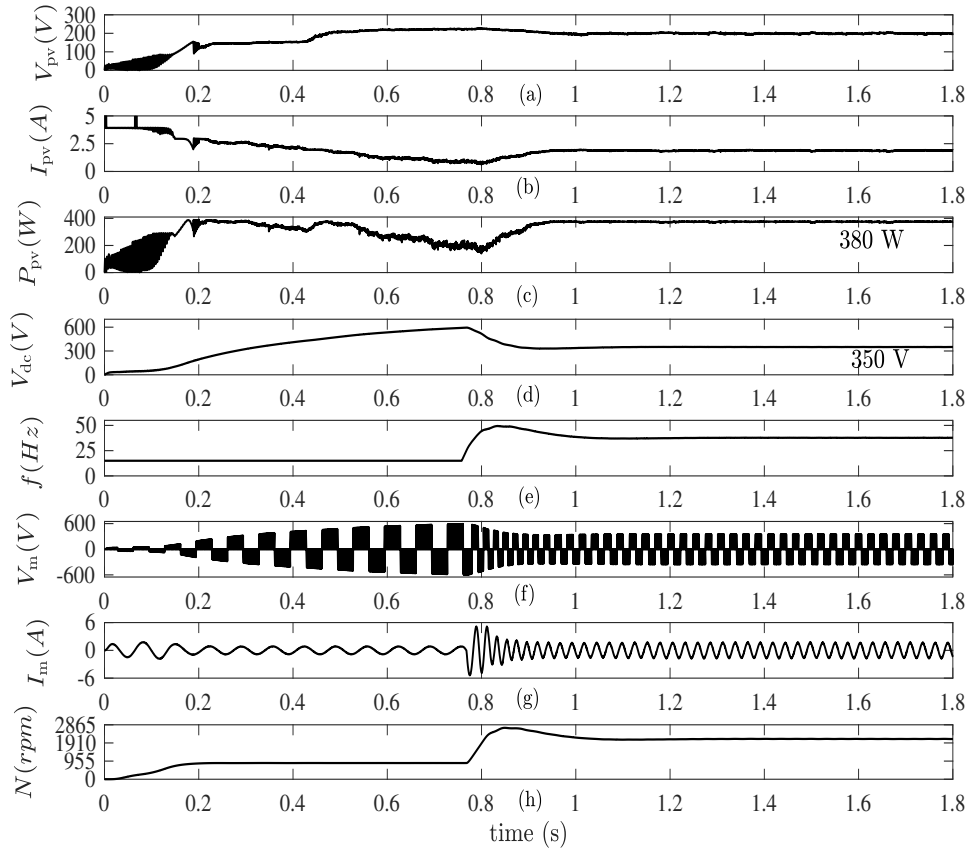


Figure 3.7: Simulated curves of PV fed induction motor water pump system showing voltage build up

conditions are presented by simulating the model in simulink of MATLAB. The results from the simulations are validated by experimentations. Since, it is very difficult to show the dynamic response for all the shading conditions, the results for few shading conditions are presented. To show the system response for all the shading conditions, in the later half of this section, the steady state response of the system for all the shading patterns are presented, further validated by experimentation. It can be seen that, the results from steady state model, dynamic model and experimentations are in good agreement with each other.

The shading patterns form the initial input to the system. The simulation and experimental results are plotted for the shading patterns shown in Fig. 3.1(b). The simulation results for PV fed induction motor pumping systems showing the voltage build up process is presented in Fig. 3.7. The results are presented for shading pattern

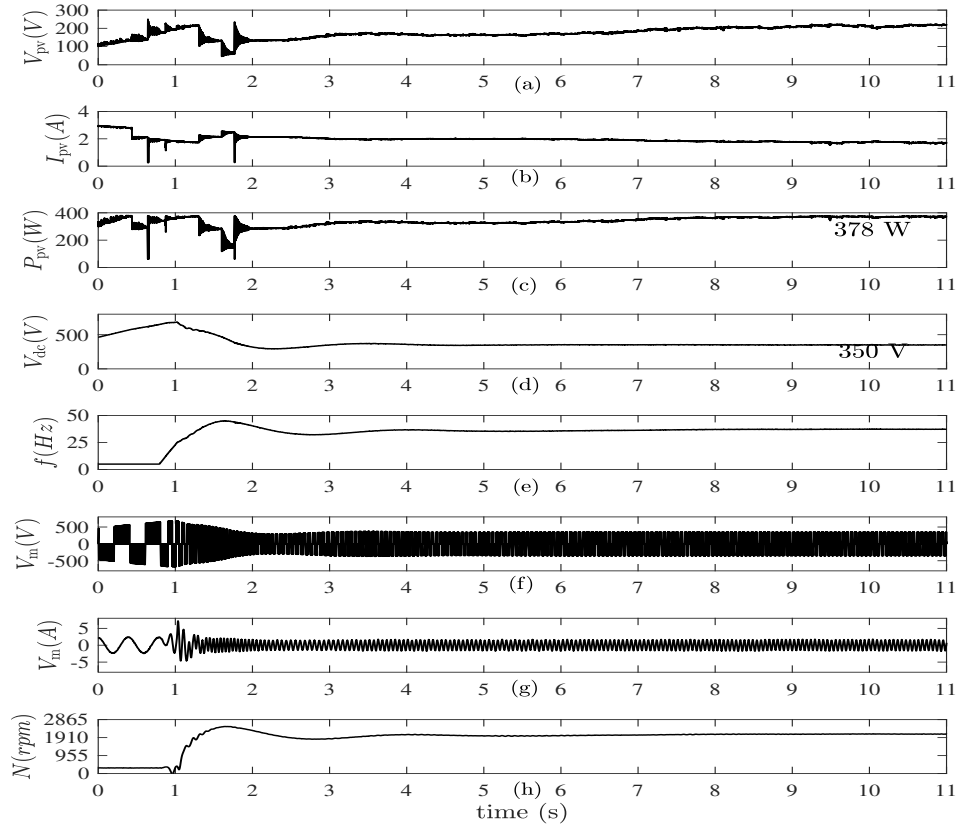


Figure 3.8: Experimental curves of PV fed induction motor water pump system showing voltage build up

I of Table 3.2 with $V_{dc_{ref}} = 350$ V. The MPP algorithm takes approximately 1 s to track a power of 380 W and is shown in Fig 3.7c. The corresponding V_{pv} and I_{pv} are shown in Fig 3.7a and Fig 3.7b respectively. The DC bus voltage build up process is shown in Fig. 3.7d and it takes approximately 1s to reach the steady state set point of 350 V. The stator frequency required to maintain 350 V at DC bus is shown in Fig. 3.7e. The corresponding stator voltage (V_m), current (I_m) and the rotor speed (N) are presented in Fig. 3.7f,g and h respectively. To validate the results from the simulation, the experimental results are presented in Fig. 3.8. The experimental peak power is 378 W which is just 2 W less than the simulated peak power and takes 9 s to reach MPP. The DC bus build up is shown in Fig. 3.8d. The stator frequency required to maintain DC link voltage at the setpoint is shown in Fig. 3.8e. The corresponding stator voltage, current and the rotor speed are presented in Fig. 3.8f,g

and h respectively.

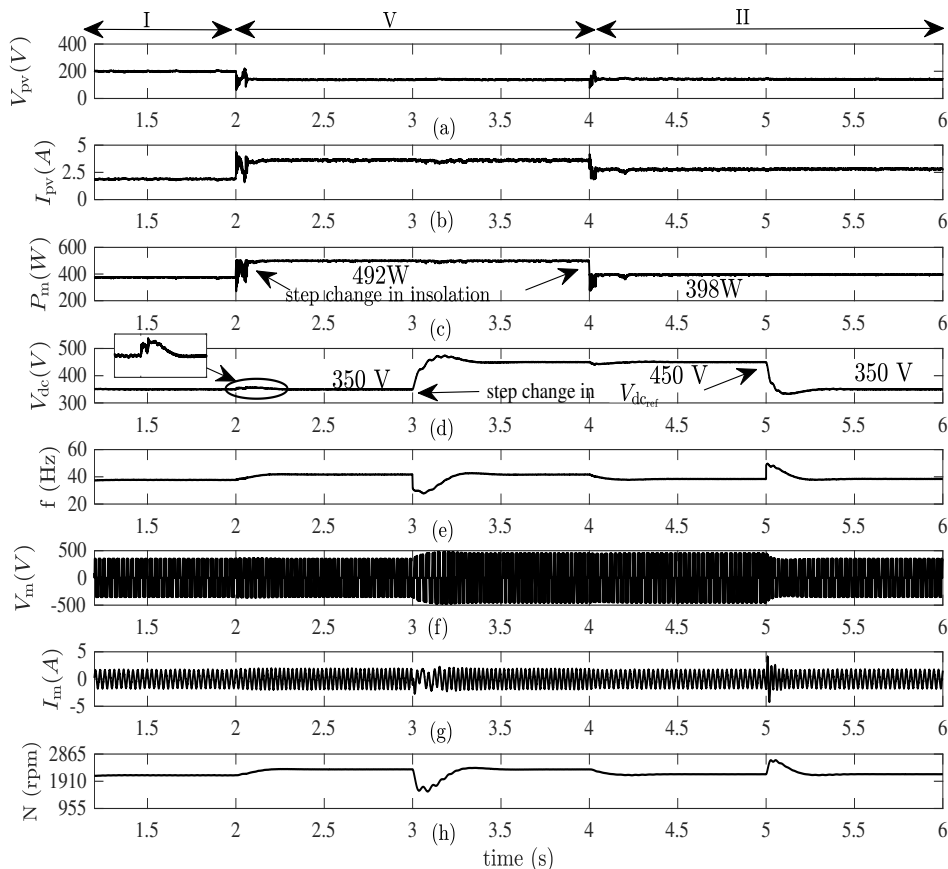


Figure 3.9: Simulated curves for step change in insolation and V_{dc}

The system is further tested for change in insolation and DC link voltage reference and the simulation results are presented in Fig. 3.9. At $t=2s$, the shading was changed from pattern I to V. The MPP algorithm identifies the new global peak and tracks in a time less than 0.5s and the tracked peak is 492 W. Since the input power has now increased, momentarily there is power imbalance at the DC bus. Therefore, the DC bus voltage momentarily swells. To get back the DC bus voltage to the set point value, the stator frequency now increases. The waveform of the DC bus voltage and the stator frequency are shown in Fig. 3.9d and 3.9e respectively. Since the power consumption has increased, the speed also increases and is given by Fig. 3.9h. The corresponding motor voltage and currents are given in Fig. 3.9f and Fig. 3.9g respectively. At $t=3s$, $V_{dc,ref}$ is changed from 350 to 450 V. The controller tracks the new reference value in less than 0.5s. The PV power is undisturbed since the insolation

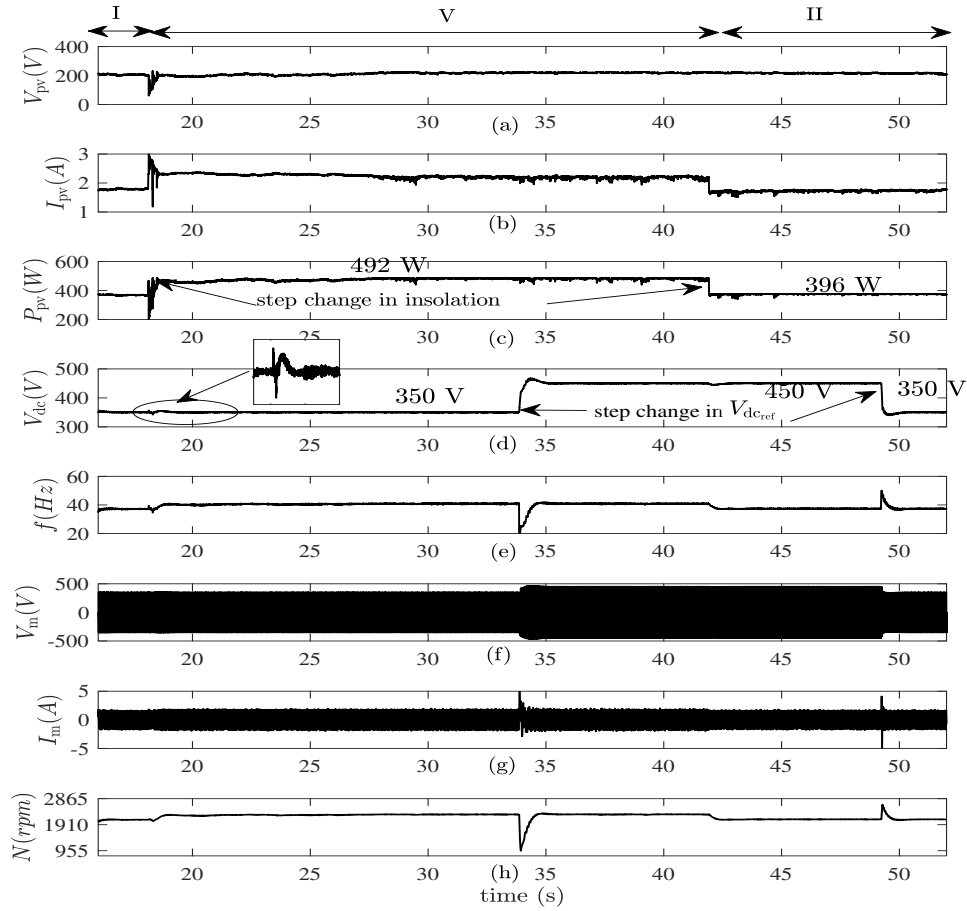


Figure 3.10: Experimental curves for step change in insolation and V_{dc}

remains constant. Since the stator frequency is also a function of input power, the stator frequency dips momentarily, however its restored back to its previous value. At $t=4$ s, the shading pattern is changed from V to II. The MPP algorithm tracks the change in shading pattern and tracks the new MPP. Since the power input is decreased, there is momentary mismatch in power levels at the DC bus and the extra power to the load is momentarily supplied by the DC bus, therefore the DC bus voltage dips. To restore the power balance, the stator frequency decreases thus maintaining the value of DC bus voltage at the reference value. Since the power fed to motor has decreased, the rotor speed also decreases. At $t=5$ s, again the DC bus voltage is decreased from 450 V to 350 V, it can be seen that the controller tracks the reference voltage command and the input power is not disturbed. The stator frequency momentarily swells, however it is soon restored to original value. The

experimentation is carried out with the similar sequence of insolation and V_{dc_ref} and are presented in Fig. 3.10. The simulation and experimental results are found to be in good agreement with each other.

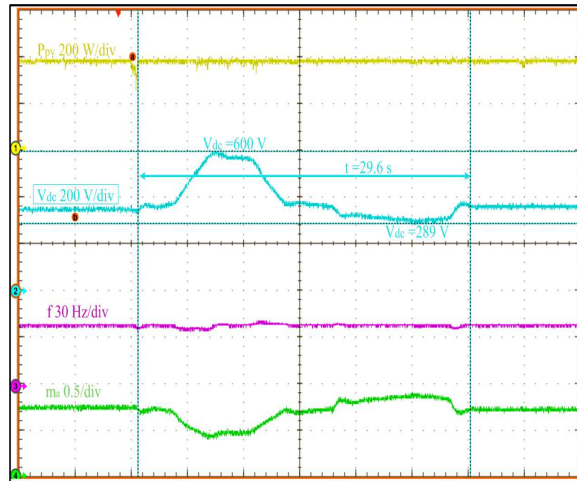


Figure 3.11: Experimental curves of PV fed induction motor water pump system showing continuously varying V_{dc_ref}

To further demonstrate the relationship between DC bus voltage, the input power and stator frequency, the experiment is performed with variable DC link voltage reference and the results are presented in Fig. 3.11. The experimentation results are presented for shading pattern I. From (3.1), with $m_{a_max} = 1$, $\implies V_{dc_min} = 1.42V_{m_rms}$. For shading pattern I, from Fig 3.8, MPP power detected is 378 W and the corresponding stator frequency is 37 Hz. Since the control involves v/f strategy, V_{m_rms} is 170.2 V. Therefore, the value of V_{dc_min} is approximately 250 V. Therefore, in the experiment, V_{dc_ref} is continuously and non-uniformly changed from 289 V to 600 V in a span of 29.6s. In Fig 3.11, channel 1 is the input power (P_{pv}), channel 2 is the DC link voltage (V_{dc}), channel 3 is the stator frequency (f) and channel 4 is the modulation index (m_a). The results are presented for shading pattern I and the DC bus voltage was maintained at 350 V. At $t=1.76$ s, the V_{dc_ref} is varied at a non uniform rate from the value of 350 V to 600 V. The MPP algorithm maintains the input power constant. Since the input power is constant and the controller tracks the DC link voltage, the stator frequency also remains constant. For a varying DC bus voltage, since v/f ratio has to be maintained constant, the modulation index varies accordingly. To maintain constant V_{m_rms} , the modulation index and the DC bus voltage are inversly proportional to each other, the value of m_a decreases for

the increasing DC bus voltage. Once the DC bus reaches 600 V, the $V_{dc,ref}$ is again decreased till 289 V. The input power and the stator frequency is found to remain constant and the value of m_a increases to meet the constant v/f requirement.

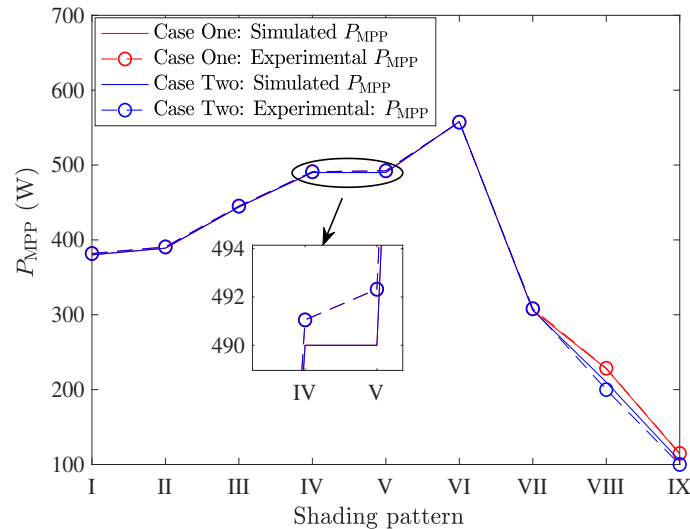


Figure 3.12: Simulated and Experimental values of MPP

Having seen that the results from simulink agree very well with the experimental results, and since its difficult to present dynamics for all shading patterns, In the following discussions, the effect of partial shading on the system is studied through steady state performance. This is done by solving the equations derived in section 3.3 using numerical techniques available in MATLAB. To study this, the results are presented in two cases named as case one and case two. Case one indicates that, for all the shading patterns, the MPP algorithm always operates at true MPP condition. In case of two, the algorithm fixes the operating point based on the duty cycle constraints. It means, that the algorithm first detects the true MPP and also checks the duty ratio. If the duty ratio is greater than the critical value, it searches the next peak and fixes the operating point. It is already discussed in previous sections that the boost converter operating point is one of the crucial conditions that determine the performance of the system. For the shading pattern considered in Fig 3.1(b), the steady state operating power of the boost converter is presented in Fig. 3.12. It is seen that till shading pattern I – VII, the trajectories of case one and case two are same. However, for shading pattern VIII and IX, as per the discussion in section 3.2, the trajectories change. The change in operating point for case one and two for

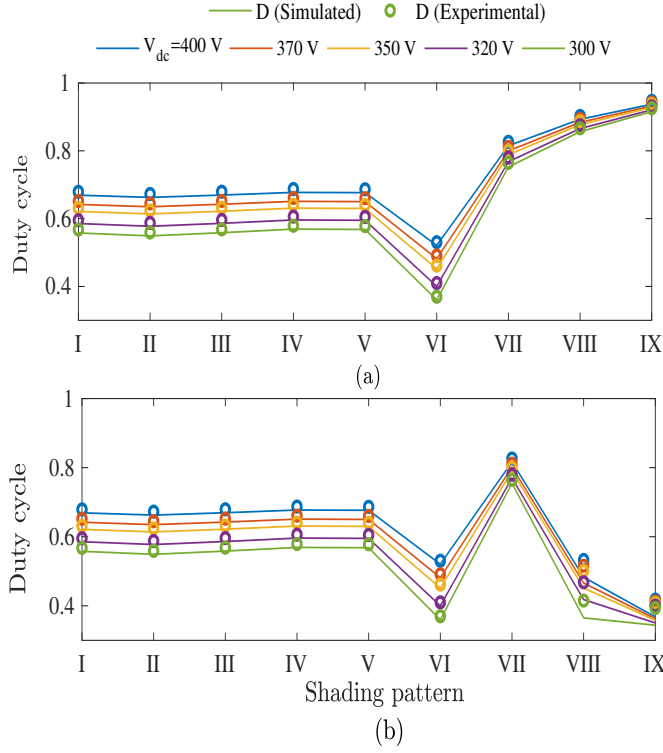


Figure 3.13: Simulated and Experimental Duty cycle a) case one b) case two

shading pattern VIII and IX are due to the duty ratio constraint and variation of the duty cycle for all the considered shading patterns are presented in Fig. 3.13.

The simulations are carried out by varying the V_{dc} from 300 V to 400 V. For a shading pattern VIII and IX, the converter has to operate at a duty ratio of 0.88 to 0.94 which causes a high stress on the switch and might eventually damage the switch (Fig 3.13a). To avoid this, the PV operating point is now shifted to the second maximum peak which lies around $0.8 \times N \times V_{oc}$ line. This will reduce the stress on the switch to less than 0.6. However, the converter now enters into DCM (Fig 3.13b). The input power (P_{pv}) and output power (P_{inv}) of the boost converter is shown in Fig 3.14 and their corresponding efficiency is shown in Fig 3.15. For shading pattern I to VII, the converter efficiency is found to be greater than 90%. For shading pattern VIII and IX, the converter can now enter into either CCM or DCM. If the converter operates in case one, the simulated efficiency for VIII and IX is found to be 90% and 85% respectively and in case two, it falls to a very low value of 80% and 45% respectively. Thus it is seen that for a given shading pattern, the converter operate

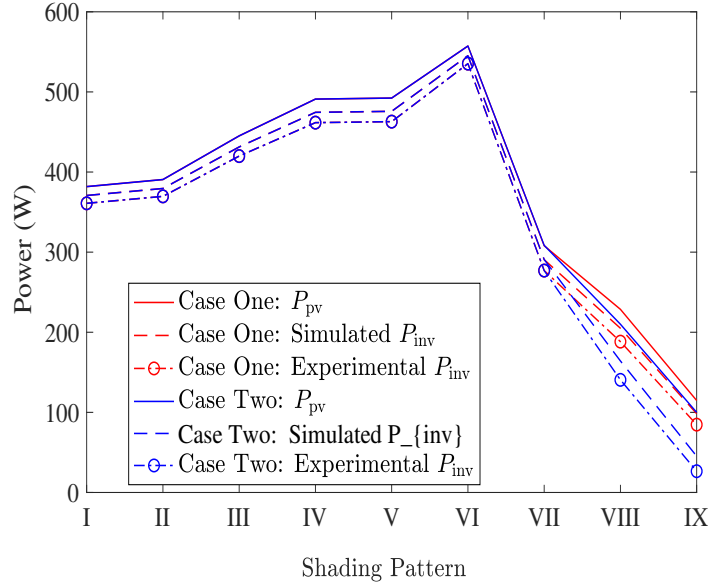


Figure 3.14: Input and output power of the boost converter for $V_{dc}= 350$ V for case one and case two

with a better efficiency in CCM than DCM. However, the switch is subjected to a high stress. The experimental plots are also presented to validate the simulation results.

The simulated and the experimental values of rotor speed are presented in Fig 3.16 respectively. The impact of boost converters CCM and DCM operation on rotor speed is shown. At shading pattern IX, in DCM mode, the stator frequency is 14 Hz, which is lesser than the minimum frequency required for the pump to start, therefore, the rotor speed is zero. However, in CCM, the rotor speed is found to be 1500 RPM. Though the available input power is almost same in both the modes (114 W and 100 W in CCM and DCM respectively), the effect on the pump is so large that, the pump fails to start in case two.

The experimentation is carried out for selected shading patterns VI, VIII, and IX of Fig. 3.1(b) and the insolation details of all the nine shading patterns are provided in Table 3.2. The experimental curves showing PV array voltage (V_{pv}), PV array current (I_{pv}), power available at the PV array terminals (P_{pv}) and stator frequency (f) for the shading patterns VI, VIII and IX are presented in Fig 3.17. The detected MPP for shading pattern VI is 558 W and the corresponding stator frequency is around 40 Hz. The shading pattern VIII and IX were changed at 24.5 s, 34 s and the MPP detected

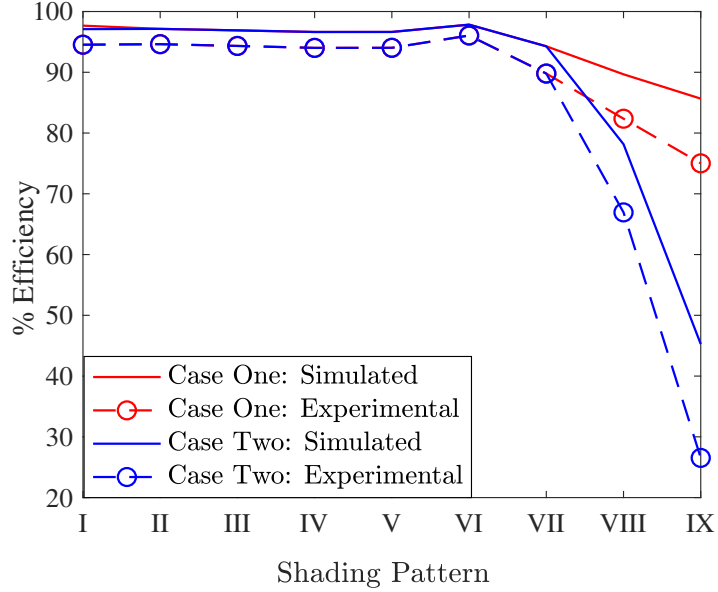


Figure 3.15: Simulation and Experimental efficiency of the boost converter for $V_{dc}= 350$ V for case one and case two

are 200 W, and 100 W respectively. Since the converter starts operating in DCM, the efficiency of the boost converter decreases as shown in Fig. 3.15. Therefore the power available at the inverter terminals decreases drastically (Refer Fig 3.14) and the corresponding frequencies are 24 Hz, and 15 Hz. The corresponding steady state switch voltages are shown in Fig 3.18 a and b respectively. For shading pattern IX, the frequency is 15 Hz which is less than 20 Hz, and therefore the pump fails to operate. The switch voltage in Fig 3.18 a and b shows the DCM operation of the converter. From the dynamic experimental plots, it is therefore clear that, the converter is found to transit from CCM to DCM for shading pattern VIII and IX and that the pump fails to operate for shading pattern IX though 100 W power is available at the PV terminal.

3.6 Conclusion

Unlike uniform shading conditions where peak power occurs at almost constant voltage regions, the peak power in case of partial shading occurs anywhere between constant current to constant voltage operation causes increased stress across DC-DC

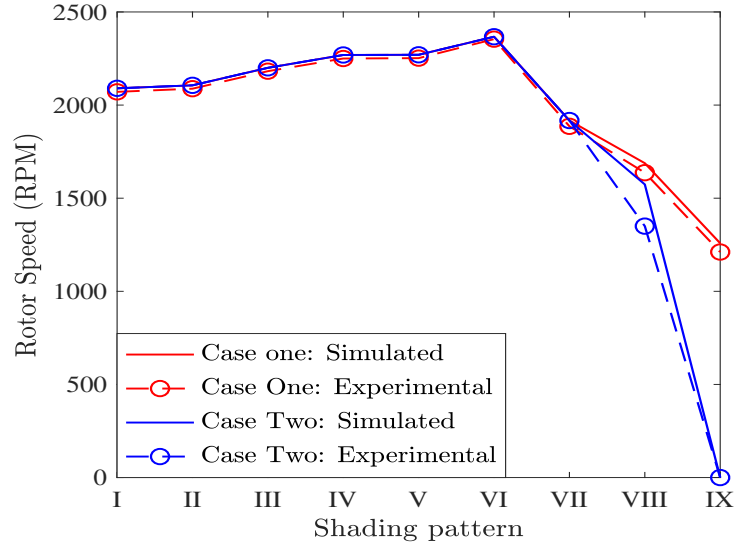


Figure 3.16: Simulated and Experimental Rotor speed of Induction Motor for case one and case two

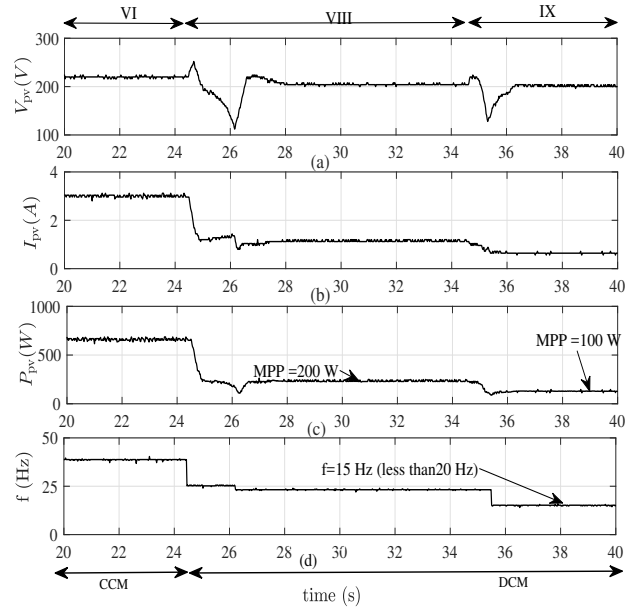


Figure 3.17: Experimental plots under CCM to DCM transition: a) PV panel Voltage (V_{pv}), b) PV current (I_{pv}), c) PV Power (P_{pv}), d) stator frequency (f)

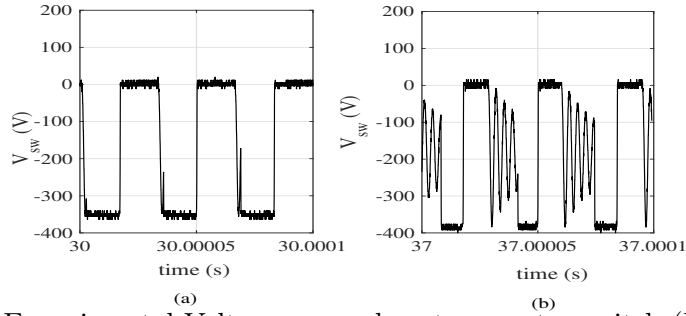


Figure 3.18: Experimental Voltage across boost converter switch (V_{sw}) for shading patterns: a) VIII and b) IX

converter switch and transition from continuous to discontinuous modes. The effects are so serious that the pump may even fail to operate though sufficient power is available at the PV terminals. The studied theory is validated by performing both dynamic and steady state simulations. The results from the simulations are further validated by conducting experimentations on actual experimental setup. It can be seen that the results from dynamic and steady state simulations are in total agreement with the results from experimentation. Overall, this work answers the effects caused by partial shading conditions on water pump systems.

Having studied the steady state and dynamic effects of shading on pumping systems, in the next chapter, the stability of the water pumping systems under partial shading conditions are presented through mathematical derivations verified by experimentation.

Chapter 4

Small signal Modeling

Contents

4.1 Introduction	73
4.1.1 Objectives	74
4.2 Small signal model of Boost converter	74
4.2.1 CCM	76
4.2.2 DCM	77
4.2.3 Inferences	79
4.2.4 Results and discussion	80
4.3 Small signal model of Motor pump system	83
4.4 Stability of water pumping system	84
4.5 Conclusion	86

4.1 Introduction

In the last chapter modeling of the power converter and inverter fed IM pump system is discussed. Through simulations and experimentations the detrimental impacts of shading are discussed. In this chapter small signal model of the power converter and the inverter fed motor is derived and several interesting observations are presented. In this chapter, the first section deals with the small signal of the boost converter

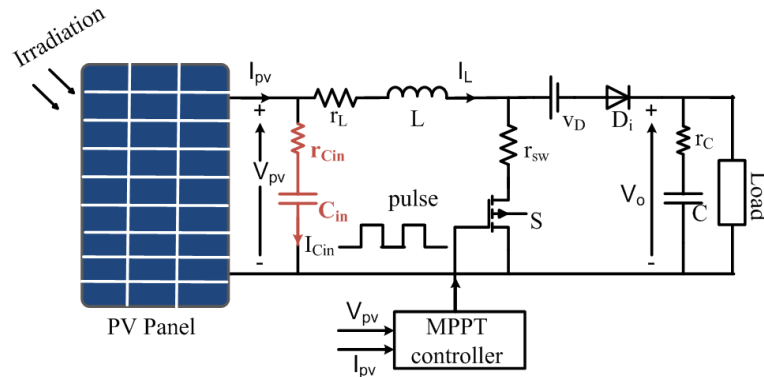


Figure 4.1: Circuit diagram of PV fed boost converter in MPPT mode feeding a load

which is an interface between the PV panel and the DC bus. The second half of the chapter presents the small signal model of Induction motor pump system.

4.1.1 Objectives

Given the discussed subject, the objectives of this chapter are

- It provides stability models for a non-ideal boost converter in both CCM and DCM modes and induction motor pumps through detailed derivations.
- It also shows exciting results like pole-zero cancellations in DC-DC converter in both the modes leading to a significant conclusion. It also provides the experimental proof to validate the presented concept.

4.2 Small signal model of Boost converter

Fig. 4.1 shows the circuit diagram of a PV fed non ideal boost converter feeding a load. The load could be a simple resistive load or a complex load like an inverter-fed motor. Here $V_{c_{in}}$, V_{pv} and V_c are the voltage across input capacitor, PV panels and output capacitors respectively. I_L and I_{pv} are the current through the inductor and PV terminals. C_{in} , L and C are the input capacitor, inductor and output capacitor of the boost converter respectively and V_o is the output voltage of the boost converter $V_o = V_{dc}$. In case of PV water pumping system, $r_{c_{in}}$, r_L , r_{sw} , r_c are the effective series resistances (esr) of input capacitor, inductor, switch and output capacitor respectively and v_D is the forward voltage drop of the diode (D_i).

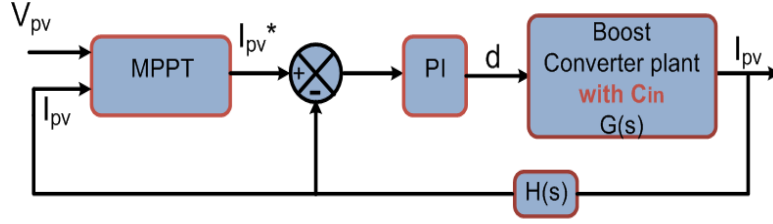


Figure 4.2: Functional Block diagram of PV fed boost converter with feedback loop

In most of the PV fed systems, it is mandatory to operate the system in MPPT mode. The MPPT controller takes V_{pv} and I_{pv} as inputs and generates duty cycle (d) such that maximum power is transferred from PV to load. The functional block diagram representation of PV fed boost converter with feedback loop is shown in Fig 4.2. Any MPPT algorithm generally takes V_{pv} and I_{pv} as inputs and generates a reference called $V_{pv_{ref}}$ or $I_{pv_{ref}}$. The value of V_{pv} or I_{pv} must be regulated at these reference values in order to transfer maximum power from source to the load. In order to accomplish this, the voltage/current reference generated by the MPPT controller is compared with its actual value and the error is further fed to a PI controller to generate pulses to the boost converter switches. In Fig. 4.2, $G(s)$ is the transfer function of the boost converter along with the input capacitor C_{in} , $H(s)$ is the transfer function of the feedback system containing the gains of the voltage and current sensors and PI is the controller. To design any controller such as P, PI, and PID, deriving the plant transfer function of the system is the first and the foremost step. The controller poles and zeroes are decided based on the characteristic of thus derived plant transfer function. In the present case, the boost converter forms the plant with d as the control input and i_{pv} as the controlled output. Since the boost converter can operate both in CCM and DCM, the objective here is to derive the transfer function, $\frac{i_{pv}(s)}{d(s)}$ for both the cases and show that the transfer function in both the cases is open loop stable.

In further subsection, we first derive the small signal models for converter in the form $\dot{X} = AX + BU$ and $Y = CX + DU$ operating in CCM followed by DCM where X is a vector of state variables, U is the input vector and Y is the output vector defined by $X = [v_{c_{in}} \ i_L \ v_c]$; $U = [v_{pv} \ v_d \ d]$; $Y = [i_{pv}]$.

4.2.1 CCM

The differential equations for ON and OFF states for non-ideal boost converter presented in Fig 4.1 are given by (4.1)-(4.6). Here, R is the load connected at the output of the boost converter and all the variables in small letters indicate that they are time varying. Equations (4.1)-(4.6) are averaged with duty cycle (d) and linearised (Erickson and Maksimovic, 2007) to yield the small signal models given by (4.7) and (4.8) and the coefficients are given in Appendix.

To understand the effect of MPP (maximum power point) on the converter stability, we see the perturbation effect of d on i_{pv} . Therefore, transfer function, $\frac{i_{pv}(s)}{d(s)}$ is derived from the small signal models using standard techniques and is given by (4.9).

ON State

$$\frac{dv_{c_{in}}}{dt} = \frac{1}{C_{in}} (i_{pv} - i_L) = \frac{1}{r_{c_{in}} C_{in}} (v_{pv} - v_{c_{in}}) \quad (4.1)$$

$$\frac{di_L}{dt} = \frac{1}{L} (v_{pv} - i_L (r_L + r_{sw})) \quad (4.2)$$

$$\frac{dv_c}{dt} = -\frac{v_o}{RC} = -\frac{v_c}{R + r_c} \quad (4.3)$$

OFF state

$$\frac{dv_{c_{in}}}{dt} = \frac{1}{C_{in}} (i_{pv} - i_L) = \frac{1}{r_{c_{in}} C_{in}} (v_{pv} - v_{c_{in}}) \quad (4.4)$$

$$\frac{di_L}{dt} = \frac{1}{L} \left(v_{pv} - i_L \left(r_L + \frac{Rr_c}{R + r_c} \right) - v_d - \frac{Rv_c}{R + r_c} \right) \quad (4.5)$$

$$\frac{dv_c}{dt} = \frac{1}{C} \left\{ i_L \left(\frac{R}{R + r_c} \right) - \frac{v_c}{R + r_c} \right\} \quad (4.6)$$

$$\begin{aligned} \begin{bmatrix} \hat{v}_{c_{in}} \\ \hat{i}_L \\ \hat{v}_c \end{bmatrix} &= \begin{bmatrix} a_{11} & a_{12} & a_{13} \\ a_{21} & a_{22} & a_{23} \\ a_{31} & a_{32} & a_{33} \end{bmatrix} \begin{bmatrix} \hat{v}_{c_{in}} \\ \hat{i}_L \\ \hat{v}_c \end{bmatrix} \\ &+ \begin{bmatrix} b_{11} & b_{12} & b_{13} \\ b_{21} & b_{22} & b_{23} \\ b_{31} & b_{32} & b_{33} \end{bmatrix} \begin{bmatrix} \hat{v}_{pv} \\ \hat{v}_d \\ \hat{d} \end{bmatrix} \end{aligned} \quad (4.7)$$

$$\begin{aligned} \begin{bmatrix} \hat{v}_o \\ \hat{i}_{pv} \end{bmatrix} &= \begin{bmatrix} c_{11} & c_{12} & c_{13} \\ c_{21} & c_{22} & c_{23} \end{bmatrix} \begin{bmatrix} \hat{v}_{c_{in}} \\ \hat{i}_L \\ \hat{v}_c \end{bmatrix} \\ &+ \begin{bmatrix} e_{11} & e_{12} & e_{13} \\ e_{21} & e_{22} & e_{23} \end{bmatrix} \begin{bmatrix} \hat{v}_{pv} \\ \hat{v}_d \\ \hat{d} \end{bmatrix} \end{aligned} \quad (4.8)$$

$$\frac{i_{pv}(s)}{d(s)} = \frac{b_{23}(s - a_{11}) \left((s - a_{33}) + \frac{a_{23}B_{33}}{b_{23}} \right)}{(s - a_{11})((s - a_{22})(s - a_{33}) - a_{32}a_{23})} \quad (4.9)$$

4.2.2 DCM

The differential equations governing the converter operation in DCM are given (4.10)-(4.19). The differential equations are first averaged with duty cycles (d and d_1). Here d is the ratio of ON time of the switch (s) to the total switching period and d_1 is the ratio of the time taken by the inductor current to reach zero during the OFF state of the switch (S), to the total switching period. The averaged model containing d and d_1 should now be modified to eliminate d_1 (Sun et al., 2001).

ON State

$$\frac{dv_{c_{in}}}{dt} = \frac{1}{C_{in}} (i_{pv} - i_L) = \frac{1}{r_{c_{in}} C_{in}} (v_{pv} - v_{c_{in}}) \quad (4.10)$$

$$\frac{di_L}{dt} = \frac{1}{L} (v_{pv} - i_L (r_L + r_{sw})) \quad (4.11)$$

$$\frac{dv_c}{dt} = -\frac{v_o}{RC} = -\frac{v_c}{R + r_c} \quad (4.12)$$

OFF state

$$\frac{dv_{c_{in}}}{dt} = \frac{1}{C_{in}} (i_{pv} - i_L) = \frac{1}{r_{c_{in}} C_{in}} (v_{pv} - v_{c_{in}}) \quad (4.13)$$

$$\frac{di_L}{dt} = \frac{1}{L} \left(v_{pv} - i_L \left(r_L + \frac{Rr_c}{R + r_c} \right) - v_d - R \frac{v_c}{R + r_c} \right) \quad (4.14)$$

$$\frac{dv_c}{dt} = \frac{1}{C} \left\{ i_L \left(\frac{R}{R + r_c} \right) - \frac{v_c}{R + r_c} \right\} \quad (4.15)$$

$$(4.16)$$

OFF state with inductor de-energized

$$\frac{dv_{c_{in}}}{dt} = \frac{1}{C_{in}} (i_{pv} - i_L) = \frac{1}{r_{c_{in}} C_{in}} (v_{pv} - v_{c_{in}}) \quad (4.17)$$

$$\frac{di_L}{dt} = 0 \quad (4.18)$$

$$\frac{dv_c}{dt} = -\frac{v_o}{RC} = -\frac{v_c}{R + r_c} \quad (4.19)$$

we know that the maximum inductor current $i_{l_{max}}$ and average inductor current \bar{i}_L of a boost converter are given by .

$$i_{l_{max}} = \frac{v_{pv} d T_s}{L} \quad (4.20)$$

$$\bar{i}_L = \frac{i_{l_{max}}}{2} (d + d_1) \quad (4.21)$$

substituting (4.20) in (4.21) we get,

$$d_1 = \frac{2L\bar{i}_L}{dT_s (v_{pv} - \bar{i}_L (r_L + r_{sw}))} - d \quad (4.22)$$

where $T_s = \frac{1}{f_s}$ and f_s is the switching frequency of the converter. The equation (4.22) which expresses d_1 as a function of d is further substituted in averaged model to make it independent of d_1 . The model thus obtained is linearised to obtain the small signal model given by (4.23) and (4.24) and the co-coefficients are given in Appendix.

$$\begin{aligned} \begin{bmatrix} \hat{v}_{c_{in}} \\ \hat{i}_L \\ \hat{v}_c \end{bmatrix} &= \begin{bmatrix} A_{11} & A_{12} & A_{13} \\ A_{21} & A_{22} & A_{23} \\ A_{31} & A_{32} & A_{33} \end{bmatrix} \begin{bmatrix} \hat{v}_{c_{in}} \\ \hat{i}_L \\ \hat{v}_c \end{bmatrix} \\ &+ \begin{bmatrix} B_{11} & B_{12} & B_{13} \\ B_{21} & B_{22} & B_{23} \\ B_{31} & B_{32} & B_{33} \end{bmatrix} \begin{bmatrix} \hat{v}_{pv} \\ \hat{v}_d \\ \hat{d} \end{bmatrix} \end{aligned} \quad (4.23)$$

$$\begin{aligned} \begin{bmatrix} \hat{v}_o \\ \hat{i}_{pv} \end{bmatrix} &= \begin{bmatrix} C_{11} & C_{12} & C_{13} \\ C_{21} & C_{22} & C_{23} \end{bmatrix} \begin{bmatrix} \hat{v}_{c_{in}} \\ \hat{i}_L \\ \hat{v}_c \end{bmatrix} \\ &+ \begin{bmatrix} E_{11} & E_{12} & E_{13} \\ E_{21} & E_{22} & E_{23} \end{bmatrix} \begin{bmatrix} \hat{v}_{pv} \\ \hat{v}_d \\ \hat{d} \end{bmatrix} \end{aligned} \quad (4.24)$$

Once the small signal model is derived, it is now convenient to obtain the transfer function $\frac{i_{pv}(s)}{d(s)}$ and is given by (4.25).

$$\frac{i_{pv}(s)}{d(s)} = \frac{B_{23}(s - A_{11}) \left((s - A_{33}) + \frac{A_{23}B_{33}}{B_{23}} \right)}{(s - A_{11})((s - A_{22})(s - A_{33}) - A_{32}A_{23})} \quad (4.25)$$

4.2.3 Inferences

Following are the inferences drawn from comparing (4.9) and (4.25).

- In both cases, there is a pole-zero cancellation at $s = -\frac{1}{r_{c_{in}}C_{in}}$. Since none of the other terms contain $r_{c_{in}}$ and C_{in} , the stability is independent of input capacitor.
- There is no extra pole or zero addition with respect to each case. The number of poles/zeros in CCM is same as the number of poles/zeros in DCM.
- The zero in both the cases lies in LHP and is a function of r_c , load, and output capacitance.
- The characteristic equation in both the cases contain all positive coefficients and according to Routh–Hurwitz criteria for a second-order system, the system is stable for all conditions.

The inferences drawn above are not just valid for $\frac{i_{pv}(s)}{d(s)}$, through derivations it can also be shown that for the transfer function $\frac{v_{pv}(s)}{d(s)}$ the same inferences can be drawn. Therefore, it can be concluded that MPPT system involving boost converter operating in both CCM and DCM are open loop stable, and their stability is independent of input capacitor and its esr.

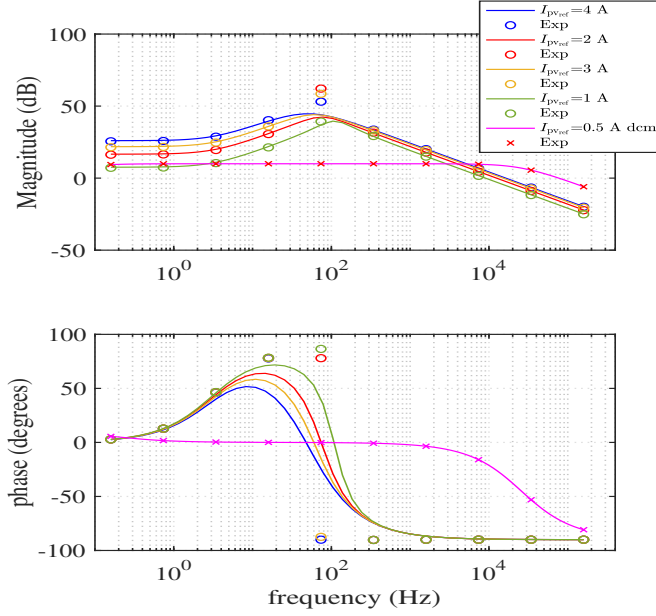


Figure 4.3: Bode plots showing open loop stability under constant current mode in both CCM and DCM case

4.2.4 Results and discussion

A PV panel with $P_{MPP, ref} = 74.5$ W, $I_{MPP, ref} = 4.4$ A, $V_{MPP, ref} = 17$ V is considered here for experimentation (the datasheet parameters are given in Table 2.1). and term “ref” indicates standard test conditions. A total of 4 panels are connected in series which makes the rating of the system equals 300 W. A boost converter with $C_{in} = 2000$ μ F, $r_{cin} = 0.016$ Ω , $L = 1.35$ mH, $r_L = 0.7$ Ω , $r_{sw} = 50$ m Ω , $v_d = 1.65$ V, $C = 1000$ μ F, $f_s = 25$ kHz and $r_c = 0.032$ Ω is used as a power electronic interface between PV simulator and load. A variable rheostat is used as a load on the output side of the boost converter. The gating pulse required to trigger the IGBT switch is generated using a dSPACE microlab box. The bode plots generated by the small signal models are verified using PSIM simulation run in AC sweep mode. To demonstrate the open loop stability of the plant (boost converter), bode plot for transfer function $\frac{\hat{i}_{pv}}{d}$ is plotted for both CCM and DCM and is shown in Fig. 4.3. The PV system is run at constant current mode for $i_{pv} = 4$ A, 2 A, 3 A and 1 A in CCM and the results are presented. It is seen that in all the four cases, the gain margin (GM) is infinity and the phase margin (PM) is close to 90.3° which indicates that the system is stable. It can also be seen that, there is low frequency zero which creates 20dB/dec

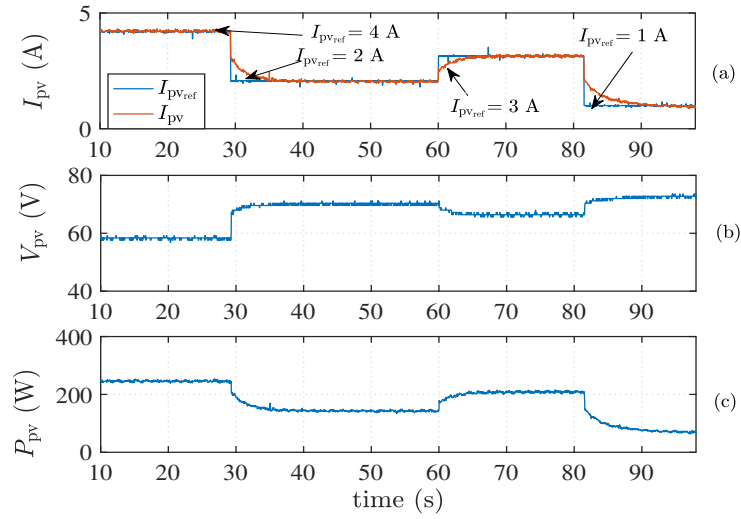


Figure 4.4: Experimental curves of PV system under constant current mode - CCM

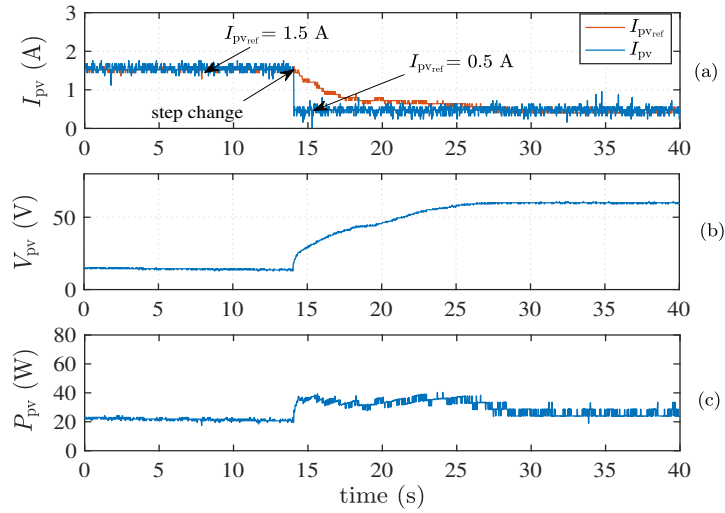


Figure 4.5: Experimental curves of PV system under constant current mode - DCM

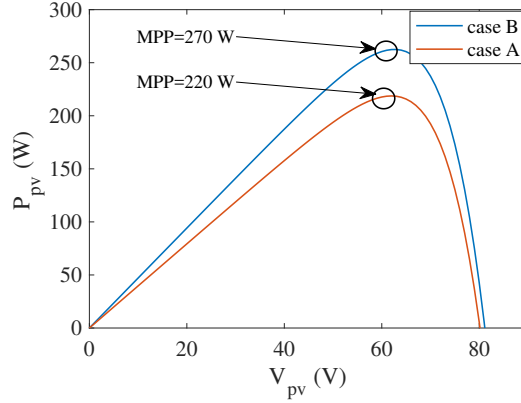


Figure 4.6: Simulated PV curves showing MPP value for case A and case B

rise, followed by two successive poles eventually causing 20dB/dec fall. From transfer function (4.9) it can be seen that, there are totally 2 zeroes and 3 poles in the system and pole zero cancellation occurs at high frequency at $s = -\frac{1}{r_{cin}C_{in}} = 33.33 \text{ kHz}$. Since there is pole zero cancellation at 33.33 kHz, there is no rate of rise/fall in dB levels at that frequency. For DCM case, the transfer function is plotted for $i_{pv} = 0.5 \text{ A}$ and $R = 250 \Omega$. The GM is found to be infinity and PM is close to 90° which again indicate open loop stability. In this case, the poles and zeroes are found to occur at the close vicinities thereby causing flat bode curve. The results from the simulations are verified from the results from PSIM simulation and are found to be in agreement with each other.

The PV system is first run in a constant current mode for reference PV currents $i_{pv}^* = 4 \text{ A}$, 2 A , 3 A , and 1 A . It is seen from Fig. 4.4a that the actual PV current tracks the reference current values in all the four cases. The corresponding PV voltage and power is shown in Fig. 4.4b and Fig. 4.4c respectively. The load resistance R is now increased to 120Ω , and inductor L was cut down to $270 \mu \text{ H}$ so that the PV enters into DCM and the system is tested for $i_{pv}^* = 0.5 \text{ A}$ at $t=14 \text{ s}$. It is seen from Fig. 4.5a that the actual PV current could track the reference current even in DCM. The corresponding PV voltage and power are shown in Fig. 4.5b and Fig. 4.5c respectively. The system is further tested for an MPPT application where the value of i_{pv}^* is obtained from an MPPT algorithm as shown in Fig. 5.3. Universal Perturb and Observe is used as an MPPT algorithm for this case. The PV curves indicating the MPP values is shown in Fig. 4.6. Through PV simulator an initial irradiance of 800 W/m^2 is maintained. It can be seen from Fig 4.7 that the i_{pv}^* tracks the reference

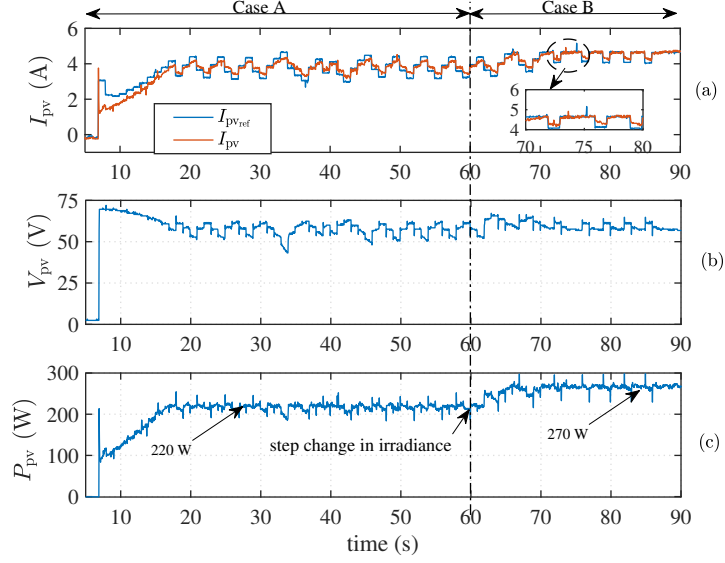


Figure 4.7: Experimental curves of PV system under MPPT - CCM

current generated by MPP algorithm successfully. The tracked MPP is 220 W which is same as the MPP shown in Fig 4.6. At $t=60$ s (Fig 4.7), the irradiance is changed to 950 W/m^2 , and the i_{pv}^* tracks reference current for this step change in irradiance, and the tracked power is 270 W. The panel temperature in both the cases is maintained at 50°C .

4.3 Small signal model of Motor pump system

The dynamic equations governing induction motor and pump are already presented in 3.4.3 however they are given here for reference and is given by (4.26)-(4.29). These dynamic equations are linearised over the operating points to obtain the small signal model. The small signal model is given by (4.30) and (4.31).

$$\begin{bmatrix} \dot{\psi}_{ds} \\ \dot{\psi}_{qs} \\ \dot{\psi}_{dr} \\ \dot{\psi}_{qr} \end{bmatrix} = - \begin{bmatrix} r_s & \omega L_s & 0 & \omega L_m \\ \omega L_s & r_s & \omega L_m & 0 \\ 0 & -\omega_s L_m & r_r & -\omega_s L_r \\ \omega_s L_m & 0 & \omega_s L_r & r_r \end{bmatrix} \begin{bmatrix} i_{ds} \\ i_{qs} \\ i_{dr} \\ i_{qr} \end{bmatrix} + \begin{bmatrix} v_{ds} \\ v_{qs} \\ v_{dr} \\ v_{qr} \end{bmatrix} \quad (4.26)$$

$$\begin{bmatrix} \psi_{ds} \\ \psi_{qs} \\ \psi_{dr} \\ \psi_{qr} \end{bmatrix} = \begin{bmatrix} L_s & 0 & L_m & 0 \\ 0 & L_s & 0 & L_m \\ L_m & 0 & L_r & 0 \\ 0 & L_m & 0 & L_r \end{bmatrix} \begin{bmatrix} i_{ds} \\ i_{qs} \\ i_{dr} \\ i_{qr} \end{bmatrix} \quad (4.27)$$

$$t_e = \frac{3P}{2}(\psi_{ds}i_{qs} - \psi_{qs}i_{ds}) \quad (4.28)$$

$$\frac{d\omega_r}{dt} = \frac{P}{2J}(t_e - k\omega_r^2) \quad (4.29)$$

$$\begin{bmatrix} \hat{i}_{ds} \\ \hat{i}_{qs} \\ \hat{i}_{dr} \\ \hat{i}_{qr} \\ \hat{\omega}_r \end{bmatrix} = \begin{bmatrix} -\frac{r_s L_r}{L_x} & \frac{\omega L_s L_r - \omega_s L_m^2}{L_x} & \frac{r_r L_m}{L_x} & \frac{\omega L_m L_r - \omega_s L_m L_r}{L_x} & \frac{P}{2} \frac{L_m I_{qs} + L_r I_{qr} L_m}{L_x} \\ -\frac{(\omega L_s L_r - \omega_s L_m^2)}{L_x} & -\frac{r_s L_r}{L_x} & -\frac{(\omega L_m L_r - \omega_s L_m L_r)}{L_x} & \frac{r_r L_m}{L_x} & -\frac{P}{2} \frac{L_m I_{ds} + L_r I_{dr} L_m}{L_x} \\ \frac{r_s L_m}{L_x} & \frac{\omega L_m L_s - \omega_s L_m L_s}{L_x} & -\frac{r_r L_s}{L_x} & \frac{\omega L_m^2 - \omega_s L_r L_s}{L_x} & -\frac{P}{2} \frac{L_m I_{qs} + L_r I_{qr} L_s}{L_x} \\ -\frac{(\omega L_m L_s - \omega_s L_m L_s)}{L_x} & \frac{r_r L_s}{L_x} & \frac{(\omega L_m^2 - \omega_s L_r L_s)}{L_x} & \frac{r_s L_m}{L_x} & \frac{P}{2} \frac{L_m I_{ds} + L_r I_{dr} L_s}{L_x} \\ -\frac{3L_m I_{qr}}{J} & \frac{3L_m I_{dr}}{J} & \frac{3L_m I_{qs}}{J} & -\frac{3L_m I_{ds}}{J} & 0 \end{bmatrix}$$

$$\begin{bmatrix} \hat{i}_{ds} \\ \hat{i}_{qs} \\ \hat{i}_{dr} \\ \hat{i}_{qr} \\ \hat{\omega}_r \end{bmatrix} + \begin{bmatrix} \frac{L_r}{L_x} & 0 & \frac{L_m}{L_x} & 0 & 0 & \frac{-s(L_m I_{qs} + L_m I_{qr})L_m + (L_s I_{qs} + L_m I_{dr})L_r}{L_x} \\ 0 & \frac{L_r}{L_x} & 0 & \frac{L_m}{L_x} & 0 & \frac{s(L_m I_{ds} + L_r I_{dr})L_m + (L_s I_{ds} + L_m I_{dr})L_r}{L_x} \\ -\frac{L_m}{L_x} & 0 & \frac{L_s}{L_x} & 0 & 0 & \frac{-(L_s I_{qs} + L_m I_{qr})L_m + s(L_m I_{qs} + L_m I_{qr})L_s}{L_x} \\ 0 & -\frac{L_m}{L_x} & 0 & \frac{L_s}{L_x} & 0 & \frac{(L_s I_{ds} + L_m I_{dr})L_m - s(L_m I_{ds} + L_r I_{dr})L_s}{L_x} \\ 0 & 0 & 0 & 0 & -\frac{1}{JL_x} & 0 \end{bmatrix} \begin{bmatrix} \hat{v}_{ds} \\ \hat{v}_{qs} \\ 0 \\ 0 \\ \hat{t}_l \\ \hat{\omega}_r \end{bmatrix} \quad (4.30)$$

$$\begin{bmatrix} \hat{\omega}_r \end{bmatrix} = \begin{bmatrix} 0 & 0 & 0 & 0 & 1 \end{bmatrix} \begin{bmatrix} \hat{i}_{ds} \\ \hat{i}_{qs} \\ \hat{i}_{dr} \\ \hat{i}_{qr} \\ \hat{\omega}_r \end{bmatrix} + \begin{bmatrix} 0 \end{bmatrix} \begin{bmatrix} \hat{v}_{ds} \\ \hat{v}_{qs} \\ 0 \\ 0 \\ \hat{t}_l \\ \hat{\omega}_r \end{bmatrix} \quad (4.31)$$

Here, $L_x = L_s L_r - L_m^2$

4.4 Stability of water pumping system

The small signal models are the means of studying system stability. The small signal models for boost converter and IM pump system are presented in this section. The effect of insolation and shading on the system poles and zeros are seen here. The

bode plots are plotted for the same shading pattern in Table 3.2. The results from chapter 3 forms the input to the small signal models. The bode plots are verified from frequency plots of PSIM.

In section 4.2.3 it was concluded that, the stability of the boost converter is found to be independent of input capacitance and also, the poles and zeros always lie in left half of s-plane. Accordingly, in frequency domain one would expect a positive GM and PM and the same has been depicted in Fig 4.8a. In all the cases of CCM and DCM, the GM and PM is found to be positive. The results from PSIM is also in agreement with results from the mathematical model. The small signal model of IM pump system is complex, and deriving transfer function manually is tedious. Therefore, the conclusions are drawn based on the bode plots. Bode plot for $\frac{\hat{w}_r}{f}$ is plotted and verified from results of PSIM as shown in Fig 4.8b. It is seen that, the IM Pump system has stable GM and PM for both CCM and DCM operations.

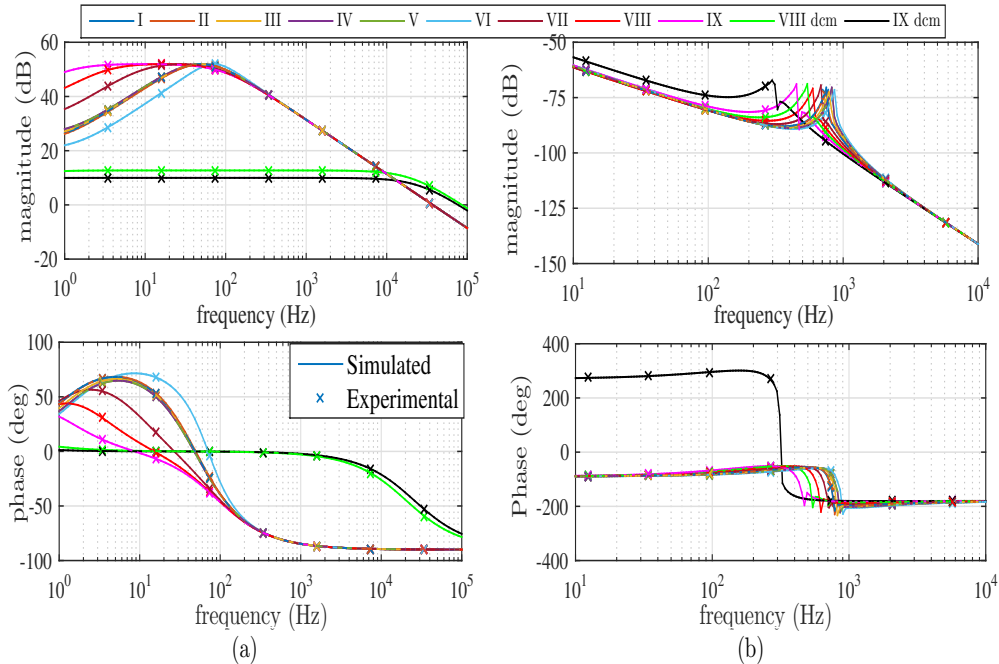


Figure 4.8: Bode plots of a) DC-DC Converter b) IM pump system for various shading conditions

4.5 Conclusion

In this chapter, small signal models for boost converter and induction motor pump system is presented. In the first section of the chapter, the effect of addition of capacitor at the PV terminals on the system stability has been investigated by deriving small signal models. The models are derived for both CCM and DCM considering the parasitics. In both the modes of operation it is observed that, there exists an identical pole and a zero pair and are found to be the functions of input capacitor and its esr. Through pole zero cancellations it is also concluded that the stability of the system is independent of the input capacitor and its esr. It is also proven by Routh–Hurwitz criteria that the system by itself is open loop stable with all poles and zeroes on the left half of s plane. Experimental validation also confirms the same.

In the later section, small signal of the motor pump system is derived and finally the stability of the entire water pump system is presented by plotting the bode plots. It is seen that, the system is stable for all shading conditions with positive gain and phase margins. The results from PSIM is in total agreement with the results from the small signal models.

In all the chapters till now, the effects of shading on pump systems are studied through steady state, dynamic and stability models. In the next chapter, the effects of cables on induction motor failure are studied through experimentations and a cost effective solution is proposed thereby increasing the reliability of the over all system.

Chapter 5

Effect of LC filters on water pumping systems

Contents

5.1	Introduction	87
5.1.1	Objectives	88
5.2	System Description	88
5.3	Selection of LC Filter Components	89
5.4	Design of Filter Inductor	90
5.4.1	Lumped Gap Inductor	90
5.4.2	Uniformly Distributed Gap Inductor	91
5.4.3	Discretely Distributed Gap Inductor	91
5.5	Results and Discussion	92
5.5.1	With lumped gap Inductor in the LC filter	93
5.5.2	With Proposed Inductor in the LC filter	95
5.6	Conclusion	100

5.1 Introduction

This chapter presents the experimental study of the effectiveness of the LC filter in PV fed water pumping systems. This study is very important in water pumping

applications where prolonged running conditions is a major concern. LC filters are connected at the terminals of the inverter to avoid transient over voltages across the induction machine. thereby avoiding motor insulation failure The conventional LC filter with lumped gap inductor is studied initially. The temperature of the filter inductor is monitored to study its behaviour. It is inferred that the inductor temperature increases drastically due to the high winding losses and therefore may lead to motor failure when run for longer duration. The inductor is replaced with uniformly distributed (powdered) core and low cost discretely distributed gap core so as to minimize the losses. Comparitive study between the conventional and proposed inductors is carried out. It is inferred that discretely distributed gap inductors are a better choice over powdered core inductors. The experimentation is carried out on a 3-hp induction motor and results with lumped gap and discretely distributed gap inductors are presented along with their thermal profiles. Results show that, the discrete distributed gap inductor is the cost effective solution for the LC filter failures in water pumping applications.

5.1.1 Objectives

The objectives of this chapter are

- The real time applications of quasi distributed inductors as a cost effective solution in water pumping systems.
- The reduction in size of the inductors when a more permeable material like iron or CRGO is used (this comparision is with respect to the powdered cores).

5.2 System Description

The circuit of PV fed water pumping system is shown in Fig.5.1. The input power to the system is fed from the PV array. A boost converter ensures maximum power transfer from the PV to inverter. The induction motor is controlled through a simple v/f control strategy. Space vector modulation is the PWM technique employed to generate pulses for the inverter. The inverter terminals are connected to an LC filter. A 100m cable connects the filter to the induction machine. This induction motor is coupled to the pump. The speed of the motor is controlled by controlling the stator frequency. DC link voltage maintained is 600V.

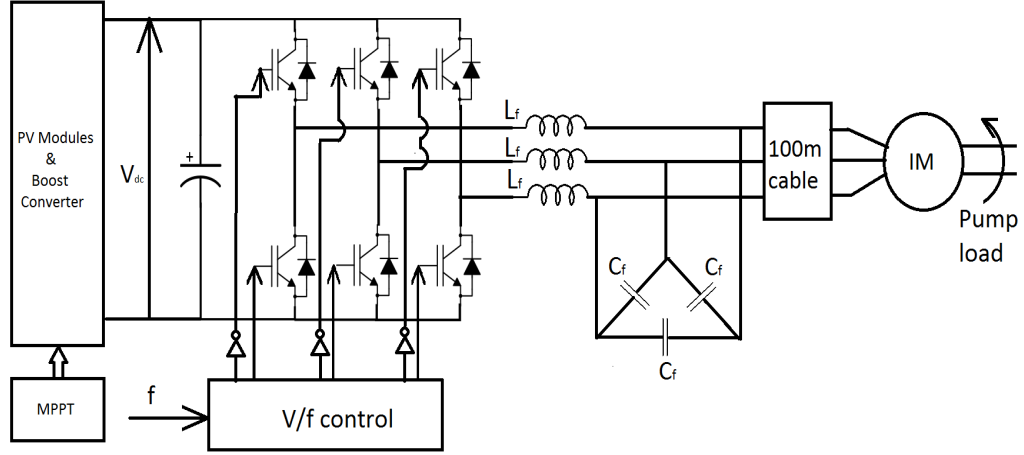


Figure 5.1: Circuit diagram of the water pumping system with LC filters

5.3 Selection of LC Filter Components

The LC filter has been designed as given in (von Jouanne and Enjeti, 1996). The normalized peak motor terminal voltage as a function of rise time(t_r) is written as

$$\frac{Pk.MotorTerm.V}{V_{dc}} = \frac{3X10^{-6}l_c\tau_L}{500t_r} + 1 \quad (5.1)$$

where, V_{dc} is the DC bus voltage, l_c is the cable length in ft, τ_L is the reflection co-effectient at the load.

In order to avoid overvoltages,

$$\frac{3X10^{-6}l_c\tau_L}{500t_r} \ll 1 \quad (5.2)$$

Setting, $\frac{Pk.MotorTerm.V}{V_{dc}}$ to 1.2(von Jouanne and Enjeti, 1996) in (5.1), $t_r = 8.856\mu s$. The relationship between motor terminal voltage and the rise time(t_r) is given as

$$v(t) = V_{dc} \left(1 - e^{-\frac{t_r}{\tau}}\right) \quad (5.3)$$

where,

$$\tau = \sqrt{L_f C_f} \quad (5.4)$$

For the filtering action, it is essential that

$$\sqrt{L_f C_f} \geq t_r \quad (5.5)$$

where,

$$C_f \geq l_c \times 3 \times 10^{-10} \quad (5.6)$$

For, $l_c = 328 \text{ft}(100\text{m})$, $C_f \geq 0.0984 \mu\text{F}$ and $L_f \geq 0.797 \text{mH}$ Therefore, the value of L_f and C_f are chosen as 1.8mH and $8 \mu\text{F}$.

5.4 Design of Filter Inductor

In this section, the design of lumped gap, quasi distributed gap and uniformly distributed gap filter inductors are presented. Area product method has been adopted to design the filter inductor as it is universally accepted and followed.

5.4.1 Lumped Gap Inductor

For $L_f=1.8 \text{mH}$ and I_p (inductor peak current)= 8A , the energy(E) stored in the inductor is 57.6mJ . Therefore,

$$A_p = A_w \times A_c = \frac{2E}{W_c \times C F \times J \times B} = 8.57 \text{cm}^4 \quad (5.7)$$

where, A_c and A_w are the core and window area respectively. W_c is the window utilization factor (here it is taken as 0.2), CF is the crest factor (1.414 for sine wave), J is the current density (2.5A/mm^2) and B is the flux density (1.9T for a steel sheet). A steel sheet EE core has been chosen for the design with $A_w=850 \text{mm}^2$ and $A_c=101.05 \text{mm}^2$. The number of turns N and air gap length (l_g) are,

$$N = \frac{L_f I_p}{A_c B} = 75 \text{turns} \quad (5.8)$$

$$l_g = \frac{N^2 \mu_o A_c}{L_f} = 0.418 \text{mm} \quad (5.9)$$

The effect of fringing has to be taken into account, Fringing factor F is calculated as follows.

$$F = 1 + \frac{l_g}{\sqrt{A_c}} \ln \frac{2G}{l_g} = 1.25 \quad (5.10)$$

where, G is the window length. With fringing into consideration, the design is iterated to yield final design values. The design values are tabulated in Table 5.1.

5.4.2 Uniformly Distributed Gap Inductor

MPP cores (Magnetic's powdered core) has a flux density of 2000 Gauss under AC conditions. They are known for low hysteresis and eddy current losses, excellent inductance stability. For the same value of E, the area product is found to be $81.47cm^4$. For the given area, from the standard available cores, $A_w=1640mm^2$ and $A_c=497mm^2$. The number of turns required is 145. Since the gaps are uniformly distributed, the calculation of air gap and fringing is not required.

5.4.3 Discretely Distributed Gap Inductor

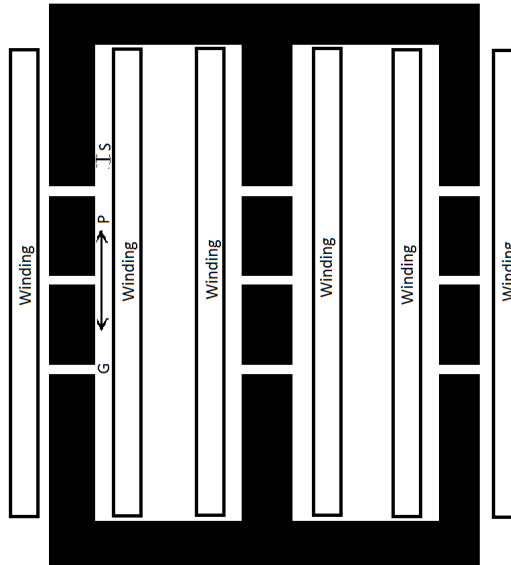


Figure 5.2: Cross sectional view of distributed gap inductor(not drawn to scale)

The distributed gap inductor is designed with the same EE core, with the dimensions as that of lumped gap inductor i.e., $A_w=850mm^2$ and $A_c=101.05mm^2$.

The lumped air gap is divided into three small air gaps of 0.1333mm each. The air gap pitch(P) and the space between the core and the winding(S) is so adjusted that the ratio of $P/S < 4$ (Hu and Sullivan, 2001) and the windings are spaced at a distance of 0.836mm which is twice the gap lengthKutkut and Divan (1998b). The value of F is 1.0956. The design is further iterated and is tabulated in Table 5.1. The cross sectional view of the distributed gap inductor is shown in Fig. 5.2.

Table 5.1: Comparison table

	LG	UDG	QDG
$A_p(cm^4)$	8.57	81.47	8.57
$A_c(cm^2)$	1.015	4.97	1.015
$A_w(cm^2)$	8.50	16.40	8.50
$B_{sat}(T)$	1.9	0.2	1.9
$l_g(cm)$	0.153		0.0523(each)
F	1.315		1.107
N	75	148	91
$L_f(\text{recalculated})(H)$	1.88m	1.8m	1.805m

Table 5.1 shows the comparison of the physical dimensions of lumped gap(LG), uniformly distributed gap(UDG) and quasi distributed gap (QDG) inductors. It is evident that, the area product(function of volume) of powdered cores(UDG) is much higher compared to CRGO core inductors due to their lower flux density value. The number of turns required is also higher. On the other hand, the quasi distributed air gap inductor has similar dimensions as that of lumped gap inductor. The fringing field is lower. Since, the powdered cores are voluminous, require more turns, low permeable and are available at higher cost, it is therefore clear that discretely distributed air gap inductor forms a better alternative to lumped gap and uniformly distributed gap inductor in terms of lower size, lower cost and reduced losses.

5.5 Results and Discussion

In this section, the performance of a Induction motor drive without filters, with lumped air gap inductor and with proposed(distributed air gap) inductors are presented. The water pumping system is normally designed for peak running power for at least 2hrs per day. In order to check the reliability of the filter inductor in water

pumping system, it is necessary to test the system at the peak power condition (at 50Hz frequency) for at least 3-4hrs. Therefore, the induction motor drive with lumped air gap and with discretely distributed air gap inductors are run for sufficiently long durations at peak power conditions and the temperature rise of the inductors are studied. The drive is later run at different stator frequencies (different speeds) to study its performance.

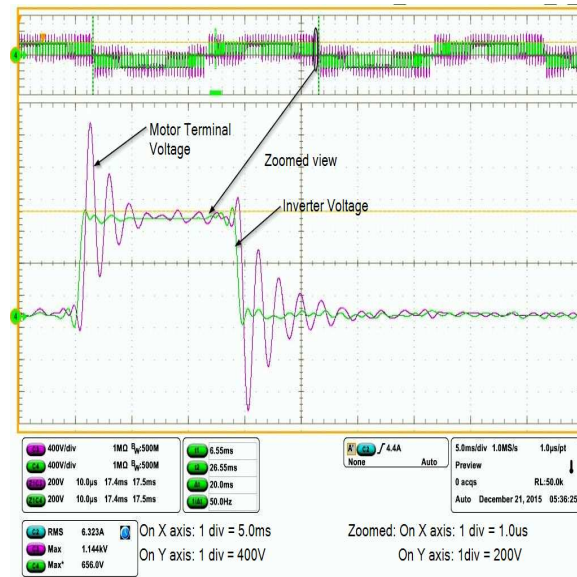


Figure 5.3: Motor terminal and Inverter output voltages - without filter

Fig.5.3 shows the over voltages in the drive system without incorporating LC filter. The DC bus is maintained at 600V and the stator frequency is 50Hz. It is seen that the L-L voltage at the machine terminals shoots upto 1.144kV which can cause insulation failure of submersible Induction motor pumps.

5.5.1 With lumped gap Inductor in the LC filter

A lumped gap LC filter (capacitors are delta connected) is connected to this system to mitigate the problem of over voltages. The results showing the stator terminal voltage, inverter terminal voltage and stator currents is presented in Fig.5.4. It is clear from the results that the overvoltages has been mitigated with the maximum machine terminal voltage of 564V. The peak to peak voltage across the inductor is 936V. The stator frequency is 50Hz.

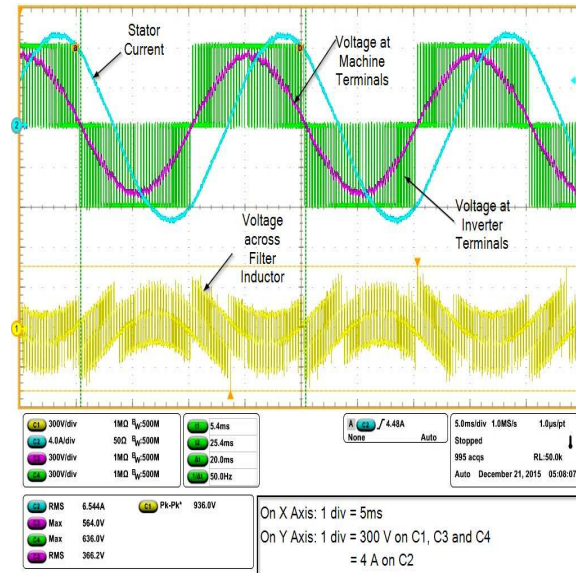


Figure 5.4: Motor terminal, Inverter terminal voltages and stator current - with lumped gap filter

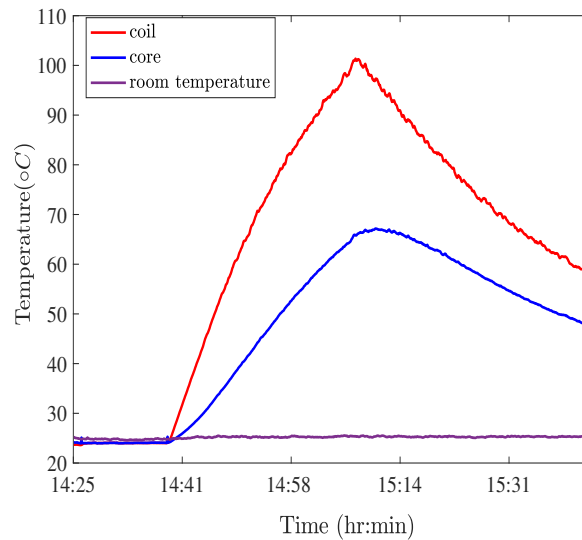


Figure 5.5: Temperature Profile of lumped air gap inductor

The drive is run at rated frequency of 50 Hz for 1hr 20min to check the temperature rise in the filter inductor and the motor draws constant power of rated value throughout the running period. The temperature profile of the inductor core and coil is shown in Fig.5.5. It is seen that at the start of the drive, the temperature of the coil and the core is 23°C, which is the room temperature. As the drive is kept running,

the temperature of the inductor rises exponentially. This exponential rise is because of the continuous heat dissipation in the inductor. At the end of 1hr 20min, the coil and the core temperatures are 102.5°C and 68°C respectively. It is important to note that the temperature does not get saturated even at the end of the running period. This high temperature might cause the LC filter failure. The system is turned off at the end of 1hr 20min to cool the inductor. The thermal images shot at the end of 1hr 20min are shown in Fig 5.6.

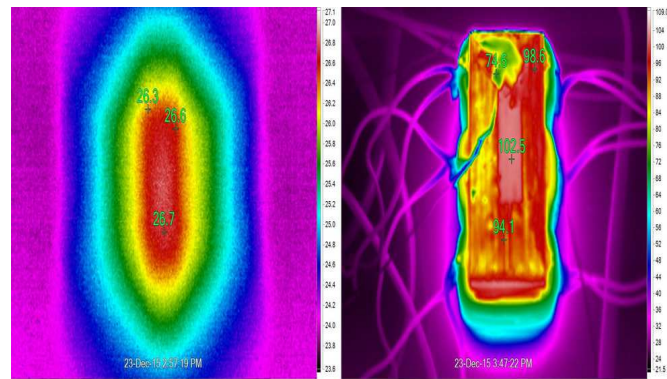


Figure 5.6: Thermal images of lumped air gap inductor - At the start (left image) and end(right image) of running period

5.5.2 With Proposed Inductor in the LC filter

The results showing L-L motor terminal voltage, inverter terminal voltage and stator currents with the proposed inductor are presented in Fig.5.7. It is clear from the results that the overvoltages has been mitigated with a maximum machine terminal voltage of 570V. The peak to peak voltage across the inductor is approximately 936V at a stator frequency is 50Hz, which is similar to previous case. However, with the redesigned inductor, the losses are reduced by a greater extent which is discussed later.

The drive is now run continuously for 5hrs (which is four times with lumped gap inductor) at the rated frequency of 50 Hz to check the temperature rise in the inductor. The temperature profile of the inductor is shown in Fig.5.8. It is seen that at the start of the drive, the temperature of the coil and the core is 23°C, which is almost same as room temperature. Though the temperature of the coil and the core rises exponentially at the initial stage, the temperature saturates to a value below 55°C. At

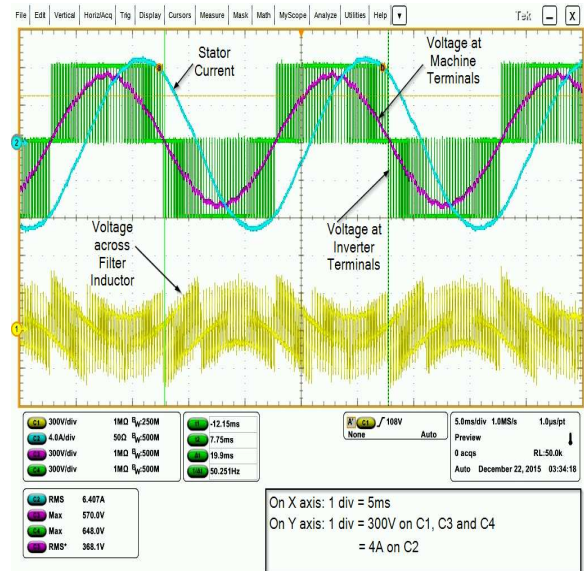


Figure 5.7: Motor terminal, Inverter terminal voltages and stator current - with discretely distributed air gap inductor

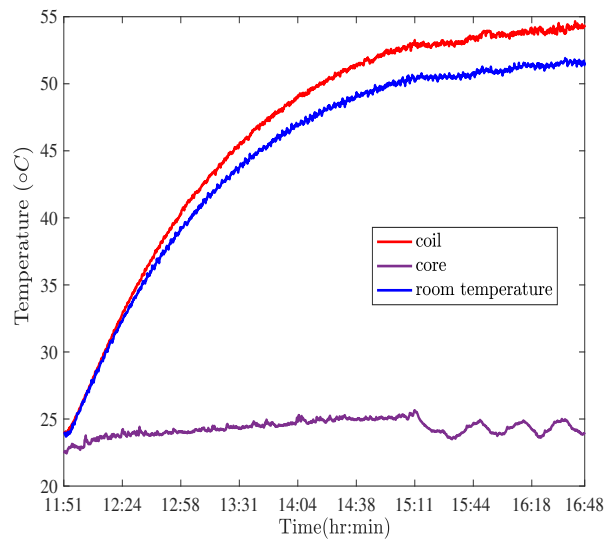


Figure 5.8: Temperature Profile of discretely distributed air gap inductor

the end of the 5th hour, the temperature of the coil and the core is found to be 54°C and 52°C respectively. It clearly shows that, with discretely distributed gap inductor the temperature levels do not exceed the limits and thereby avoid possible damage to the system. The thermal images shot at the end of 5 hrs are shown in Fig. 5.9.

Fig 5.10(a)-5.14(a) shows various performance plots. The drive is run at different

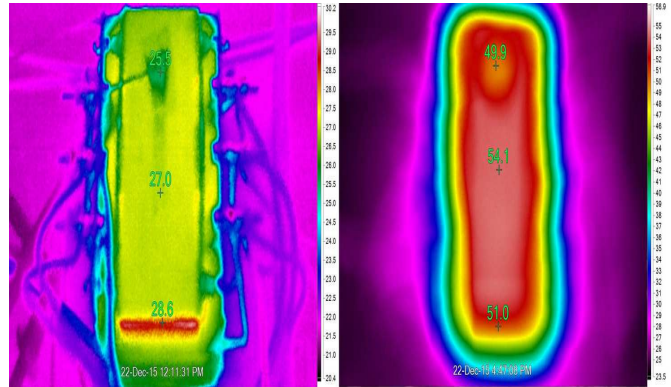


Figure 5.9: Thermal images of discretely distributed air gap inductor - At the start(left image) and end(right image) of running period

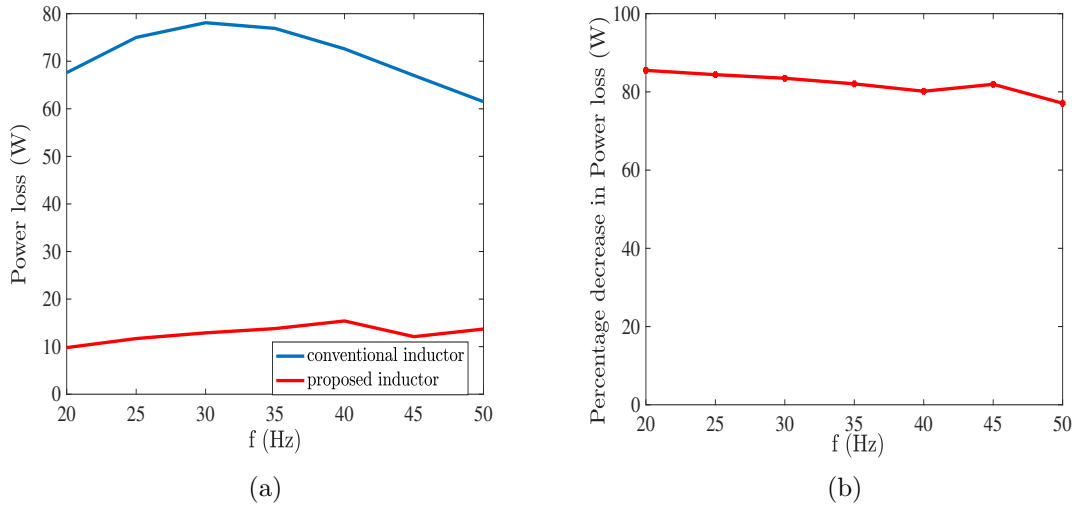


Figure 5.10: Power loss in inductors a) conventional and proposed b) percentage decrease

frequencies(at different input powers) and the corresponding losses, efficiency, power factors are presented.

The power loss in the inductors are presented in Fig. 5.10(a). The drive is run at different frequencies, from 20 Hz to 50 Hz. It is seen that there is a considerable reduction of power loss with incorporation of proposed inductor. A maximum reduction of losses upto 60 W is seen.

The plot of percentage decrease in power losses is shown in Fig. 5.10(b). The power loss is decreased by almost 80%. to 88% throughout the entire operating frequency.

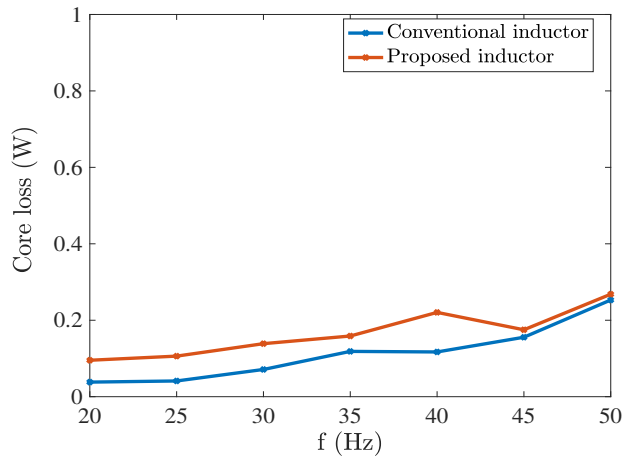


Figure 5.11: Comparison of inductor core losses

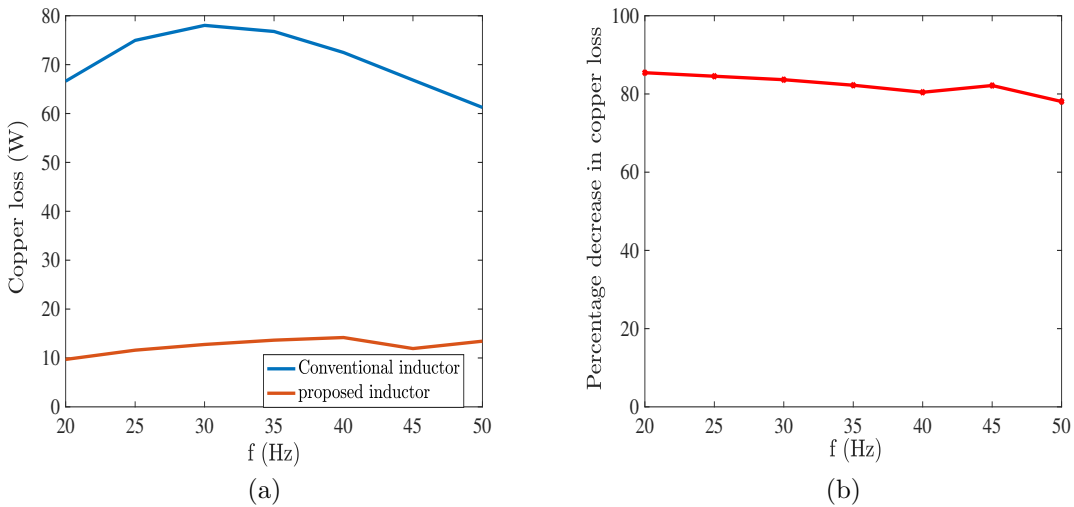


Figure 5.12: Copper loss in inductors a) conventional and proposed b) percentage decrease

The plots of inductor core losses and copper losses are shown in Fig 5.11 and Fig 5.12(a) respectively. There is a reduction in both core and copper losses over the entire frequency range. Copper losses forms the major portion of the entire losses. An approximate reduction of 80% to 88% throughout the entire operating frequency is visible in Fig. 5.12(b). The decrease in AC resistance when the conventional filter is replaced with proposed filter is shown in Fig. 5.13(a). It is seen that the decrease in the resistance is approximately 80%. The AC resistance at different frequencies was calculated from the voltage and current data taken from WT3000 spectrum analyzer.

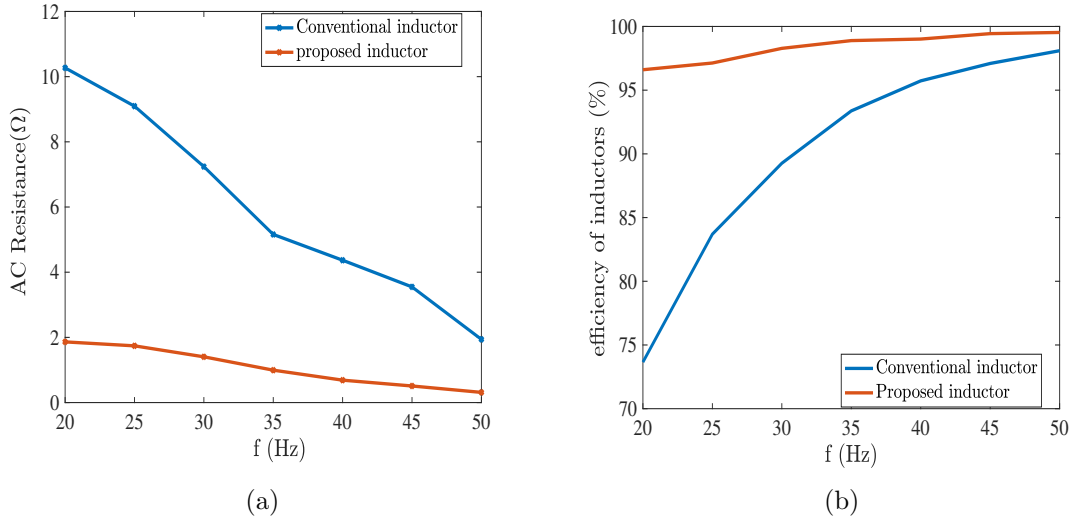
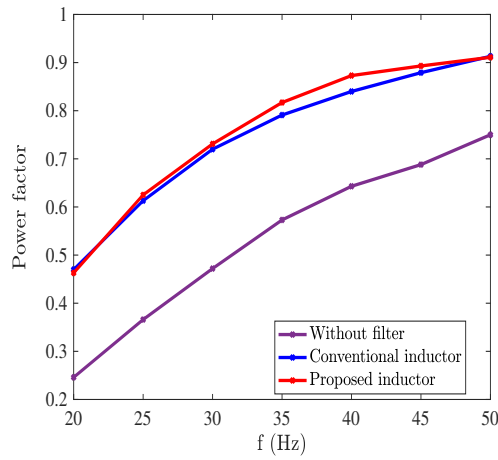


Figure 5.13: Comparison of a) AC resistances b) Efficiency of the conventional and proposed inductor

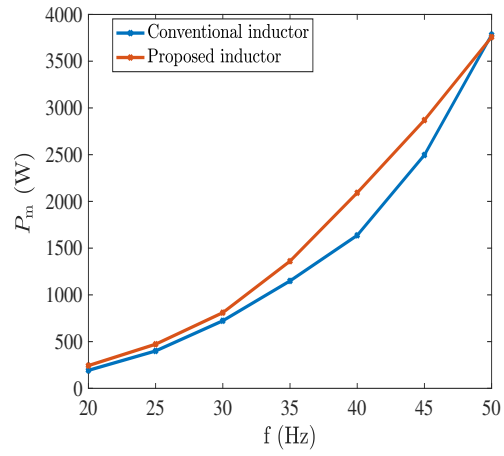
An efficiency plot of both inductors are presented in Fig. 5.13(b) to show the effectiveness of the proposed inductor. It seen from the figure that the efficiency of the proposed inductor varies between 96% to 99% and that of the conventional inductor varies between 74% to 96%. The efficiency of the conventional inductor is poor at lower power levels(lower frequencies), however, in case of proposed inductor, the efficiency is fairly good for all power levels(frequencies).

The variation of system power factor as a function of frequency without filter, with conventional filter and with the proposed filter are shown in Fig. 5.14(a). The power factor is very low without filter. The filter capacitors supplies the VAR, thereby improving the power factor. The power factor increases as the frequency increases. The power factor is improved slightly with the incorporation of proposed inductor as against conventional inductor.

Estimation of power available at the machine terminals is a very important performance criteria, as higher the power available, higher is the quantity of water being pumped. The power available at the machine terminals with the both the inductors and the plot is shown in Fig. 5.14(b). It is seen that , for the same insolation levels, the power availability is higher in case of the proposed inductor than the conventional inductor. A maximum difference of 211W is seen which is a considerable value. Since per phase loss reduction is 60-70W, the three phase power difference of 211W is seen.



(a)



(b)

Figure 5.14: Comparison of a) power factors b) Power available at machine terminals of the conventional and proposed inductor

5.6 Conclusion

In this chapter, the study of different kinds of LC filters in PV fed water pumping system is carried out to address the issue of induction motor insulation failure. It is found that, the high winding losses in lumped gap inductor causes the temperature of the inductor to rise exponentially. The proposed distributed air gap inductor minimizes the losses, thereby increasing the life span and improve overall reliability of the system. Experimental results and thermal images are presented to show the effectiveness of the proposed inductor.

Chapter 6

CONCLUSION AND FUTURE SCOPE

6.1 Conclusion

PV fed pumping systems are one of the promising applications of photovoltaic systems. Since they involve high initial investments and their energy conversion efficiency is low, utilizing the available PV output effectively is one of the important research areas. The characteristics of PV arrays are highly non linear and there exists a unique point at which maximum power can be extracted. With changes in insolation and temperature, this location of maximum power changes. Therefore, research focus is laid on development of faster yet simple algorithms to operate PV at maximum power point conditions. However, in practical scenario of a PV array containing more than panel, it is more likely that not all panels receive same irradiation. Under such circumstances, the PV characteristic exhibit multiple peaks and therefore, extracting maximum power is more challenging. This is one of the prime concern in water pumping applications where the working conditions are agricultural fields. Soiling of panels, shade of trees and clouds might cause conditions of partial shading and thereby cause decreased output. Therefore, one needs a clear understanding of the effects of partial shading on water pumps. One of the powerful tools to understand and analyze non linear systems like PV under such partial shading conditions is mathematical models. Therefore, in this thesis, a study on partial shading effects on water pumps is carried by mathematical modeling and verified by experiments.

The thesis presents detailed modeling of PV arrays and the modeled PV is further used to propose two fast converging analytical methods to compute maximum power point under partial shading conditions. The proposed techniques are simulated for smaller arrays till larger arrays and the results are verified by experimentations. The experimental results are found to be in good agreement with the simulations. Once the maximum power point tracking techniques are presented, they are further used to evaluate the performance of water pumping systems under partial shading conditions. Both dynamic and steady state models for boost converter, inverter and Induction motor water pumping systems are presented. From the simulation and experimental results, it is seen that if partial shading conditions are overlooked it might cause stress on switches and may even lead to discontinuous mode of DC–DC converter.

The water pumping systems under partial shading conditions are further studied through stability models by developing small signal models for DC–DC converter and IM pump system. It is seen that the input capacitor has no effect on the stability of the DC–DC converter. It is also inferred that the system is open loop stable.

Finally, an investigation on the effect of LC filter on the working of water pumps is presented. It is seen that the water pump often has a breakdown due to high losses in the conventional filter inductor which has lumped airgap. Experimental investigations are carried to replace the inductor with a quasi distributed inductor which reduces the losses in the filter thereby helping in uninterrupted working of the water pumps.

In nutshell, this thesis addresses the key points of stand alone water pumping systems and can also be used as a computer aided tool to study the PV fed pumping systems and thus helping in effective utilization of PV power.

6.2 Future scope

Based on the research carried out in this thesis, the recommendations for future research are as follows:

- The effect of partial shading on the performance of systems with PMSM pumps, BLDC pumps needs to be investigated
- The stability model of only boost converter has been presented this thesis. Since the stability is converter specific, the stability of other power electronic converters has to be investigated.

Appendix

Appendix A

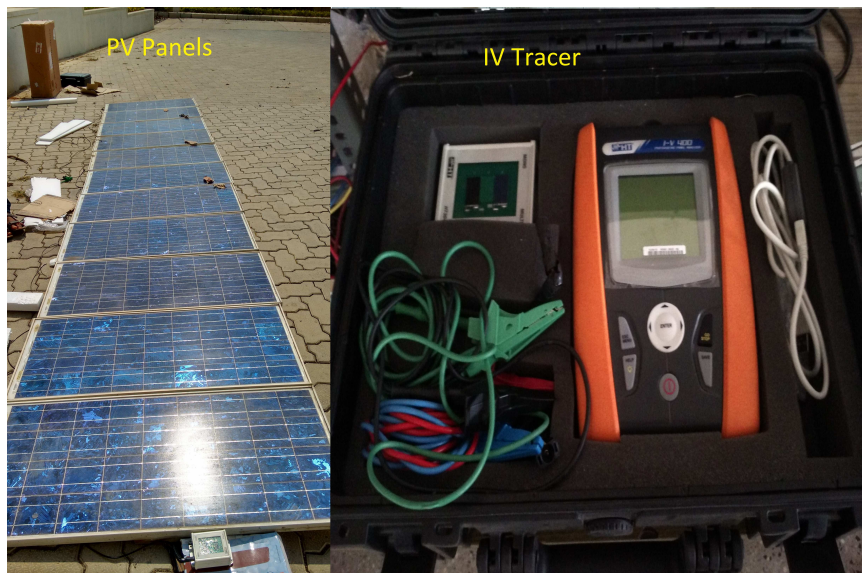


Figure 6.1: Prototype used to validate proposed PV Panel modeling

In this section, the experimental setup used to validate the simulation studies is presented. The experimentation is carried out in two phases. In first phase, the experimentation for proposed mathematical model to verify PV characteristics is carried out. To validate the proposed model, actual panels from TATA manufacturers are used. The datasheet parameters are presented in Table 2.1. To verify the PV characteristics, HT I-V 400, IV tracer is used. The experimental setup is shown in Fig. 6.1. Since measurement of insolation and temperature for larger arrays are not possible, this setup is used only for validating smaller arrays presented in Chapter 2. However, for validating PV arrays of larger size, a PV simulator is used.

The results presented in rest of the thesis is validated using the hardware presented

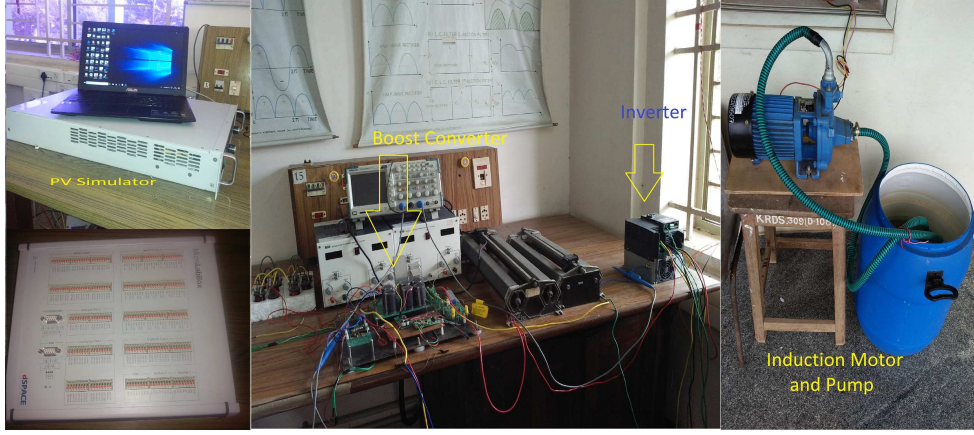


Figure 6.2: Prototype of the PV fed water pumping system

in 6.2. The details of the various components used in the hardware are given below

1. PV simulator : Magna Power XR 250-8
2. dSPACE control card : RT1202 Microlab box
3. Inverter: TOSHIBA VF S-15
4. Induction motor pump system: Kirloskar 1 HP, 230 V with Delta connected stator

Appendix B

$$\begin{aligned}
 A_{22} &= \frac{(r_l+r_{sw})^2 dT_s - (r_c + \frac{r_c R}{R+r_c})(2L+d^2 T_s(r_l+r_{sw}))}{L^2} - \frac{2v_{pv}(\frac{RV_{dc}}{R+r_c} - V_{pv} - V_d)}{dT_s(V_{pv} - I_{pv}(r_l+r_{sw}))^2} \\
 B_{21} &= \frac{2I_{pv}}{dT_s} \left(\frac{V_{dc}R}{R+r_c} - I_{pv}(r_{sw} + r_l) + v_d \right) - \frac{(r_{sw}+r_l)d^2 T_s + \frac{r_c R}{r_c+R}d^2 T_s}{2L^2} \\
 B_{23} &= \frac{(V_{pv} - I_{pv}(r_l+r_{sw}))dT_s(\frac{r_c R}{R+r_c} + r_c - (r_l+r_{sw}))}{L^2} + \frac{RV_{dc}}{(R+r_c)L} + \frac{V_d}{L} + \frac{2I_{pv}}{d^2 T_s(V_{pv} - I_{pv}(r_l+r_{sw}))} \left(\frac{RV_{dc}}{R+r_c} - V_{pv} + V_d \right) \\
 B_{23} &= \frac{(V_{pv} - I_{pv}(r_l+r_{sw}))dT_s(\frac{r_c R}{R+r_c} + r_c - (r_l+r_{sw}))}{L^2} + \frac{RV_{dc}}{(R+r_c)L} + \frac{V_d}{L} + \frac{2I_{pv}}{d^2 T_s(V_{pv} - I_{pv}(r_l+r_{sw}))} \left(\frac{RV_{dc}}{R+r_c} - V_{pv} + V_d \right)
 \end{aligned}$$

Rest all other co-efficients are zero

$$\begin{aligned}
a_{11} &= -\frac{1}{r_{cin} C_{in}} & c_{21} &= -\frac{1}{r_{cin}} \\
a_{22} &= -\frac{1}{L} \left(r_l + Dr_{sw} + \frac{Rr_c D'}{R+r_c} \right) & c_{22} &= 1 \\
a_{23} &= -\frac{D'R}{L(R+r_c)} & d_{13} &= -I_{pv} \frac{r_c R}{R+r_c} \\
a_{32} &= \frac{RD'}{C(R+r_c)} & d_{21} &= \frac{1}{r_{cin}} \\
a_{33} &= -\frac{1}{C(R+r_c)} & A_{11} &= -\frac{1}{r_{cin} C_{in}} \\
b_{11} &= \frac{1}{r_{cin}} & A_{33} &= -\frac{1}{C(R+r_c)} \\
b_{21} &= \frac{1}{L}; b_{22} = -\frac{D'}{L} & A_{32} &= \frac{R}{2LC(R+r_c)} (2L + D^2 T_s (r_l + r_{sw})) \\
E_{11} &= -\frac{D^2 T_s R r_c}{2(R+r_c)L} & B_{11} &= \frac{1}{r_{cin} C_{in}} \\
b_{23} &= \frac{I_{pv} \left(\frac{Rr_c}{R+r_c} - r_{sw} \right)}{L} + \frac{RV_c}{L(R+r_c)} + \frac{V_D}{L} & A_{23} &= \frac{R}{(R+r_c)} \left(\frac{D}{L} - \frac{2I_{pv}L}{DT_s(V_{pv} - I_{pv}(r_l + r_{sw}))} \right) \\
E_{21} &= \frac{1}{r_{cin}} & B_{31} &= -\frac{RD^2 T_s}{2LC(R+r_c)} \\
b_{33} &= -\frac{RI_{pv}}{(R+r_c)C} & B_{22} &= D - \frac{2LI_{pv}}{DT_s(V_{pv} - I_{pv}(r_l + r_{sw}))} \\
c_{12} &= \frac{r_c RD'}{R+r_c} & C_{13} &= \frac{R}{R+r_c} \\
C_{23} &= -\frac{1}{r_{cin}} & B_{33} &= -\frac{DT_s R (V_{pv} - I_{mpp}(r_l + r_{sw}))}{LC(R+r_c)} \\
c_{13} &= \frac{R}{R+r_c} & C_{22} &= 1 \\
& & C_{12} &= \frac{Rr_c}{2(R+r_c)L} (2L + D^2 T_s (r_l + r_{sw}))
\end{aligned}$$

Bibliography

- Altas, I. and Sharaf, A. (2008). A novel maximum power fuzzy logic controller for photovoltaic solar energy systems. *Renewable Energy*, 33(3):388–399.
- Appelbaum, J. (1986). Starting and steady-state characteristics of dc motors powered by solar cell generators. *IEEE Transactions on Energy Conversion*, (1):17–25.
- Appelbaum, J. and Sarma, M. (1989). The operation of permanent magnet dc motors powered by a common source of solar cells. *IEEE Transactions on Energy Conversion*, 4(4):635–642.
- Bartle, R. G. and Sherbert, D. R. (2000). *Introduction to Real Analysis*. New York: Wiley.
- Bharadwaj, P. and John, V. (2014). Direct duty ratio controlled mppt algorithm for boost converter in continuous and discontinuous modes of operation. In *2014 IEEE 6th India International Conference on Power Electronics (IICPE)*, pages 1–6.
- Bhat, S., Pittet, A., and Sonde, B. (1987). Performance optimization of induction motor-pump system using photovoltaic energy source. *IEEE Transactions on Industry Applications*, (6):995–1000.
- Blanes, J. M., Toledo, F. J., Montero, S., and Garrigos, A. (2013). In-site real-time photovoltaic i–v curves and maximum power point estimator. *IEEE Trans. Power Electron*, 28(3):1234–1240.
- Bonnett, A. H. (1996). Analysis of the impact of pulse-width modulated inverter voltage waveforms on ac induction motors. *IEEE Transactions on Industry Applications*, 32(2):386–392.

- Bose, B. K. (2010). *Power electronics and motor drives: advances and trends*. Elsevier.
- Brito, A. and Zilles, R. (2006). Systematized procedure for parameter characterization of a variable-speed drive used in photovoltaic pumping applications. *Progress in Photovoltaics: Research and Applications*, 14(3):249–260.
- Cai, H., Xiang, J., and Wei, W. (2016). Modelling, analysis and control design of a two-stage photovoltaic generation system. *IET Renewable Power Generation*, 10(8):1195–1203.
- Chen, X., Xu, D., Liu, F., and Zhang, J. (2007). A novel inverter-output passive filter for reducing both differential- and common-mode dv/dt at the motor terminals in pwm drive systems. *IEEE Transactions on Industrial Electronics*, 54(1):419–426.
- Corrêa, T. P., Seleme Jr, S. I., and Silva, S. R. (2012). Efficiency optimization in stand-alone photovoltaic pumping system. *Renewable Energy*, 41:220–226.
- Ding, K., Bian, X., Liu, H., and Peng, T. (2012). A matlab-simulink-based pv module model and its application under conditions of nonuniform irradiance. *IEEE Transactions on Energy Conversion*, 27(4):864–872.
- Erickson, R. W. and Maksimovic, D. (2007). *Fundamentals of Power Electronics*. Springer Science and Business Media.
- Eskander, M. N. and Zaki, A. M. (1997). A maximum efficiency-photovoltaic-induction motor pump system. *Renewable Energy*, 10(1):53–60.
- Espinoza-Trejo, D. R., Brcenas-Brcenas, E., Campos-Delgado, D. U., and Angelo, C. H. D. (2015). Voltage-oriented inputoutput linearization controller as maximum power point tracking technique for photovoltaic systems. *IEEE Transactions on Industrial Electronics*, 62(6):3499–3507.
- Fam, W. and Balachander, M. (1988). Dynamic performance of a dc shunt motor connected to a photovoltaic array. *IEEE Transactions on Energy Conversion*, 3(3):613–617.
- Farivar, G., Asaei, B., and Mehrnami, S. (2013). An analytical solution for tracking photovoltaic module mpp. *IEEE Journal of Photovoltaics*, 3(3):1053–1061.

- Femia, N., Lisi, G., Petrone, G., Spagnuolo, G., and Vitelli, M. (2008). Distributed maximum power point tracking of photovoltaic arrays: Novel approach and system analysis. *IEEE Transactions on Industrial Electronics*, 55(7):2610–2621.
- Garrigós, A., Blanes, J. M., Carrasco, J. A., and Ejea, J. B. (2007). Real time estimation of photovoltaic modules characteristics and its application to maximum power point operation. *Renewable Energy*, 32(6):1059–1076.
- Habetler, T. G., Naik, R., and Nondahl, T. A. (2002). Design and implementation of an inverter output lc filter used for dv/dt reduction. *IEEE Transactions on Power Electronics*, 17(3):327–331.
- Hartmann, L. V., Vitorino, M. A., de Rossiter Correa, M. B., and Lima, A. M. N. (2013). Combining model-based and heuristic techniques for fast tracking the maximum-power point of photovoltaic systems. *IEEE Transactions on Power Electronics*, 28(6):2875–2885.
- Herrmann, W. and Wiesner, W. (1996). Current-voltage translation procedure for pv generators in german 1000 roofs-programme. In *EUROSUN Conf., Freiburg, Germany*.
- Hu, J. and Sullivan, C. R. (1997). The quasi-distributed gap technique for planar inductors: design guidelines. In *IAS '97. Conference Record of the 1997 IEEE Industry Applications Conference Thirty-Second IAS Annual Meeting*, volume 2, pages 1147–1152 vol.2.
- Hu, J. and Sullivan, C. R. (2001). Ac resistance of planar power inductors and the quasideistributed gap technique. *IEEE Transactions on Power Electronics*, 16(4):558–567.
- Kerkman, R. J., Leggate, D., and Skibinski, G. L. (1997). Interaction of drive modulation and cable parameters on ac motor transients. *IEEE Transactions on Industry Applications*, 33(3):722–731.
- Kirchenberger, U., Marx, M., and Schroder, D. (1992). A contribution to the design optimization of resonant inductors for high power resonant dc-dc converters. In *Conference Record of the 1992 IEEE Industry Applications Society Annual Meeting*, pages 994–1001 vol.1.

- Kolhe, M., Joshi, J., and Kothari, D. (2004). Performance analysis of a directly coupled photovoltaic water-pumping system. *IEEE Transactions on Energy Conversion*, 19(3):613–618.
- Kutkut, N. H. and Divan, D. M. (1998a). Optimal air-gap design in high-frequency foil windings. *IEEE Transactions on Power Electronics*, 13(5):942–949.
- Kutkut, N. H. and Divan, D. M. (1998b). Optimal air-gap design in high-frequency foil windings. *IEEE Transactions on Power Electronics*, 13(5):942–949.
- Maranho, G. N. A., Brito, A. U., Pinho, J. T., Fonseca, J. K. S., Leal, A. M., and Macdo, W. N. (2016). Experimental results of a fuzzy controlled variable-speed drive for photovoltaic pumping systems: A review. *IEEE Sensors Journal*, 16(9):2854–2864.
- Masoum, M. A., Dehbonei, H., and Fuchs, E. F. (2002). Theoretical and experimental analyses of photovoltaic systems with voltage and current-based maximum power-point tracking. *IEEE Transactions on energy conversion*, 17(4):514–522.
- Matlin, R. W. (July 10, 1979). *Design Optimization and Performance Characteristics of a Photovoltaic Microirrigation System For Use In Developing Countries*. A Project sponsored by Government of United States, Lexington, Massachusetts.
- MNRE (2012). *Phase II – Policy Document*. Jawaharlal Nehru National Solar Mission.
- Mohan, N. and Undeland, T. M. (2007). *Power electronics: converters, applications, and design*. John Wiley & Sons.
- Muljadi, E. (1997a). Pv water pumping with a peak-power tracker using a simple six-step square-wave inverter. *IEEE Transactions on industry applications*, 33(3):714–721.
- Muljadi, E. (1997b). Pv water pumping with a peak-power tracker using a simple six-step square-wave inverter. *IEEE Transactions on industry applications*, 33(3):714–721.
- Ngo, K. D. T. and Kuo, M. H. (1988). Effects of air gaps on winding loss in high-frequency planar magnetics. In *PESC '88 Record., 19th Annual IEEE Power Electronics Specialists Conference*, pages 1112–1119 vol.2.

- Nomura, T., Wang, C., Seto, K., and Yoon, S. W. (2013). Planar inductor with quasi-distributed gap core and busbar based planar windings. In *2013 IEEE Energy Conversion Congress and Exposition*, pages 3706–3710.
- NREL (2017). Official website of nrel solar radiation research laboratory.
- Patel, H. and Agarwal, V. (2008). Matlab-based modeling to study the effects of partial shading on pv array characteristics. *IEEE TRANSACTIONS ON ENERGY CONVERSION*, 23(1).
- Periasamy, P., Jain, N., and Singh, I. (2015). A review on development of photovoltaic water pumping system. *Renewable and Sustainable Energy Reviews*, 43:918–925.
- Periasamy, P., N.K.Jain, and I.P.Singh (2014). A review on development of photovoltaic water pumping system. *Elsevier:Renewable and Sustainable Energy Reviews*, 7(43):918–925.
- Persson, E. (1992). Transient effects in application of pwm inverters to induction motors. *IEEE Transactions on Industry Applications*, 28(5):1095–1101.
- Pottebaum, J. R. (1984). Optimal characteristics of a variable-frequency centrifugal pump motor drive. *IEEE transactions on industry applications*, (1):23–31.
- Qin, L., Xie, S., Hu, M., and Yang, C. (2015). Stable operating area of photovoltaic cells feeding dc/dc converter in output voltage regulation mode. *IET Renewable Power Generation*, 9(8):970–981.
- Rodriguez, C. and Amaratunga, G. A. (2007). Analytic solution to the photovoltaic maximum power point problem. *IEEE Transactions on Circuits and Systems I: Regular Papers*, 54(9):2054–2060.
- Siebert, S., Burke, J., Faures, J.-M., Frenken, K., Hoogeveen, J., Döll, P., and Portmann, F. T. (2010). Groundwater use for irrigation—a global inventory. *Hydrology and Earth System Sciences*, 14(10):1863–1880.
- Singh, B., Singh, B., Singh, B., Chandra, A., and Al-Haddad, K. (1996). Optimized performance of solar powered variable speed induction motor drive. In *Power Electronics, Drives and Energy Systems for Industrial Growth, 1996., Proceedings of the 1996 International Conference on*, volume 1, pages 58–66. IEEE.

- Solodovnik, E. V., Liu, S., and Dougal, R. A. (2004). Power controller design for maximum power tracking in solar installations. *IEEE Transactions on Power Electronics*, 19(5):1295–1304.
- Steinke, J. K. (1999). Use of an lc filter to achieve a motor-friendly performance of the pwm voltage source inverter. *IEEE Transactions on Energy Conversion*, 14(3):649–654.
- Sun, J., Mitchell, D. M., Greuel, M. F., Krein, P. T., and Bass, R. M. (2001). Averaged modeling of pwm converters operating in discontinuous conduction mode. *IEEE Transactions on Power Electronics*, 16(4):482–492.
- Tafticht, T., Agbossou, K., Doumbia, M., and Cheriti, A. (2008). An improved maximum power point tracking method for photovoltaic systems. *Renewable energy*, 33(7):1508–1516.
- Toledo, F., Blanes, J. M., Garrigós, A., and Martínez, J. A. (2012). Analytical resolution of the electrical four-parameters model of a photovoltaic module using small perturbation around the operating point. *Renewable Energy*, 43:83–89.
- Villalva, M. G., Siqueira, T. G. D., and Ruppert, E. (2010). Voltage regulation of photovoltaic arrays: small-signal analysis and control design. *IET Power Electronics*, 3(6):869–880.
- Vitorino, M. A., de Rossiter Corrêa, M. B., Jacobina, C. B., and Lima, A. M. N. (2011). An effective induction motor control for photovoltaic pumping. *IEEE Transactions on Industrial Electronics*, 58(4):1162–1170.
- von Jouanne, A. and Enjeti, P. (1996). Design considerations for an inverter output filter to mitigate the effects of long motor leads in asd applications. In *Proceedings of Applied Power Electronics Conference. APEC '96*, volume 2, pages 579–585 vol.2.
- von Jouanne, A., Renusara, D., and P. Enjeti, W. G. (1995). Filtering techniques to minimize the effect of long motor leads on pwm inverter fed ac motor drives. In *Proc. IEEE IAS Conf.*, volume 2.

- Xiao, W., Lind, M. G., Dunford, W. G., and Capel, A. (2006). Real-time identification of optimal operating points in photovoltaic power systems. *IEEE Transactions on Industrial Electronics*, 53(4):1017–1026.
- Yadav, K., Sastry, O., Wandhare, R., Sheth, N., Kumar, M., Bora, B., Singh, R., Kumar, A., et al. (2015). Performance comparison of controllers for solar pv water pumping applications. *Solar Energy*, 119:195–202.
- Yao, Y., Bustamante, P., and Ramshaw, R. (1994). Improvement of induction motor drive systems supplied by photovoltaic arrays with frequency control. *IEEE Transactions on Energy conversion*, 9(2):256–262.
- Zhang, W. and Kimball, J. W. (2018). Dcdc converter based photovoltaic simulator with a double current mode controller. *IEEE Transactions on Power Electronics*, 33(7):5860–5868.

PUBLICATIONS BASED ON THE THESIS

Papers in refereed journals

1. **Arjun M**, Vanjari Venkata Ramana, Roopa Viswadev and B. Venkatesaperumal., “An Iterative Analytical Solution for Calculating Maximum Power Point in Photovoltaic Systems under Partial Shading Conditions.”, *IEEE Transactions on circuits and systems II – Express Briefs* (Accepted)
2. **Arjun M**, Vanjari Venkata Ramana, Roopa Viswadev, B. Venkatesaperumal and Sukumar Mishra., “Effect of Partial shading on Induction motor water pumping systems.”, *IEEE Transactions on Energy Conversion* (Under Review)
3. **Arjun M**, Vanjari Venkata Ramana, Roopa Viswadev and B. Venkatesaperumal., “Small Signal Model for PV fed Boost Converter in Continuous and Discontinuous Conduction Modes .”, *IEEE Transactions on circuits and systems II – Express Briefs* (Under review)

Papers published in referred conference proceedings

1. **Arjun M**, Subrahmanya Adiga, Anusha R and B V Perumal., “Experimental Investigation of the Effectiveness of the LC filter in PV fed Induction Motor Water Pumping Systems with different type of Inductors” In Proc. *International Conference on Emerging Trends in Engineering, Science and Technology (ICETEST)* , PICC.,DOI. 10.1109/PICC.2018.8384748/18/\$31.00 2018 IEEE.

Indian Patent

1. Venkatesaperumal, A Karthikeyan, **Arjun M** and Vanjari Venkata Ramana, *Solar water pumping system in grid tie or off grid mode with net zero energy from grid.*
Patent Number: **201641035575**. Status: **Published**

Bio-data

Name : Arjun M

Date of birth: 12-02-1991

Marital status: Unmarried

E-mail: arjunmudlapur@gmail.com

Mobile: +91-9902169213

Address

Research Scholar

Department of Electrical & Electronics Engineering

National Institute of Technology Karnataka

Surathkal, Mangaluru, India-575025, India.

Education

- **M.Tech.**, Power Electronics and control, Manipal Institute of Technology, MAHE, Manipal, Aggregate-9.71, 2015.
- **B.E.**, Electrical & Electronics Engineering, B. V. Bhoomaraddi college and Engineering and Technology, Hubli, Aggregate-9.03, 2012.
- **Inter**, Pre University Education, Shri Manjunatheshwara Pre University College, Aggregate-83%, 2008.
- **SSLC**, Little Flower English Medium High School, Hospet, Aggregate-90%, 2006.